Solid-state NMR studies of protein dynamics: New approaches and applications to crystalline proteins and large molecular assemblies

Paul Schanda

Habilitation à Diriger des Recherches (HDR)

Université Joseph Fourier, Grenoble

UFR de Chimie

Solid-state NMR studies of protein dynamics

New approaches and applications to crystalline proteins and large molecular assemblies

Dr. Paul Schanda

MEMBERS OF THE HABILITATION JURY:

Dr. Fabien Ferrage	(rapporteur)
Prof. Frans Mulder	(rapporteur)
Dr. Guido Pintacuda	(rapporteur)
Prof. Mikael Akke	(examinateur)
Dr. Dominique Bourgeois	(examinateur)
Prof. Tatyana Polenova	(examinatrice)
Prof. Bernd Reif	(examinateur)

Table of Contents

1 CHARACTERIZING PROTEIN MOTION AT ATOMIC RESOLUTION: INTRODUCING THE POSSIBILITIES OF SOLID-STATE NMR 6

1.1 INTRODUCTION – PROTEIN FUNCTION RELIES ON FLEXIBILITY 6
1.2 NEW POSSIBILITIES TO STUDY PROTEIN MOTION BY SOLID-STATE NMR 8
1.3 DIPOLAR COUPLINGS IN SOLID-STATE NMR: DIRECT INSIGHT INTO AMPLITUDES OF MOTION 10
1.4 NUCLEAR SPIN RELAXATION AND PROTEIN DYNAMICS 13
1.5 MOTION ON MICRO-TO-MILLISECOND TIME SCALES: PROBING DYNAMICS ON BIOLOGICAL FUNCTIONAL TIME SCALES 16
1.6 QUANTIFYING DYNAMICS IN THE SOLID STATE: EXPERIMENTAL CHALLENGES 16

2 DEUTERATION AND FAST MAGIC-ANGLE SPINNING: OVERCOMING CHALLENGES OF DYNAMICS STUDIES IN SSNMR 18

2.1 LONG COHERENCE LIFE TIMES IN DEUTERATED PROTEINS 18
2.2 NOVEL TYPES OF CORRELATION EXPERIMENTS: FROM ASSIGNMENT TO HYDROGEN-BOND SCALAR COUPLINGS 20
2.3 STRUCTURE DETERMINATION OF DEUTERATED PROTEINS FROM UNAMBIGUOUS ^{1}H-^{1}H DISTANCE RESTRAINTS 21

3 SOLID-STATE NMR MEASUREMENTS OF ASYMMETRIC DIPOLAR COUPLINGS PROVIDE INSIGHT INTO PROTEIN SIDE-CHAIN MOTION 24

3.1 INTRODUCTION 24
3.2 EXPERIMENTAL OBSERVATION OF ASYMMETRIC DIPOLAR COUPLINGS IN UBIQUITIN SIDE CHAINS 25
3.3 MODELS OF SIDE CHAIN MOTION FROM DIPOLAR COUPLINGS 29
3.3.1 Valines 29
3.3.2 Leucines 30
3.3.3 Isoleucines 31
3.3.4 Possibilities of studying other side chains, and characterizing side chain motion in even more detail 32

4 TIME SCALES AND AMPLITUDES OF PROTEIN BACKBONE DYNAMICS IN THE SOLID-STATE 33

4.1 PROTON-DETECTED SPECTROSCOPY ON UBIQUITIN: ASSIGNMENTS AND QUALITATIVE CONCLUSIONS ABOUT DYNAMICS 34
4.2 INSIGHT INTO SUB-MICROSECOND BACKBONE MOTION FROM EXPERIMENTAL DATA: THEORETICAL CONSIDERATIONS 35
4.3 AMPLITUDES OF BACKBONE MOTION FROM NH DIPOLAR COUPLINGS 38
4.4 TIME SCALES OF BACKBONE MOTION: INSIGHT FROM DIFFERENT SPIN RELAXATION PARAMETERS. 41
- ^{15}N R_1 AT FIELD STRENGTHS CORRESPONDING TO 500, 600 AND 850 MHZ ^{1}H LARMOR FREQUENCY .. 41

4.5 COMPARISON TO SOLUTION-STATE NMR: DOES THE CRYSTAL LATTICE IMPACT PROTEIN DYNAMICS? 45
4.6 THE IMPACT OF THE CRYSTALLINE ENVIRONMENT FROM COMPARISONS OF DIFFERENT CRYSTAL POLYMORPHS 47
4.7 CONCLUSIONS 47

5 SITE-RESOLVED MEASUREMENT OF MICROSECOND TO MILLISECOND CONFORMATIONAL-EXCHANGE PROCESSES IN PROTEINS BY SOLID-STATE NMR SPECTROSCOPY 50

5.1 INTRODUCTION 50
5.2 RESULTS AND DISCUSSION 51
5.2.1 Differential zero- and double-quantum ^{1}H-^{15}N line broadening reveals conformational exchange. 51
5.2.2 ^{15}N CPMG relaxation dispersion experiments. 55
5.2.3 Comparison to conformational exchange in solution. 57
5.3 CONCLUSIONS 60

6 STRUCTURAL INSIGHT INTO TRANSIENT CONFORMATIONAL STATES OF PROTEINS BY SOLID-STATE $R_{1\rho}$ RELAXATION-DISPERSION NMR SPECTROSCOPY 61
6.1 INTRODUCTION 61
6.2 THE PROPERTIES OF $R_{1\rho}$ EXPERIMENTS IN MAS SOLID-STATE NMR: INSIGHT FROM NUMERICAL SIMULATIONS 61
6.3 EXPERIMENTAL IMPLEMENTATION OF $R_{1\rho}$ RELAXATION DISPERSION 63
6.4 KINETICS AND THERMODYNAMICS OF CONFORMATIONAL EXCHANGE: FITTING THE BLOCH-MCCONNELL-REGIME OF $R_{1\rho}$ DISPERSION CURVES 64
6.5 BEYOND CHEMICAL SHIFT INFORMATION: BOND ORIENTATION CHANGES UPON THE STRUCTURAL TRANSITION TO THE EXCITED STATE 67

7 ATOMIC MODEL OF A CELL-WALL CROSS-LINKING ENZYME IN COMPLEX WITH AN INTACT BACTERIAL PEPTIDOGLYCAN 69
7.1 INTRODUCTION 69
7.2 EXPERIMENTAL SECTION 70
7.2.1 Sample preparation 70
7.2.2 NMR spectroscopy and structure calculation 70
7.3 RESULTS 71
7.3.1 Ldt_{Bs} tightly binds to peptidoglycan 71
7.3.2 Peptidoglycan dynamics in the protein-bound state 73
7.3.3 Atomic model of the complex from ^{1}H-detected ssNMR experiments 74
7.3.4 Mutants and isolated domains have different binding affinities than full-length wild-type Ldt_{Bs} 76
7.4 DISCUSSION 79
7.5 CONCLUSIONS 80

8 SUBSTRATE TRANSLOCATION ACROSS THE INNER MITOCHONDRIAL MEMBRANE . 82

Preface

This habilitation manuscript outlines some of the work I performed since the beginning of my research on solid-state NMR in Beat H. Meier's laboratory in 2008, and at IBS Grenoble since 2011. The particular emphasis of this work is on the use of solid-state NMR spectroscopy for the study of protein dynamics. This field has seen great improvements and developments over the last 10-15 years, to which I hope was able to contribute somewhat.

The field of protein dynamics has fascinated me since my undergraduate studies. This fascination arose from interactions I had with several persons that have shared their passion for protein dynamics and structural biology NMR with me. I therefore would like to express here my gratitude to these persons, and many others that have been influential for my work, but which would be too numerous to be exhaustively listed here.

My early fascination for NMR has been triggered by Robert Konrat and Bernhard Brutscher, and although none of the work described here was done with them, I am grateful for their guidance. I am particularly grateful to the people that have taught me solid-state NMR spectroscopy at ETH Zurich, most notably Matthias Ernst, Beat H. Meier and René Verel.
Matthias' scientific rigor and ability to explain NMR theory, down to the last detail, and his ability to "walk through Floquet space" better than some of us wander around in 3D space, leaves me impressed. I am grateful for his support during my time at ETH. I would also like to acknowledge Beat's support, who let me develop all the proton-detection approaches on my own in his lab. I am particularly grateful also for the excellent NMR courses that Beat and Matthias were giving at ETH.
Some of the proton-detected experiments were done together with Matthias Huber, and I thank him for numerous discussions.

I would like to thank particularly my colleagues at IBS Grenoble. Special thanks goes to Bernhard Bruscher, Jerome Boisbouvier and Jean-Pierre Simorre for their support when setting up my research activity at IBS. I have and had the great chance to work with excellent colleagues, post-docs, PhD students and exchange students. Jens Haller, although he has been in my group for just a few months, made impressive progress and was the main actor in some of the ubiquitin dynamics work presented in this work. Astrid Sivertsen, Peixiang Ma and Vilius Kurauskas were brave enough to embark on a difficult membrane project, and I am grateful for their endurance and efforts. Peixiang has been a very valuable member of the team also for projects which are rather far from his initial education: he managed to make sense out of our work on relaxation dispersion, and I want to express my gratitude for his wide range of activities. I would also like to thank Audrey Hessel, who has set up the activity that I myself know least – membrane protein biochemistry – and has been a major driving force, together with Vilius and Peixiang, to bring forward the membrane protein project. Special thanks goes to Martin Tollinger, with whom I had the chance to collaborate at several instances, which has always been a very stimulating experience.

My work on proton-detected solid-state NMR spectroscopy started out when I entered the solid-state NMR field in 2008. At that time Beat gave me the freedom to choose my research topic by myself, and among the most promising approaches I found in the literature for measuring dynamics were reports on deuteration and proton detection. The ideas that were around at that time, particularly put forward by Bernd Reif, but also others, shaped the way I approached solid-state NMR. Thanks to the impressive methodological developments, NMR studies of protein dynamics have made great progress over the last decade, and I am happy to witness these exciting steps of the field.
I am glad that some of the researchers that actively shape NMR these days, and that have been inspiring for my work have accepted to take the time to read and evaluate the present HDR manuscript and HDR defense.

Dr. Paul Schanda
September 2014

1 Characterizing protein motion at atomic resolution: introducing the possibilities of solid-state NMR

1.1 Introduction – Protein function relies on flexibility

One of the key goals of contemporary science is the understanding of cellular processes on a molecular level. The determination of the three-dimensional structure of biomolecules has been extremely important to understand the molecular basis of processes in living cells. The hallmark feature of all processes in living systems, however, is molecular motion. Thus, the static pictures provided by traditional structural biology approaches fail to grasp an important aspect of biomolecules, namely how these structures interconvert between alternate conformations, thereby possibly sampling states that are the actual functionally relevant ones.

Characterizing protein motion at atomic resolution is challenging. Dynamics occur on a wide range of time scales, calling for versatile methods sensitive to different time scales and types of motions. Furthermore, functionally relevant structural excursions may be infrequent, and involve short-lived conformational states that are populated to only minute extents in equilibrium with a major conformation. Detecting minor forms in the presence of an overwhelming conformer represents a severe challenge in terms of sensitivity. In addition, one wants to study protein motion in the environment where the molecule actually performs its function, i.e. possibly in the cellular context, or at least in near-native solution or in the native membrane environment. Given all these different requirements, advanced experimental methods, or combinations of methods are often required to characterize protein dynamics. A number of experimental techniques have been developed to study protein dynamics. While exhaustively reviewing these techniques is not within the scope of this work, one may cite in particular methods based on detailed analysis of X-ray diffraction data, possibly collected at physiologically relevant temperature[1-3], that visualize alternate conformations (although without providing insight into thermodynamics/kinetics or the processes). Kinetic crystallography represents a very attractive route to studying off-equilibrium dynamics in systems in which a reaction can be triggered,[4] which in many cases is difficult to achieve. Lower-resolution methods, such as IR spectroscopy,[5] also provide powerful tools to monitor global structural changes, although without atomic details.

Arguably, NMR spectroscopy in solution state stands out among many experimental techniques for studying protein dynamics. NMR spectroscopy delivers information about motions on a wide range of time scales at atomic resolution. Not only does it provide information at the atomic scale about the presence of motion, but it also gives detailed information about time scales and relative populations of states, and thus gives access to a range of physico-chemical parameters.
Solution-state NMR methods nowadays routinely probe the bond librational motions of the protein backbone and side chains, that can be used as a direct measure of conformational entropy, thus providing insight into the thermodynamics of proteins.[6]
Excitingly also, NMR spectroscopy can probe motions that are on time scales at which proteins actually perform their function, which are mostly millisecond time scales. A growing list of beautiful examples highlights this power of NMR spectroscopy to directly see proteins in action. NMR techniques have, for example, allowed to get insight into enzyme function, where it could be directly shown that the rate at which an enzyme performs its action corresponds to the rate at which it undergoes conformational exchange, and that this exchange process is present even without substrate.[7]

Motion also plays an important role in membrane proteins, where substrate transport can often be accomplished only if the membrane protein undergoes significant structural rearrangement. In this

context, a recent work has beautifully explained how the small multidrug resistance transporter EmrE dynamically exchanges between two states that are open to one side of the membrane, thus allowing to transport its substrates.[8]

Dynamic exchange processes also play a key role in allosteric regulation. Figure 1 shows an example of a dynamic process in an allosteric protein, the small transcription co-activator domain KIX, which can bind two transcription factors. In vitro, binding of the MLL activation domain to KIX cooperatively enhances the interaction with c-Myb: KIX in complex with MLL displays a ~2-fold higher affinity for the c-Myb activation domain than the KIX domain alone. While this allostery has been detected by thermodynamic methods, the molecular mechanism that mediates this cooperativity remained unclear. NMR methods could shed light onto this phenomenon: in the presence of only one of the two binding partners, the binary complex (KIX+MLL) is in continuous exchange between a major conformational state (of which a structure had been determined), and a minor state, that is too transient and low-populated to be seen in a crystal structure or conventional NMR structure. Our solution-state NMR data could reveal that it is this minor state that is pre-formed to bind the second transcription factor.[9] In other words, the actual function state of this protein does not correspond to the main conformer, that is generally in the focus of structural biology. Rather, a dynamically sampled alternate conformation is the functionally relevant one.

These few examples (and many many more could be cited here) emphasize the importance of characterizing "hidden" states, which generally are overlooked by the static views of structural biology. Understanding the jiggling and wiggling of biomolecules in detail will provide important clues about their functions.

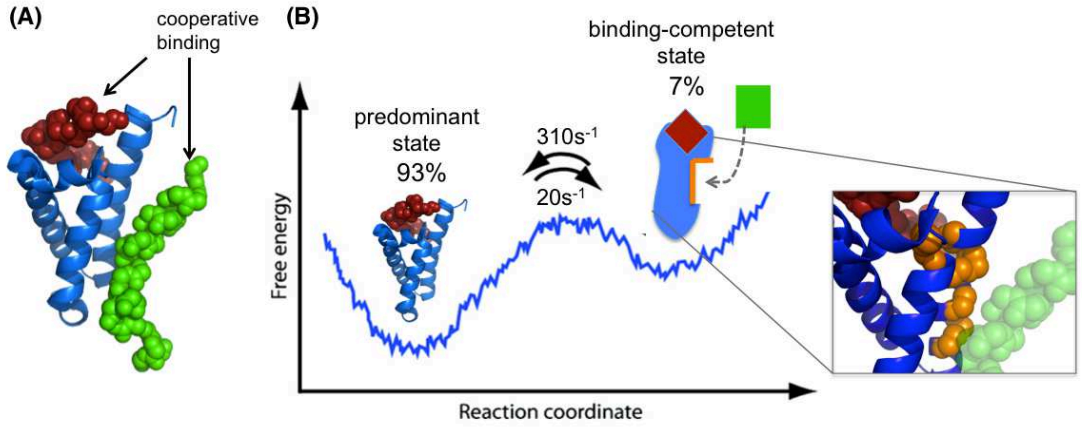

Figure 1. A dynamic process underlies allosteric signal transmission in the KIX domain. (A) Structure of the transcription co-activator KIX (blue) in complex with two transcription factors, MLL and c-Myb (red, green). (B) In the presence of only one of the two binding partners (MLL, red), KIX is in a dynamic exchange between a major state and a transient minor state on a millisecond time scale. The minor state is preformed to accommodate the second binding partner, explaining the allostery of binding.

1.2 New possibilities to study protein motion by solid-state NMR

Biological processes occur in complex cellular environments. Many processes involve very large biomolecular complexes and assemblies, such as ribosomes, membrane-embedded proteins and enzymatic complexes of hundreds of kilodalton in size. Solution-state NMR spectroscopy is significantly challenged in these cases: many of these objects may inherently not be soluble (e.g. membrane proteins), or their large size and associated slow molecular tumbling in solution leads to rapid signal loss and line broadening.
Magic-angle spinning solid-state NMR (MAS ssNMR) does not face these inherent limitations. The perspectives of gaining atomic-resolution insight into objects that were so far out of reach (for solution-state NMR) have been a major driving force for the development of the technique. While the technically more demanding requirements of MAS ssNMR have retarded the widespread use of ssNMR in structural biology for some time, relative to its solution-state counterpart, the development of ssNMR over the last decade is impressive. Protein structures of increasing size and complexity are nowadays being determined by ssNMR,[10] and, importantly also, interactions can be probed in complex environments, including entire cells and cell walls.[11]

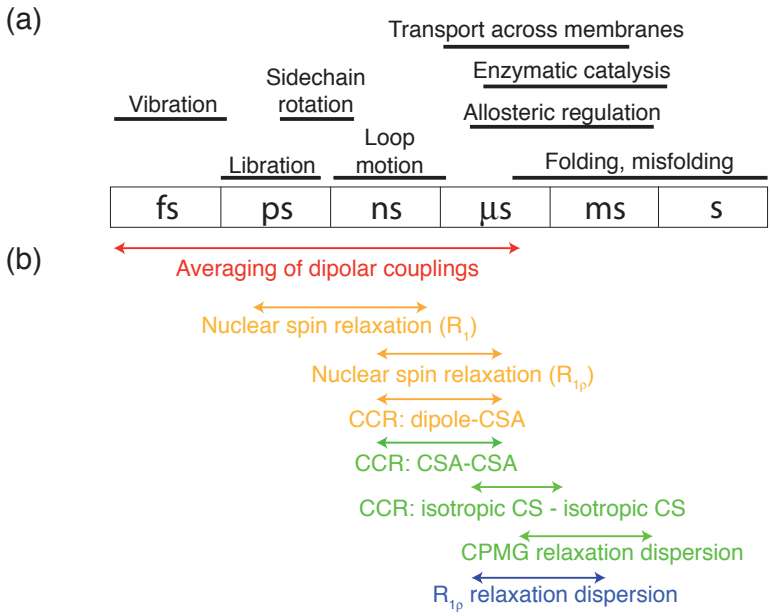

Figure 2. Time scales of protein dynamics (a) and corresponding solid-state NMR approaches to probe these motions (b). The approaches shown in (b) will be discussed in the present manuscript. The averaging of dipolar couplings (red) is introduced in section 1.3 and in more detail in chapter 3. Relaxation approaches (shown in orange) are discussed in section 1.4 and their application to studying protein backbone is discussed in chapter 4. Slower motional processes can be studied using methods shown here in green and blue, discussed in chapters 5 and 6, respectively.

The development of MAS ssNMR has also opened the way to probe protein dynamics in these samples. In addition to probing motion in systems that are out of reach for solution-state NMR, solid-state NMR also allows addressing interesting biophysical questions. For example, solid-state NMR can monitor motion in (micro-)crystalline proteins, thus allowing to answer to questions that arise in crystallography, such as the link to crystallographic temperature factors.

Figure 2 shows time scales of protein dynamics, and MAS ssNMR approaches to study these motions, whereby, for simplicity, only the methods that were used and developed in this present

habilitation are shown. (The reader is referred to reviews on protein dynamics for a more comprehensive treatment of the subject.[12-15])

In the remainder of this chapter, different techniques for measuring dynamics in solids are introduced. The main aim of this introduction is to allow the reader getting an intuitive understanding of the approaches. The discussion deliberately avoids deriving the theory behind the methods in a formal way. A rigorous formal introduction of the theory (e.g. Redfield theory or dipolar coupling Hamiltonians) would by far exceed the scope of the present discussion, and I apologize for having to refer the reader to more thorough treatments of these theories. I shall also apologize for the fact that I cannot (by far!) discuss all of the approaches that have been proposed for studying dynamics, but rather focus on those that seem most relevant for my work.

1.3 Dipolar couplings in solid-state NMR: direct insight into amplitudes of motion

The dipolar coupling is the dominant spin-spin interaction in the solid state. It is used as the primary source of structural information, and it is also a very useful tool for studies of dynamics.
In the absence of an external magnetic field, the dipolar interaction between two spins is isotropic: it depends exclusively on the distance between the two spins as well as the types of spins involved, but not on their relative orientation in space (Figure 3A). This situation is never encountered in NMR spectroscopy, where a strong external magnetic field dictates a preferential orientation. This external magnetic field truncates the dipolar-coupling interaction, which becomes anisotropic (i.e. orientation-dependent, Figure 3B). In the case of the heteronuclear dipolar coupling between two spins, *k* and *n*, the Hamiltonian describing the interaction can be written as:

$$\hat{\mathcal{H}}_{\mathrm{D}}^{(k,n)} = -\frac{\mu_0}{4\pi}\frac{\gamma_k\gamma_n\hbar}{r_{kn}^3}\frac{(3\cos^2\theta-1)}{2}2\hat{I}_{kz}\hat{S}_{nz}$$

where θ denotes the orientation of the inter-nuclear vector relative to the laboratory frame (given by the orientation of B_0), r_{kn} is the inter-nuclear distance, and γ_i is the gyromagnetic ratio of spin *i*. Due to the functional form of the dependence of the dipolar coupling on the orientation, $(3\cos^2\theta\text{-}1)/2$, the splitting due to a heteronuclear dipolar coupling takes values ranging from $+1\cdot\delta_D$ to $-0.5\cdot\delta_D$, where δ_D is the anisotropy of the dipolar coupling tensor given as $\delta_D = \frac{-2\mu_0}{4\pi}\frac{\gamma_k\gamma_n}{r_{nk}^3}$.

The dipolar coupling tensor depicted in Figure 3B reflects this situation. Here, the orientation of the tensor reflects the orientation of the inter-nuclear vector, i.e. in the example in Figure 3B the internuclear vector is parallel to the B_0 axis. The dipolar splitting can be found from the component of the tensor along the B_0 axis.

Of particular relevance for this manuscript is the impact of dynamics on the dipolar coupling. Dynamics, i.e. the interconversion of numerous structures, reorients a given inter-nuclear vector in a molecule, and thus modulates the orientation of the dipolar coupling between the involved nuclei. As a consequence, the dipolar coupling tensor is given by the time-averaged tensor over all involved orientations. For a given inter-nuclear vector in a single molecule, oriented at a certain angle with respect to the external magnetic field strength, this averaging of orientations can, in principle, increase or decrease the effective dipolar coupling (i.e. the anisotropy of the dipolar-coupling tensor). Dynamics will result in an increased dipolar coupling strength for an internuclear vector aligned at the magic angle (where the dipolar coupling strength vanishes), but dynamics will decrease the coupling strength for most orientations. When considering an ensemble of randomly oriented molecules within the sample (a “powder”), the dynamic process leads to an overall reduction of the dipolar coupling strength. This averaging in schematically shown in Figure 3D.

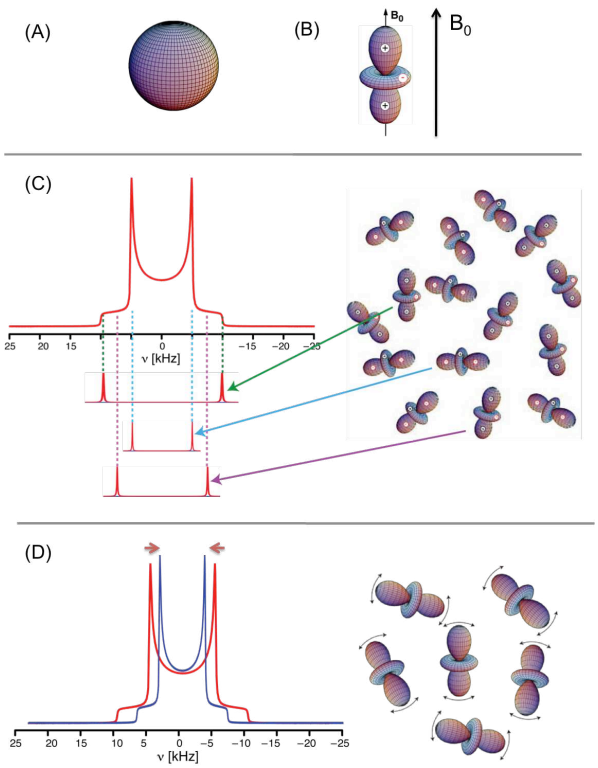

Figure 3. The dipolar coupling in solid-state NMR. (A) In the absence of an external magnetic field, the dipolar coupling between two spins is isotropic, i.e. independent of the relative orientation of the two interacting spins. (B) The presence of an external magnetic field B_0 renders the dipolar coupling anisotropic, and its orientation-dependence is described by a rank 2 tensor, that is depicted. The interaction strength can be seen as the component of this tensor along the B_0 field axis. (C) In a sample of randomly oriented molecules, a given internuclear vector in different molecules samples all possible orientations, leading to a distribution of coupling strengths that results in a powder-pattern (left). (D) In the presence of motion, the coupling strength is reduced. Note that (C) and (D) depict the situation of static samples (without MAS).

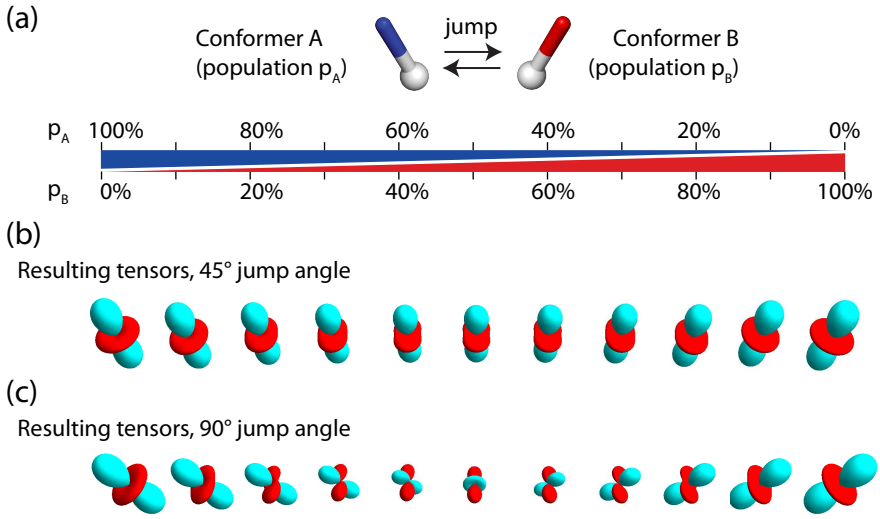

Figure 4. The effect of motion on the dipolar coupling tensor, shown for a two-site exchange process. In panels (b) and (c) the resulting dipolar coupling tensors are shown for the exchange depicted in panel (a). The different tensors in (b) and (c) correspond to the averaged tensors resulting from the two-site exchange with relative populations of the two states ranging from 100% state A to 100% state B. Positive and negative lobes of the dipolar coupling tensors are shown in red and cyan.

The measurement of dipolar couplings in solid therefore gives a very direct access to the amplitude of the motion sampled by a given inter-nuclear vector: a comparison of the experimentally measured dipolar-coupling tensor with the rigid-limit dipolar-coupling tensor reveals the space sampled by the vector under consideration. Generally this amplitude of motion is described by a single value, the "order parameter", S, that compares the anisotropies δ_D of the dipolar coupling tensors, $S = \delta_{D,measured}/\delta_{Drigid}$. The rigid-limit tensor δ_{Drigid} depends only on the types of nuclei and

the inter-nuclear distance. For directly bonded nuclei, where the distance is given by the bond length, the rigid-limit is thus readily computed.
This order-parameter description of a dynamic process is of course an oversimplification, because motion is in the general case asymmetric, i.e. its amplitude is orientation-dependent. Figure 4 illustrates the effect of a simple two-site exchange model on the dipolar-coupling tensor. As can be seen by comparing the dipolar-coupling tensors depicted in Figure 4b and c with the rigid-limit coupling tensor (Figure 3B), the motional process not only changes the strength of the dipolar coupling (i.e. the anisotropy of the tensor), but it also makes this tensor asymmetric. This often-overlooked fact can be put to good use: the characterization of the anisotropy AND asymmetry of the dipolar-coupling tensor allows extracting information of the motional process at a fair level of detail. Chapter 3 shows the measurement of the asymmetry of dipolar couplings, and illustrates how such measurements provide access to side chain motional processes, such as rotamer jumps.

The above discussion illustrated how motion averages dipolar couplings. So far we have assumed that all the orientations that a given inter-nuclear vector samples contribute to this averaging. However, it is of course important to consider the time scale over which this averaging is effective. In Figure 5 we consider the averaging process through explicit numerical spin simulations, i.e. simulations of a REDOR-experiment under MAS, assuming a three-site exchange process. REDOR is a recoupling experiment which re-introduces the dipolar coupling under MAS, and the coupling strength is reflected by the oscillation frequency of the curve, where fast oscillation reflects a large dipolar-coupling strength δ_D.
As Figure 5 reveals, a fast motional process leads to an averaging, and thus a reduced dipolar coupling strength, see lower right panel. This is the averaging process discussed above. The other extreme, very slow motion effectively means that the involved conformational states never inter-convert. Thus, each of the involved states has its full rigid-limit dipolar coupling (top left panel).
The transition between these two extremes occurs when the rate matches the (rigid-limit) dipolar-coupling strength, as Figure 5 shows.
This situation resembles the coalescence observed in chemical-shift averaging between two (or more) states with different chemical shifts: exchange with a rate slower than the chemical-shift difference between the states results in two separate peaks, while fast exchange ($k_{ex}>>\Delta\omega$) results in a single peak. In between these two extremes, broadening of the peak occurs, similar to the situation in the coalescence regime in Figure 5.

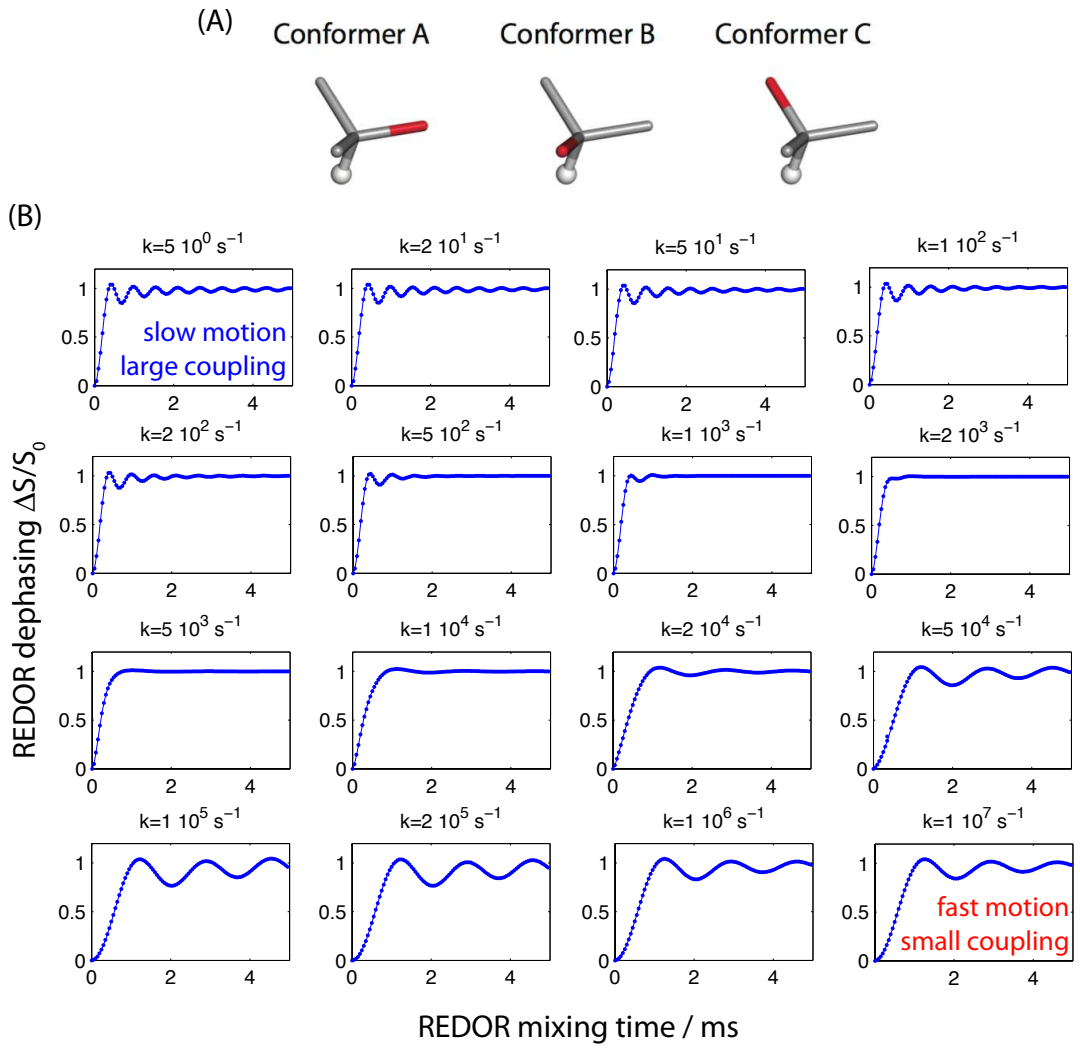

Figure 5. Motional averaging of heteronuclear dipolar coupling, as seen by explicit numerical simulations of a system undergoing three-site exchange. In this model, depicted in (A), a given internuclear vector, as shown in red, jumps between three distinct conformations, which are here assumed to have tetrahedral symmetry. It is assumed that the relative populations of the three states are equally distributed (an assumption that is lifted in chapter 3). In (B), the resulting REDOR recoupling curves are shown for different rates of exchange between the states, from very slow motion (top left) to very fast motion (bottom right), as indicated above the panels. The coupling strength assumed here is 20 kHz (approximately a 1.02Å N-H distance). The REDOR recoupling is performed as in reference[16].

Taken together, dipolar couplings provides a rich source of information about motional amplitudes. They possibly can reveal details of the motion, such as asymmetric motion, as long as the motional process takes place on time scales shorter than the inverse of the coupling strength. For typical heteronuclear systems (H-C, H-N, where δ_D is approximately 10 to 25 kHz) this means that amplitudes of motions faster than about 10-20 µs can be accessed. The development of methods to accurately measure dipolar couplings, and applications thereof, are shown in chapters 3, 4 and 7.

1.4 Nuclear spin relaxation and protein dynamics

Nuclear spin relaxation rates are sensitive to molecular motion. In solution state, where anisotropic interactions (dipolar couplings and chemical-shift anisotropies) are averaged by molecular tumbling, nuclear spin relaxation rates are the primary source of information about molecular motion. Nuclear spin relaxation is sensitive to the amplitude and time scales at which anisotropic

interactions (dipolar couplings, CSAs) are modulated. Through the well-established Redfield theory[17]
A detailed treatment of the theory of spin relaxation is not within the scope of this manuscript, and the reader is referred to excellent text books that cover in particular the situation in solution state (see, for example reference [18])

Likewise, relaxation rates also provide valuable information about motion in solids.
In this discuss we will not treat relaxation theory, but rather briefly introduce the main differences of solid-state relaxation approaches as compared to the (more widespread) solution-state relaxation analyses.

The main difference to solution-state NMR is the fact that in solid proteins do not have overall tumbling. This fact results in a number of important consequences:

1. Solution-state NMR measurements of internal molecular motion are restricted to time scales shorter than the overall molecular tumbling correlation time scale. This comes from the fact that overall tumbling averages all correlation functions of motion, and therefore any internal motion that is slower than the overall tumbling (typically in the low nanosecond range) becomes masked by the overall motion. In solids this is not the case, due to the absence of tumbling. Thus, solid-state NMR can probe motions over much wider ranges of time scales. Figure 6 shows this situation for 15N relaxation rates. The left panels show the situation in solution state: any internal motion that is slower than the overall motion does not lead to any alteration of the relaxation rates.

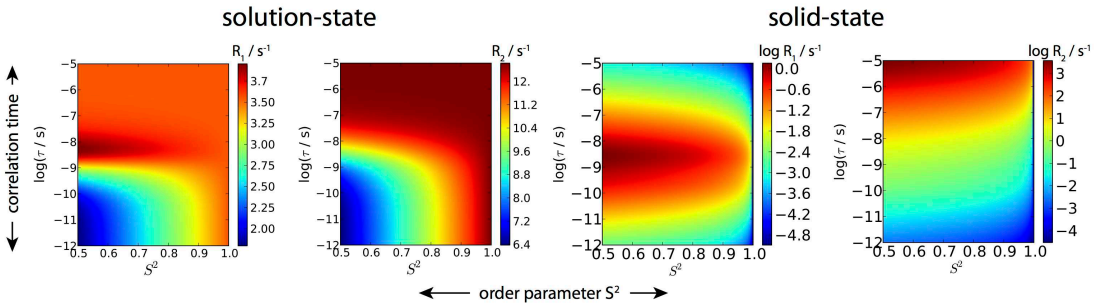

Figure 6. Relaxation rates in solution and solid state, arising from internal motion, as a function of the parameters of the internal motion. Shown are ^{15}N R_1 and R_2 relaxation rates in solution-state, assuming an overall tumbling correlation time of 5 ns, and in the solid state (right), in the absence of overall motion. The relaxation rates are calculated as a function of the squared order parameter (x-axis), describing the motional amplitude, and the correlation time of internal motion.

2. The overall motion in solution state is generally the dominant process leading to relaxation. As a consequence, in solution state the relaxation rates e.g. of ^{15}N spins are dictated by this overall motion, which is the same for the entire molecule. Figure 7 depicts this situation with the example of 15N R1 relaxation rates in ubiquitin. As these data show, the relaxation rates are very uniform, and site-to-site variations are only of the order of 10 %. This is completely different in solids, where relaxation is uniquely due to internal motion. The right panel in Figure 7 shows ^{15}N R_1 rates in the same protein, ubiquitin, in crystals. Site-to-site variations of relaxation rates are much larger, about one order of magnitude. Thus, solid-state NMR has the potential to reveal the internal motion with much higher precision that solution-state NMR.

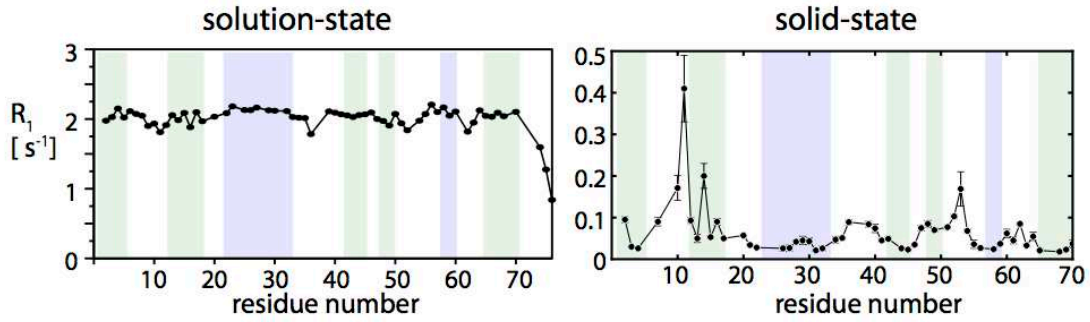

Figure 7. ^{15}N R_1 relaxation rates in ubiquitin in solution and in crystals. Note that the site-to-site variation of relaxation rates in solution is less than 10%, whereas relaxation rates vary by more than one order of magnitude in solids.

3. The absence of tumbling also leads to serious experimental and theoretical complications. On the theoretical side, the validity of the generally used theory of spin relaxation, Redfield theory[17], is not generally granted. In the derivation of Redfield theory, it is assumed that the relaxation rates are much smaller than the rate of the dynamic processes that leads to the relaxation. In solution state, there is always molecular tumbling on ps-ns time scales, and relaxation rates are always in the ms-s time scale. Thus, in solution state the validity of Redfield's derivation is always given. In solids this is not necessarily the case. Figure 6 (right panel) shows the R_2 relaxation rates in solids, derived with Redfield theory. In the top of this panel i.e. at long correlation times of microseconds, the R_2 rates become very large, and comparable to the correlation time. In this regime Redfield theory starts losing its validity. Numerical simulation of spin relaxation may be one way of deriving theoretical relaxation rates in this regime.
4. On the experimental side, the absence of tumbling has also severe consequences, that arise because anisotropic interactions – most notably dipolar couplings – are not averaged out any more, unlike in solution. The dipolar couplings can thus lead to evolution of the density operators. This coherent evolution gives rise to spin-diffusion of longitudinal spin density operators, and can thus interfere with the accurate measurement of "real", i.e. incoherent longitudinal relaxation processes that are due to stochastic motion. This situation is thus a challenge for measuring R_1 rate constants. The situation is even more severe for transverse relaxation. In solids the fate of nuclear spin coherences is generally largely dominated by dipolar dephasing. For this reason, transverse relaxation parameters in solids are very difficult to access. Solutions to this problem have been proposed for 15N spins,{Chevelkov:2007dc}{Lewandowski:2011gw} but so far accessing transverse relaxation rates of carbons or protons remains a challenge.

Taken together, solid-state relaxation measurements provide potentially a very rich source of information about sub-microsecond motion in (bio-)molecules. There are challenges, however, with respect to how one can access relaxation rates properly, and how to interpret them.
The main challenge on the experimental side is due to the strong dipolar couplings to protons. The advent of deuteration for analyzing dynamics in solids, pioneered by Reif and co-workers, and also described in this manuscript, as well as fast magic-angle spinning, explored by a number of groups, has thus lead to an improvement, and has allowed to measure relaxation rates in a quantitative manner.

1.5 Motion on micro-to-millisecond time scales: Probing dynamics on biological functional time scales

Many biomolecular reactions take place on microsecond to millisecond time scales. Over the last 15 years solution-state NMR has witnessed a very strong interest in measuring dynamics on these time scales, and impressive examples have related such dynamics to biomolecular function and protein folding.[9,21-23]

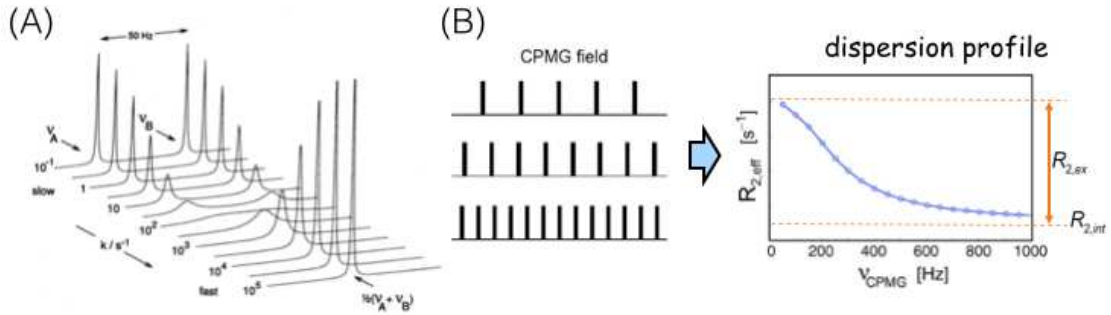

Figure 8. The impact of microsecond to millisecond exchange on NMR spectra in solution, and the well-established solution-state CPMG methodology to access such motions. Panel (A) shows spectra of a system that exchanges between two states with different chemical chemical shifts (separated by Δω=50 Hz), as a function of the time scale of the exchange process. In this case the two states are equally populated. Panel (B) schematically depicts the principle of CPMG experiments. Transverse relaxation is measured in the presence of a train of refocusing pulses. The spacing of these pulses is changed (resulting in different pulsing frequencies ν_{CPMG}), and in the presence of an exchange process the effective transverse relaxation rate is altered. The right panel shows the effective relaxation rates as a function of the ν_{CPMG}.

Figure 8 shows the effect that an exchange process between two states with different chemical shift has on an NMR spectrum. Exchange between different conformations leads to line broadening, and in many cases it becomes impossible to detect minor conformational states in exchange with a major state, because the effect of the exchange broadens the resonances beyond detection. Nonetheless, the presence of minor conformational states is detectable through the line broadening of the major-state peak that remains observable. Carr-Purcell-Meiboom-Gill (CPMG) relaxation dispersion experiments (Figure 8B) or $R_{1\rho}$ relaxation-dispersion experiments essentially quantify this line broadening, and thereby provide access to conformational exchange processes. Quantitative analysis of relaxation-dispersion data (right panel in Figure 8B) allow the quantification of the kinetics of the exchange process, the relative populations and the chemical-shift difference. These approaches are well established in solution-state NMR.
While a theoretical treatment is not within the scope of this manuscript, it is worth highlighting the particularities of solid-state NMR approaches that aim at quantifying exchange processes.
The primary challenge for quantifying conformational exchange in solids comes from the fact that line widths in the solid state are generally dominated by factors that are unrelated to dynamics. In particular, as mentioned in the previous section, dipolar dephasing represents the primary factor of line broadening. As a consequence, line widths are generally not suited for the analysis of conformational exchange.

1.6 Quantifying dynamics in the solid state: experimental challenges

The previous sections have introduced approaches to measure dynamics in the solid state. Although solid-state NMR has a great potential for studying dynamics, a couple of experimental challenges have hampered in the past its widespread use. As discussed in the previous sections, these challenges are:

- Transverse relaxation parameters are difficult to access. The reason for this is the dipolar dephasing, i.e. a decay of magnetization through coherent processes rather than incoherent

stochastic (i.e. dynamic) processes. On the one hand, this situation hampers the measurement of motion on the time scale of hundreds of nanoseconds to microsecond (through the zero-frequency spectral density). On the other hand, the fact that transverse decay parameters are most often not reflecting dynamics also hampers that analysis of µs-ms dynamics, which are routinely measured in solution through relaxation-dispersion experiments.

- Longitudinal relaxation rates may also be corrupted by the presence of coherent evolution of polarization, i.e. by spin diffusion.
- The measurement of dipolar couplings is in principle possible through methods that have been in use for decades. However, measuring dipolar couplings quantitatively is also challenging, because experimental imperfections (e.g. pulse imperfections) as well as couplings to remote spins may interfere with the accurate measurement.

On top of these difficulties to access dynamics quantitatively, it should also be mentioned that spectral resolution and sensitivity are always a serious challenge in solid-state NMR, and also interfere with the extraction of dynamic parameters on a residue-by-residue basis.
As this manuscript will show, the use of deuteration and fast magic-angle spinning resolves several of the above-mentioned problems. The following chapter briefly introduces recent developments of the use of deuteration and fast-MAS in biomolecular solid-state NMR.

2 Deuteration and fast magic-angle spinning: overcoming challenges of dynamics studies in ssNMR

The main challenges for quantifying dynamics in solids, and also for line widths (and thus resolution), can be ascribed to dipolar dephasing, i.e. the evolution of the density matrix due to large dipolar couplings. Magic-angle spinning does not allow to eliminate multiple non-commuting interactions, but these interactions are reduced by a scaling factor of $1/\nu_{MAS}$ (where ν_{MAS} is the MAS frequency). Increasing the spinning speed is thus one viable approach for reducing the effects of dipolar dephasing. An alternative and fully complementary approach to reduce the effect that the multiple couplings to protons have is to chemically remove protons and replacing them by deuterons.

The use of deuteration has become very popular over the last 10 years, following pioneering work by Zilm,[24] Rienstra[25] and Reif[26] and their respective co-workers. When I started solid-state NMR in 2008 these works have been influential for my work, and we further developed methods and applications of deuterated proteins, some of which are outlined in this manuscript. More recently, Pintacuda and co-workers have shown very elegantly the power of deuteration, fast magic-angle spinning and highest magnetic field strengths for assignment and structure determination of proteins, and applications to complex systems such as membrane proteins are rapidly emerging.[27-29] The reader is referred to recent reviews on the topic for further information.[30,31]

This chapter briefly introduces the opportunities that deuteration and fast magic-angle spinning have opened for biomolecular solid-state NMR.

2.1 Long coherence life times in deuterated proteins

In most instances, protein deuteration is combined with re-protonation of sparse sites in the protein, most often the amide sites. As a consequence, the distances between the few remaining protons are large, and accordingly the dipolar couplings between them very weak. Due to these drastically reduced dipolar-coupling network, dipolar dephasing is greatly reduced, and coherence life times are thus longer. This leads to narrow line widths of heternuclei (^{15}N, ^{13}C), but also of protons, and therefore allows direct proton detection. The high gyromagnetic ratio of protons then leads to an additional sensitivity gain. As the effect of dipolar interactions are scaled down by fast magic-angle spinning, this approach is ideally performed at fast MAS. However, even at rather moderate MAS frequencies of ~20-25 kHz very high resolution spectra may be obtained already, given high levels of deuteration.[32]

Figure 9 shows examples of proton-detected solid-state NMR spectra of microcrystalline ubiquitin, a small 8 kDa model protein. This protein is used in many of the developments and applications discussed in this manuscript. These spectra show very high resolution in heteronuclear dimensions (^{13}C, ^{15}N, line widths down to ~15 Hz), but also in proton dimensions. In addition, the sensitivity is generally high, even though these spectra were recorded with a rather small amount of sample (2.5 – 3 mg).

Figure 10 investigates ^{15}N transverse relaxation rates in a highly deuterated sample of ubiquitin. Coherence life times up to 100 ms are found for a majority of residues, which reflects the high resolution obtained in spectra in Figure 9. Remarkably, however, these coherence life times are not yet the "true" relaxation-limited coherence life times. As shown in Figure 10 (red and blue data sets), the actual expected R2 are of the order of about 5 s^{-1}. In other words, even in highly deuterated proteins at an MAS frequency nowadays dubbed "ultra-fast", dipolar dephasing still dominates the coherence decay. Nonetheless, these T_2' , which are obtained with only moderate ^{1}H

decoupling, are significantly longer than in protonated proteins, where ^{15}N T_2' are mostly below 30-50 ms,[33] and only if high-power (~100 kHz ^{1}H decoupling is used).

The high sensitivity and resolution offered by proton-detected solid-state NMR of deuterated proteins offers a number of exciting possibilities for studying biomolecular structure, dynamics and interactions.

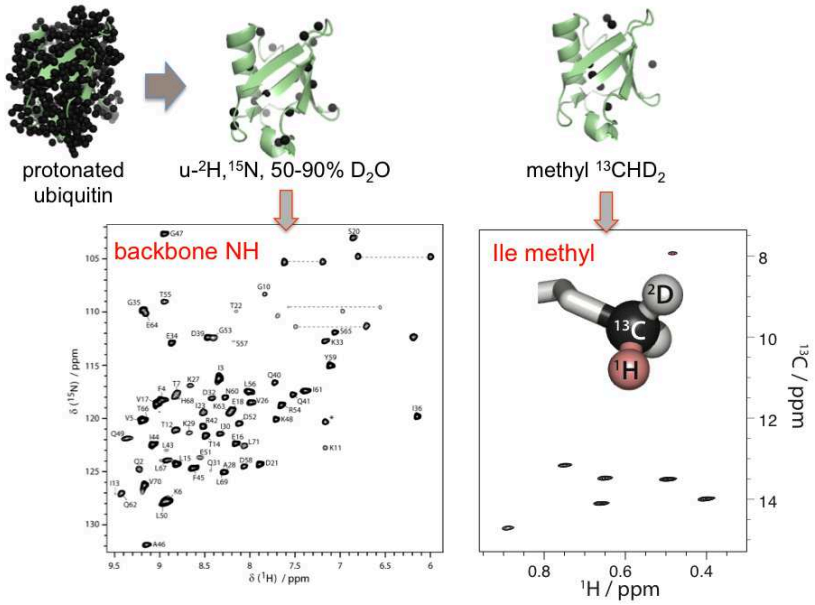

Figure 9. High-resolution proton-detected solid-state NMR spectroscopy by deuteration and fast magic-angle spinning. These data have been recorded at a static magnetic field strength of 19.9 T (850 MHz) and MAS frequencies of 50-55 kHz. Typical experimental times are of the order of 20-30 mintues.

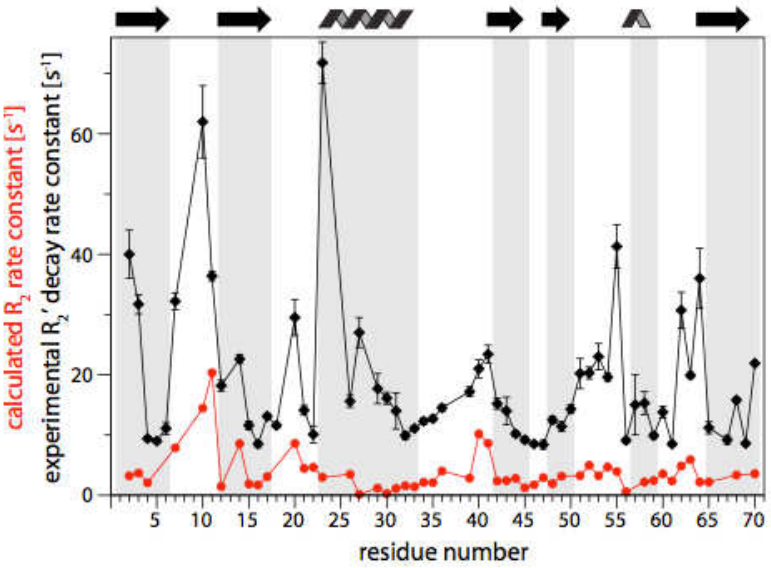

Figure 10. Transverse relaxation rate constants in a highly deuterated sample of microcrystalline ubiquitin. The experimental R_2' (black) is of the order of 10-20 s^{-1}, i.e. coherence life times of up to 100 ms. Details about the measurement scheme are presented elsewhere.[34] The red data set shows expected R_2', based on the backbone dynamics derived from dipolar-coupling and relaxation experiments (chapter 4).

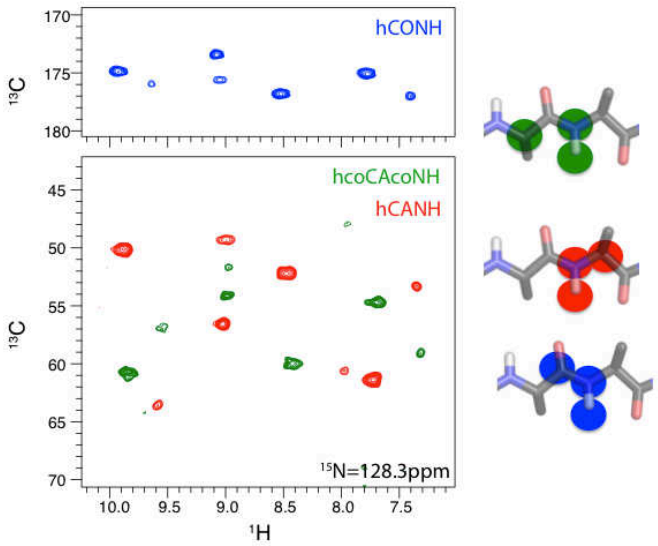

Figure 11. Sequential assignment experiments based on proton detection in the solid state. The right panels show the nuclei that are correlated in the 3D experiments, of which one plane is shown on the left. This set of three 3D experiments was obtained within 7 days of experimental time (data unpublished).

2.2 Novel types of correlation experiments: from assignment to hydrogen-bond scalar couplings

Assignment experiments in solid-state NMR traditionally relied exclusively on correlation spectra of heteronuclei, i.e. on CANCO, NCACX, NCOCX correlations and variants thereof. The possibility of detecting protons allows having an additional nucleus for increasing resolution and spreading signals. Figure 11 shows representative examples of 3D assignment experiments, recorded in 2011 on a 39 kDa protein (unpublished data). As pointed out very recently, 1H-detected assignment experiments are rather rapid, and a 3D data set (hCANH, hCONH) can be obtained within less than 12 hours with less than 3 mg of proteins. This is significantly faster than ^{13}C-detected experiments, that typically require >15 mg of protein and several days of experimental time for a 3D data set.

The long coherence life times of protonated proteins at fast MAS allow also scalar-coupling based coherence transfer experiments, rather than cross-polarization experiments. Linser *et al* have shown that in highly deuterated proteins it is possible to construct experiments that are based exclusively on scalar-coupling mediated transfer steps.[35] This type of experiments make it possible to use the scalar couplings along the backbone for assignment purposes. These couplings are of the order of 7-13 Hz, and the transfer delays are thus of the order of 25 ms. While in protonated proteins the coherence life times are typically too short for efficient transfer throughout the ~25 ms long transfer delays, the long coherence life times in deuterated samples make these experiments straightforward.

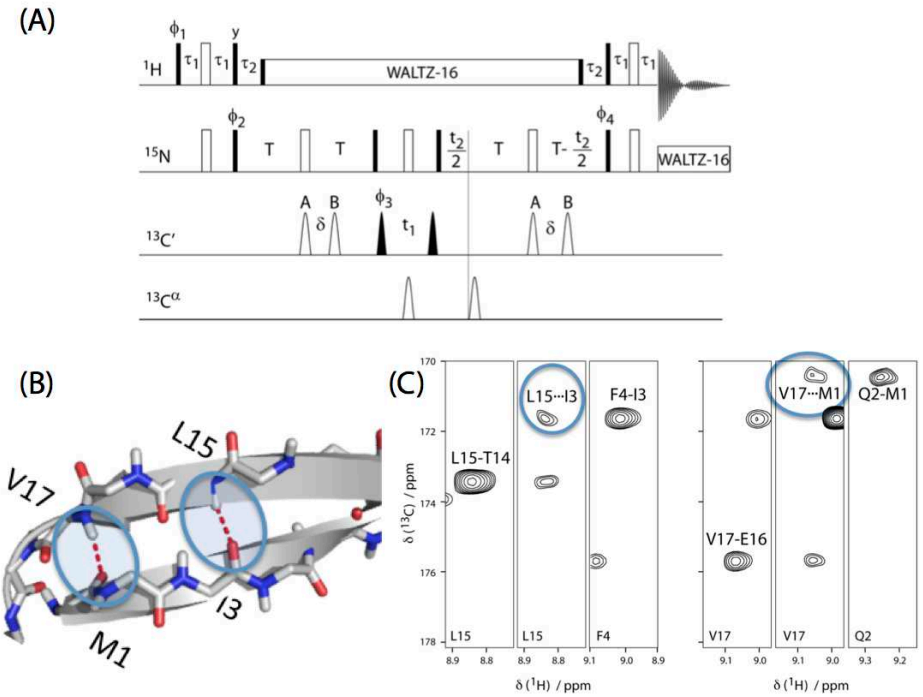

Figure 12. Direct detection of hydrogen-bond scalar couplings (3hJNC') in proteins in the solid state. (A) pulse sequence employed. The transfer delay 2T is 66.6 ms. (B, C) Experimental results obtained on microcrystalline ubiquitin at a MAS frequency of 57 kHz. Hydrogen-bond scalar couplings are evident from the cross-peaks encircled in panel (C), and are highlighted on the structure.

The most challenging experiments among biomolecular scalar-based transfer experiments are those experiments that aim at measuring very weak interaction: hydrogen-bond scalar couplings between backbone ^{15}N and hydrogen-bonded carbonyl ^{13}C are of the order of 1 Hz or less, i.e. about one order of magnitude lower than the experiments correlating nuclei along the backbone. Accordingly, the delays required for coherence transfer are long, typically of the order of hundred milliseconds. Thus, trans-hydrogen-bond scalar coupling transfer is a particular challenge. Figure 12 shows that when combining high levels of deuteration with fastest possible MAS, it is indeed possible to measure such couplings, i.e. identify the nuclei involved in the hydrogen bond, and even quantify the coupling strength, which reflects the H-bond geometry.[34]

2.3 Structure determination of deuterated proteins from unambiguous ^{1}H-^{1}H distance restraints

Protein structure determination does not have a very long and/or impressive history so far, regarding the number of structures solved or the size of the proteins for which structures were obtained (although important biological assemblies have been resolved). Structure determination has so far mostly relied on the extraction of ^{13}C-^{13}C or ^{15}N-^{13}C internuclear distances in ^{13}C-detected experiments (although 1H-1H distances are indirectly used in CHHC-type experiments[36] on protonated samples). Challenges of such experiments are typically related to the large number of structurally irrelevant intra-residue correlation peaks, and low sensitivity. The availability of highly resolved proton-detected spectra opens new opportunities for structure determination through ^{1}H-^{1}H distance measurements.

A number of advantages might arise from the use of deuterated samples. (i) When sparsely protonated samples are used, then ^{1}H-^{1}H distances necessarily correspond to long-range contacts (at least to a different residues). This is generally not the case when using ^{13}C-^{13}C contacts in uniformly ^{13}C-labeled molecules, where the majority of observed distances arise from (trivial) connectivities within the same residue. Furthermore, the large gyromagnetic ratio of protons translates to

relatively large couplings even for distant nuclei, i.e. one can expect to see longer distances than with ^{13}C-^{13}C experiments.

Structure determination using proton detection in deuterated proteins has been pioneered by Rienstra and co-workers,[25] and, simultaneously Reif and co-workers[37], and our group[#,38].
Figure 13 shows the approach we have chosen to obtain the structure of microcrystalline ubiquitin, which consists of measuring ^{1}H-^{1}H distances between amides, as well as between methyls in specifically $^{13}CHD_2$ labeled and otherwise deuterated samples. The high sensitivity of proton detection, a consequence of the long coherence life times and the high gyromagnetic ratio of ^{1}H, enabled us to obtain four-dimensional spectra, akin to solution-state HSQC-NOESY-HSQC data, which have essentially no assignment ambiguity. Details of this approach are not within the scope of this manuscript.

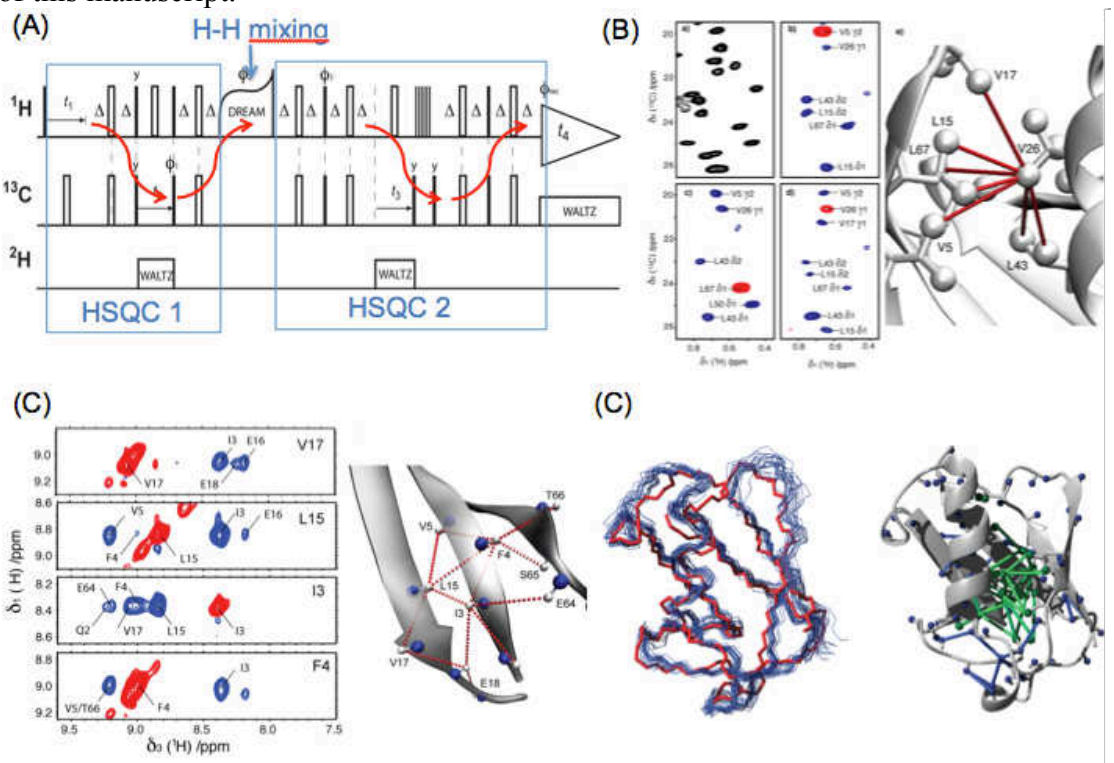

Figure 13. Protein structure determination from ^{1}H-^{1}H distance measurements for deuterated proteins at fast magic-angle spinning. (A) Pulse sequence used for obtaining methyl-methyl distance restraints from 4D data. (B) and (C) Examples of methyl-methyl and amide-amide distance restraints, respectively. (D) Structure obtained from these distance restraints, along with secondary structure information from TALOS.

In summary, the advent of proton-detected experiments, enabled by deuteration and fast MAS has opened a range of new possibilities, and has had a great impact on biomolecular solid-state NMR. In this chapter we have shown how coherence life times are prolonged in deuterated samples, and what benefit can be obtained for assignment and structure determination.
In the remainder of this manuscript we will primarily focus on opportunities to study protein dynamics with deuterated proteins.
Chapter 3 shows an approach that allows measuring dipolar couplings at unprecedented level of detail, thus enabling to characterize protein side chain mobility.
Chapter 4 focuses on time scales and amplitudes of protein backbone motion on sub-microsecond time scales. Different experimental observables are critically analyzed, and finally the impact of the protein crystal on protein motion is investigated.

[#] work presented at the International Workshop on high-field solid- and solution-state NMR, Les Houches, France. June 2009. P. Schanda: "Direct observation of ^{1}H-^{1}H dipolar recoupling in highly deuterated proteins"

Chapters 5 and 6 investigate how one can obtain information about slower processes, in which a predominant state undergoes transient excursions to low-populated “higher-energy” conformers.
Chapter 7 presents the application of (mostly) proton-detected NMR to the study of a complex of a protein with an intact peptidoglycan cell wall in terms of its structure and dynamics.
Finally, chapter 8 provides an outlook on future work planned in my group.

3 Solid-state NMR measurements of asymmetric dipolar couplings provide insight into protein side-chain motion[#]

3.1 Introduction

Understanding conformational flexibility is of critical importance for understanding protein function, folding, and interactions with other proteins and ligands. NMR spectroscopy is an important tool for such investigations in solution[1] and increasingly also in the solid state[2] since it allows site-resolved studies of dynamic processes. An experimental characterization of all motional modes of a protein is a great challenge and simplified models are necessary. In NMR studies of dynamics, motional amplitudes are generally expressed in terms of a single order parameter,[3] discarding the details of the motion, such as the motional asymmetry. In the following, we show a significant extension of this description, by detecting asymmetric motion of side chains in a protein in the solid state.
Dipolar couplings are particularly powerful probes of local molecular dynamics in the solid state. In the absence of motion, the tensor describing the dipolar interaction between two nuclei is a traceless axially-symmetric second-rank tensor. It can be characterized by a single parameter, namely its anisotropy $\delta_{D,rigid}$ which depends only on the internuclear distance and isotope type of the nuclei involved.

In the presence of "fast" motional processes, i.e., processes with a correlation time shorter than approximately $1/\delta_{D,rigid}$, (typically 10-100 µs), the dipolar-coupling tensor becomes partially averaged. In the case of a motional process with three-fold (C_3) or higher symmetry, for example, an isotropic motion within a cone, the averaged tensor remains axially symmetric and is fully characterized by the effective anisotropy δ_D which has a reduced value compared to $\delta_{D,rigid}$. In this case, the motional amplitude can be expressed by a single order parameter[4] $S = \delta_D/\delta_{D,rigid}$, such that the dipolar couplings asymmetry is given as:

$$\delta_D = S\frac{-2\mu_0}{4\pi}\frac{\gamma_k\gamma_n\hbar}{r_{kn}^3}$$

where S and r_{kn} are the order parameter and the internuclear distance, respectively.
However, in the case of a general fast motion, the characterization solely by S is incomplete because the averaged dipolar tensor is no longer axially symmetric[5] and one additional tensor parameter, the asymmetry η_D is needed for a complete description. The asymmetry η_D varies between zero (symmetric tensor) and one.[5a]
In this general case, the dipolar coupling tensor thus takes the following general form:

$$\underset{\sim}{D} = \delta_D\frac{1}{2}\begin{bmatrix} -1-\eta & 0 & 0 \\ 0 & -1+\eta & 0 \\ 0 & 0 & 2 \end{bmatrix}$$

Here, The value of the asymmetry is $0 \le \eta \le 1$, implying the following ordering of principal components of $\underset{\sim}{D}$:

[#] This work was published in: P. Schanda, M. Huber, J. Boisbouvier, B. H. Meier and M. Ernst. Solid-State NMR Measurements of Asymmetric Dipolar Couplings Provide Insight into Protein Side-Chain Motion. Angew. Chem. Int. Ed. Engl. **2011**, *50*, 11005.

$|D_{yy}| \le |D_{xx}| \le |D_{zz}|$. Thus, $\eta_D = \frac{D_{yy} - D_{xx}}{D_{zz}}$.

Note that in the case of axially symmetric motion (η=0) the dipolar coupling tensor reduces to the often assumed form, where the diagonal elements are -1, -1 and 2, as is the case for a rigid-limit coupling.

In solution-state NMR, dipolar couplings can be measured as residual couplings (RDCs) in anisotropic media. The evaluation of motional amplitudes from RDCs is challenging because RDCs also depend on the (*a priori* unknown) degree of molecular alignment and the orientation of a given vector relative to the alignment frame and usually data from different alignment media must be combined[6]. The situation is much simplified in solid-state magic-angle spinning (MAS) NMR, where overall molecular tumbling is absent, allowing the direct measurement of dipolar couplings that only depend on the interatomic distance and dynamics. For the case of one-bond dipolar couplings (C-H, N-H, or C-N) the rigid-limit dipolar-coupling tensor is known from the bond lengths. Thus, measurements of the dipolar-coupling tensor provide direct access to the amplitude and axial symmetry of the motion sampled by the bond vector. However, due to the limited precision and accuracy of the currently available experimental data, dynamically-averaged dipolar-coupling tensors have, so far, always been analyzed in terms of a single order parameter *S*. In this communication, we demonstrate the first direct measurement of asymmetric dipolar-coupling tensors in MAS NMR, providing a more detailed picture of motional amplitudes. We exemplify the measurement of asymmetric dipolar couplings by studying side-chain motions in the protein ubiquitin, using a combination of appropriate sample labeling with sensitive and precise NMR measurement techniques. We find that the asymmetry η_D of the dipolar-coupling tensor of several methyl C-H moieties deviates indeed significantly from zero and provides useful information about the details of the motional processes.

In order to obtain the necessary accuracy and precision in the measurement of ^{1}H-^{13}C dipolar-coupling tensors, we extend a recently developed experimental approach with greatly improved accuracy.[7] In brief, it consists of (i) the selective introduction of isolated ^{1}H-^{13}C spin pairs in an otherwise perdeuterated protein, using specifically protonated precursors, and (ii) a REDOR recoupling technique in combination with sensitive proton detection. REDOR has a built-in normalization[8], such that the recoupling data are expressed in a manner that is independent of the peak intensity or the coherence loss during the recoupling period and can be fitted using only δ_D (or S) and η_D as free parameters.[7]

3.2 Experimental observation of asymmetric dipolar couplings in ubiquitin side chains

We have prepared two samples of perdeuterated ubiquitin carrying ^{1}H-^{13}C spin pairs on a single methyl group of either Ile (δ1) or Val (γ1 or γ2) and Leu (δ1 or δ2) residues and we study side-chain dynamics as probed by the methyl C-H dipolar-coupling tensor. The labeling follows established protocols[9] (see Supporting Information for details). The low ^{1}H density in such samples largely eliminates ^{1}H-^{1}H couplings and couplings from the ^{13}C spins to remote ^{1}H spins, thus excluding one source of potential systematic errors in dipolar-coupling measurements. Furthermore, the low proton density allows the acquisition of high-resolution proton-detected correlation spectra with high sensitivity.[10] In combination with fast magic-angle spinning, coherences in such samples are long lived[11] leading to a further increase in sensitivity and thus precision of dipolar-coupling measurements. The improved measurement precision, the suppression of systematic errors and the normalized nature of REDOR recoupling curves are crucial to detect dipolar tensor asymmetry. Figure 14 shows how the presence of discrete jumps that result in asymmetric dipolar coupling tensors impacts REDOR recoupling curves, and Figure 15 depicts the

tensors resulting from conformational exchange in a tetrahedral geometry, such as a side chain performing rotations around the χ1 angle.

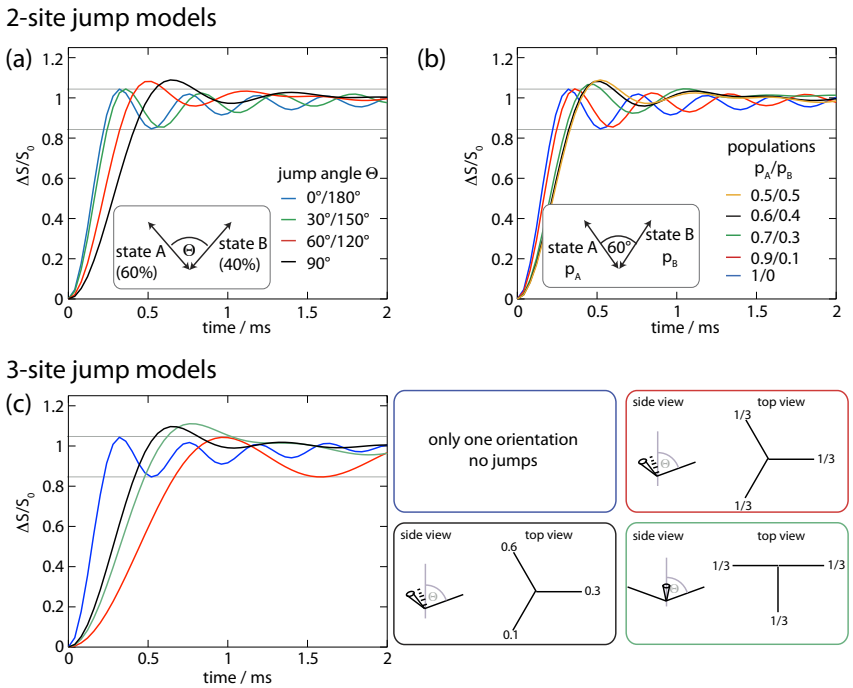

Figure 14. The effect of discrete bond jumps on REDOR curves, exemplified here for two-site (a,b) and three-site (c) cases.

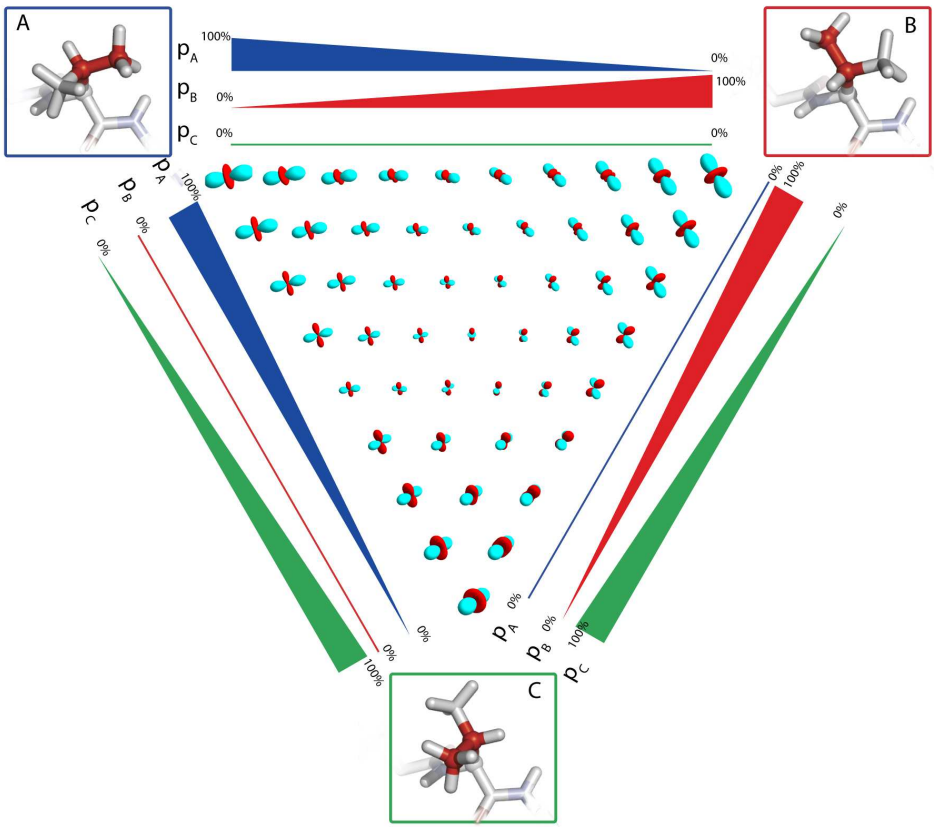

Figure 15. Dipolar coupling tensors in a system undergoing exchange between three sites (tetrahedral geometry). This is typically the case for e.g. a valine side chain. Along the three axes the relative populations of the three rotamer states are changed, and the symbols in the center depict the resulting dipolar coupling tensors. Symmetric tensors are obtained if either only one rotamer is populated (the three extremities of this plot), or if all are populated equally (center).

Figure 17a shows experimental REDOR curves for a number of representative methyl groups in ubiquitin, measured using the pulse sequence of Figure 16. The full set of experimental recoupling curves is shown in Fig. S2, and representative two-dimensional spectra are shown in Fig. S3 of the SI. The results of a two-parameter fit (anisotropy δ_D and asymmetry η_D, red curves in Figure 2a) are shown in Figure 3 and listed in Table S1. Reduced-chi-square (χ^2_{red}) surfaces are shown in Fig. 2b.

Comparing the different methyl groups in ubiquitin, a large variation in the fitted anisotropies δ_D is observed, ranging from 4.9 to 11.8 kHz, indicating that site-to-site variations of side chain motional amplitudes are large. We also detect significant variation of the asymmetries η_D between different side chains (between 0 and 0.58). Based on the fit of the anisotropy and the asymmetry to the REDOR data, the methyl groups can be classified into three groups: (i) methyl groups that have a low χ^2_{red} value and an asymmetry that is not significantly different from 0, (ii) methyl groups that have a low χ^2 value but a value of the asymmetry parameter that is significantly different from 0, and (iii) methyl groups that cannot be properly fitted (with correspondingly large χ^2 value) by a single asymmetric dipolar tensor. The majority of the methyl groups in ubiquitin (22 out of 29), such as Val5, Val17, Val26, Leu50 (Fig. 1) fall into category (i) with an almost symmetric dipolar-coupling tensor, i.e. an asymmetry below about 0.2. These methyl groups can be described by the conventional symmetric-tensor assumption. A significant asymmetry with values of $\eta \geq 0.4$ (category ii) is observed for the methyl groups of Val70, Leu67, and Leu69 (5 out of 29). For two methyl groups the asymmetric dipolar-coupling model does not result in satisfactory fits (category (iii), δ1 of Ile13 and Ile36), pointing to slow motional processes (*vide infra*). Thus, for several sites the traditional symmetric tensor model clearly does not apply, and the reported asymmetric tensors provide further insight into the motion of these side chains.

The observed dipolar tensor parameters δ_D and η_D for a methyl group are the result of several averaging processes. Invariably, at room temperature, the methyl groups are in fast rotation around the local three-fold axis with correlation times typically in the picosecond range. This rotation leads to an averaged axially-symmetric tensor with an asymmetry $\delta_{D,rigidaxis} = \delta_{D,rigid}/3 \approx 14.53$ kHz (based on the canonical tetrahedral angle $\theta_{HCC} = 109.47°$ and a C-H bond length of 1.115 Å). This tensor is further affected by motional processes involving the direction of the three-fold methyl axis, which result from librational motions, and, more importantly in terms of amplitude, jumps between discrete rotamer states. Under such fast (<10-100μs) rotamer jumps, the observed tensor is the average of the involved orientations, and will, thus, be generally asymmetric, characterized by its asymmetry η and the anisotropy δ_D or the axis order parameter $S_{axis} = \delta_D / \delta_{D,rigidaxis}$. Rotamer jumps should thus have a measurable impact on tensor anisotropies and asymmetries, and information about rotamer equilibria should be contained in the dipolar tensors. Furthermore, rotamer jumps equally affect the methyl groups γ1 and γ2 attached to a given Val, and the δ1/δ2 methyls attached to a given Leu side chain, and the tensors should thus be identical, provided that librational motions are negligible or similar to both sites. Indeed, we find that the tensor parameters for methyls attached to the same side chain always agree within error bars.

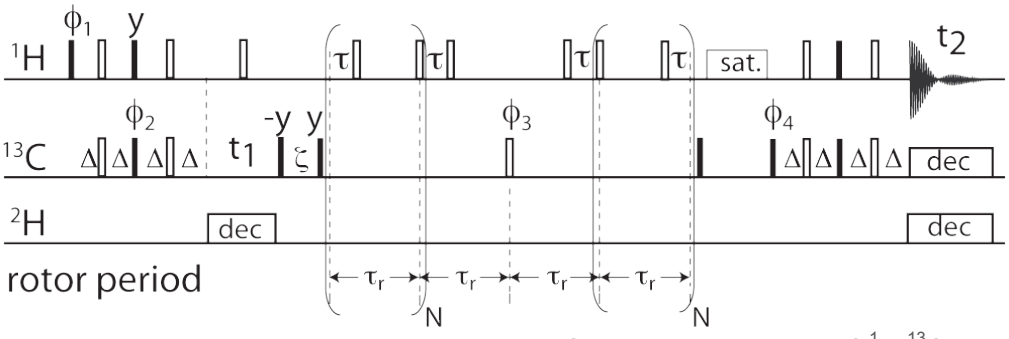

Figure 16. Pulse sequence used in this study for the measurement of ^{1}H-^{13}C dipolar couplings in highly deuterated, sparsely ^{1}H,^{13}C labeled samples. Filled and open rectangles denote 90° and 180° pulses,

respectively. Pulse phases are set to ϕ1=2(x),2(-x), ϕ2=x,-x, ϕ3=y,-y, ϕ4=4(x),4(-x), ϕrec=x,-x,-x,x,-x,x,x,-x. ^{1}H pulse phases during REDOR recoupling are incremented (decremented) according to the XY-16 scheme in the first (second) half of the REDOR block. The delays Δ, τ and ζ were set to 1.5ms, 4μs and 10ms, respectively. All pulses were applied at a field strength of γB1/2π=100kHz, except for 1H 180° pulses during the REDOR train, which were applied at 125kHz (4μs). The 1H saturation pulse ("sat.") was applied for 80ms at a field strength of about 10kHz. 2.5kHz/3kHz WALTZ-16 decoupling was applied on ^{2}H/^{13}C, respectively.

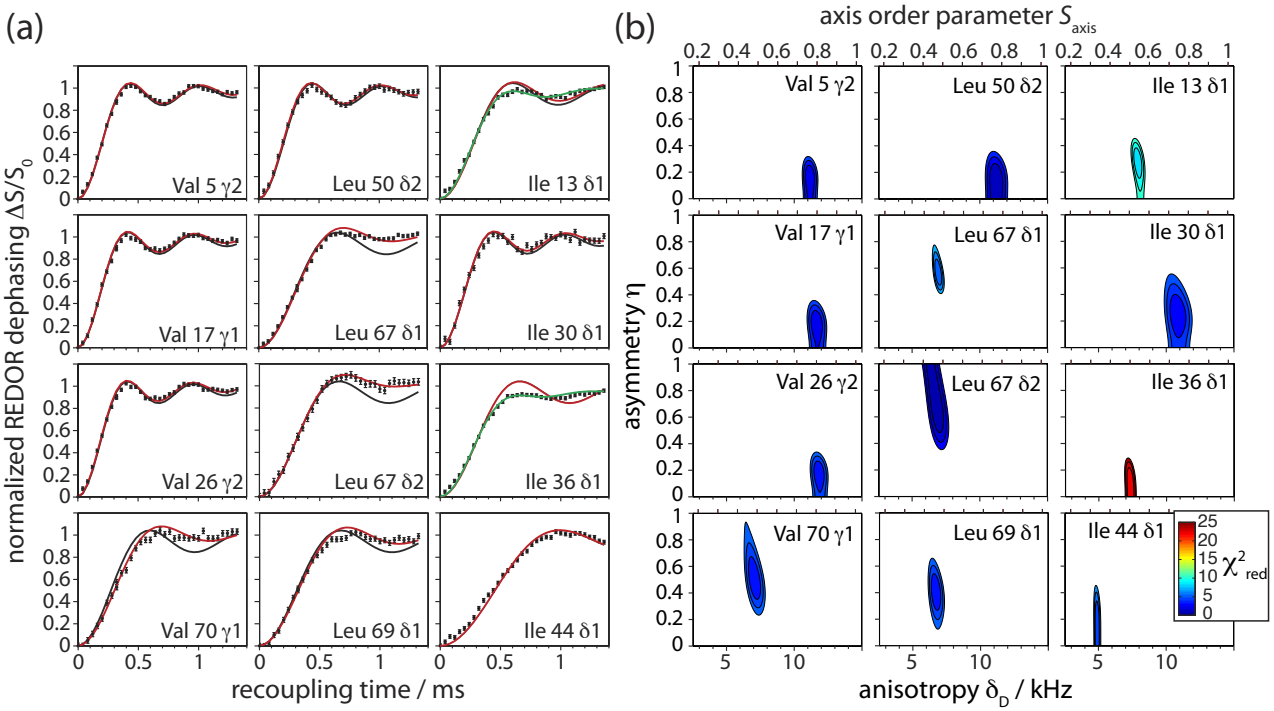

Figure 17. ***a.*** REDOR recoupling curves for methyl ^{1}H-^{13}C sites in crystalline ubiquitin. Each data point was obtained from 2D recoupling and reference spectra, recorded in 95 minutes per spectrum. Experimental points are shown along with error bars, based on twice the standard deviation of the spectral noise. Black curves show fits assuming an axially-symmetric dipolar-coupling tensor, red curves use asymmetric tensors, and green curves (only Ile13/36) assume a superposition of two general tensors. ***b.*** Plots of the reduced chi-square χ^2_{red} for the two-parameter fits of the (red) REDOR curves of Fig. 1a. Shown are three contours at the values of χ^2_{red} corresponding to the minimum of χ^2_{red} +1, +2 and +3. Thus, the innermost contour denotes the confidence interval. The full set of χ^2_{red} plots is shown in Figure S4. S_{axis} is defined as $\delta_D/\delta_{D,rigidaxis}=\delta_D/14.53$kHz.

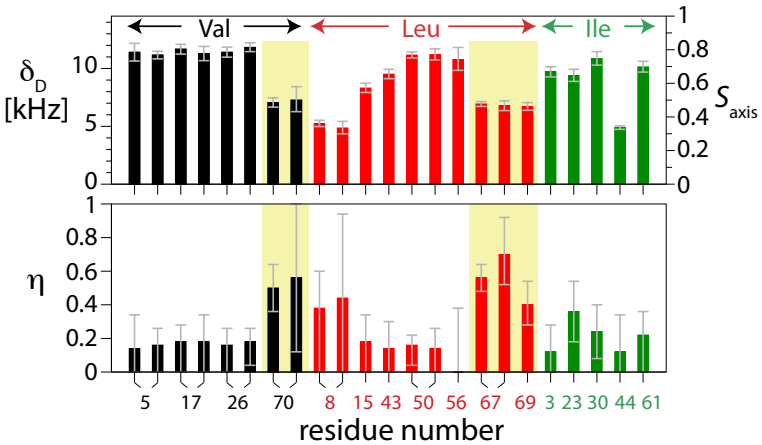

Figure 18. Dipolar tensor parameters (top: anisotropy, bottom: asymmetry) for methyl groups in ubiquitin. Two data points per residue denote methyls at positions γ1/γ2 (Val) or δ1/δ2 (Leu). Side chains with large tensor asymmetries are highlighted (yellow background).

3.3 Models of side chain motion from dipolar couplings

The significant asymmetry ($\eta \geq 0.4$) observed for some of the Val and Leu methyl groups can be rationalized when looking into the details of possible rotamer transitions for different side chains.

3.3.1 Valines

The simplest situation arises for valine side chains where a single dihedral angle $\chi 1$ is relevant. Rotations by 120° around $\chi 1$ interconvert trans, gauche(+) and gauche(-) rotamer states[12] (see Fig. 4a). Assuming that the methyl axis undergoes only transitions between these three rotameric states and neglecting any other motional processes, it is straightforward to calculate the resulting ^{1}H-^{13}C tensor parameters as a function of the populations of the three states (see Fig. 4b,c). The asymmetry in this model is zero for the case of only a single rotamer state being populated (which in this model means no mobility), or if all three rotamer states are equally populated. These two cases are readily distinguished by the tensor anisotropy, which is three times larger for the case of a single rotamer state (see also Figs. S5-S7 for examples of REDOR curves resulting from different motional models and illustrative examples).

There are four valine residues in ubiquitin. Only one of these (Val70) shows significant asymmetry, while the asymmetry for Val5, Val17 and Val26 is not significantly different from zero (see Figure 17 and Figure 20). Likewise, the order parameter S_{axis} is about 0.5 for Val70, but significantly higher (close to 0.8) for the others. The small asymmetry and high anisotropy observed for the valine residues 5, 17 and 26 can only be explained if these side chains populate primarily one rotamer state. Calculations show that these three side chains populate primarily one rotamer state (at levels of 80-90%, see Table 1). This 85% population has to be considered as a lower limit, resulting from the assumption that no librational motion is present: if part of the reduction of S_{axis} from 1 to 0.8 is ascribed to librational motion rather than rotamer jumps, an even higher population of the dominant rotamer state is calculated. For Val70 the tensor asymmetry is significantly different from zero, and the calculated populations of the three rotamer states are roughly 60, 25 and 15% (see Table 1); i.e. all three rotamer populations deviate significantly from zero within this model.

We have, thus, identified a valine side chain with significant tensor asymmetry, Val 70, which is the only surface-exposed valine in ubiquitin. We ascribed this asymmetry to jumps between unequally populated rotamers and estimated the relative populations based on dipolar-tensor parameters. The three other valines, buried in the hydrophobic core, are well described as populating only one rotamer state. It is interesting to compare our findings to data from complementary approaches. Scalar ($^{3}J_{C'C\gamma}$ and $^{3}J_{NC\gamma}$) couplings and residual dipolar couplings in liquid-crystalline media can also provide insight into the population levels and identity of side chain rotamers.[13] While the small size of the scalar couplings (below 3-4 Hz) currently makes direct measurement in the solid state difficult, a solution-state study has used residual dipolar couplings in two alignment media and ^{3}J scalar couplings to investigate side chain rotamer jumps.[14] Interestingly, Val5, Val17 and Val26 were found to populate primarily one single rotamer state in solution, while in Val70 all three rotamer states are populated to similar extents as found here (Table 1). Remarkably, these findings in solution state are in good agreement with the picture arising from the dipolar coupling tensors found in the present study.

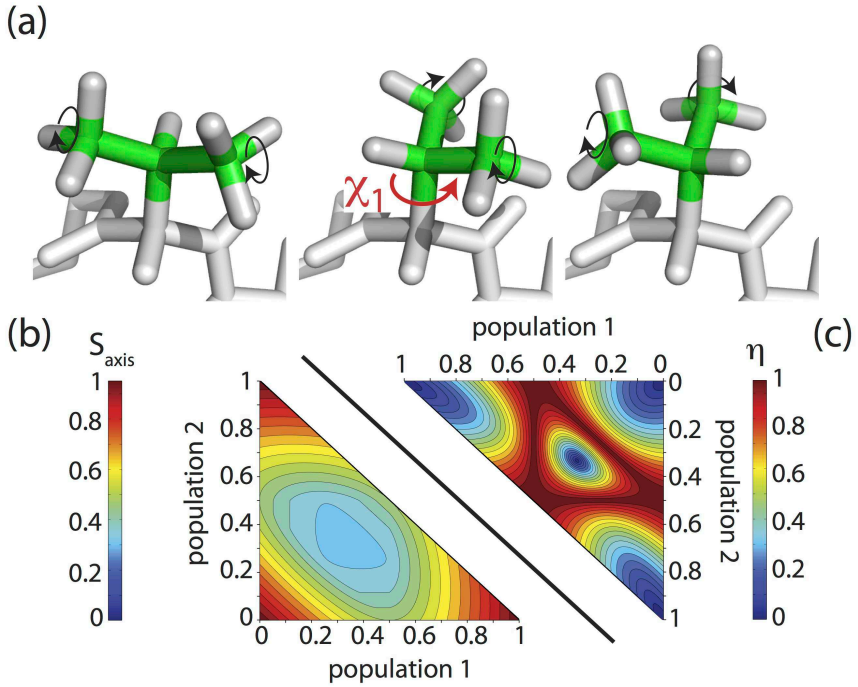

Figure 19. (a) Rotamer transitions in the valine side chain. Fast methyl rotations (black arrows) and jumps around χ1 are considered. (b) Calculated methyl ^{1}H-^{13}C tensor anisotropy $\delta_D/\delta_{D,rigidaxis}$ and (c) asymmetry η for the three-site jump model of the methyl axis around χ1, as a function of the population levels of the three rotamer states p_1, p_2 and p_3=1-p_1-p_2.

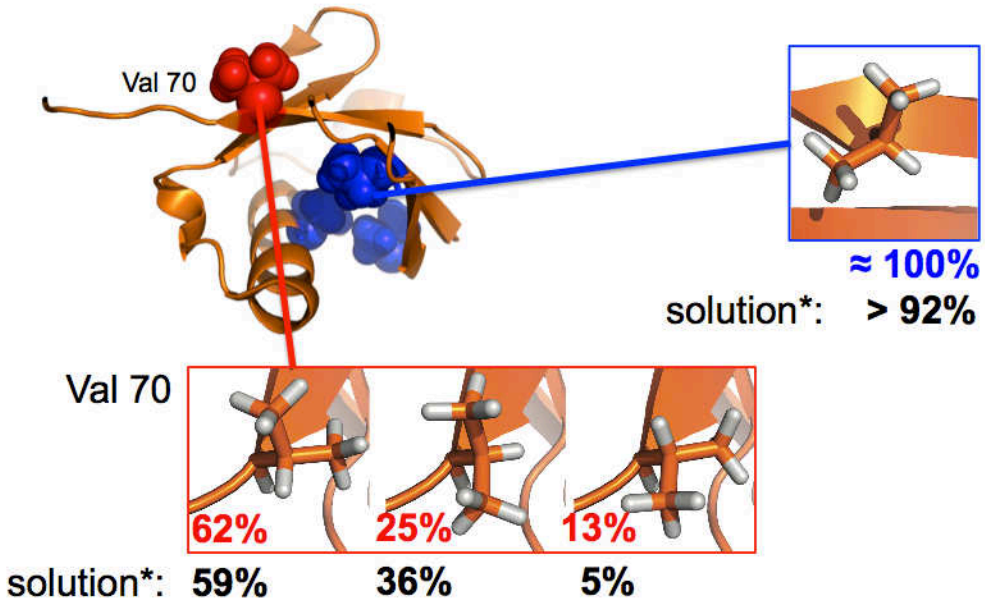

Figure 20. Valine side chain rotamer jumps in ubiquitin, as observed by asymmetric dipolar couplings (this study) and solution-state NMR data.[39] Note that our data do not allow to assign which of the rotamer states (trans, gauche+, gauche-) has which population, and the structure figures shown in the insert are based on solution-state NMR J couplings.[39]

3.3.2 Leucines

Jumps around two side-chain dihedral angles (χ1, χ2) have to be considered for Leu. Clearly, the complete characterization of such motions based on only the ^{1}H-^{13}C dipolar-coupling tensor of the

terminal methyl groups is difficult and in general ambiguous. In general, the measurement of several dipolar coupling tensors along the side chain would be needed. In Leu side chains, however, jumps around χ1 and χ2 are highly correlated, and these side chains populate primarily two states. We have, thus, attempted to interpret the dipolar-coupling parameters for the two Leu side chains that show significant asymmetry (Leu67, Leu69), in the framework of such a simple two-site jump model (see Figure 21). Based on the relations shown in Figure 4, the observed asymmetry η_D for Leu67 and Leu69 (see Figure 1 and Table S1) points to population levels of roughly 70% to 30% (see Table 1). However, these populations would result in tensor anisotropies that are higher than the ones found experimentally. We speculate that the model used here, where only transitions between two rigid conformations are considered is too simplistic, and that additional librational motions are present that give rise to this observed reduction of the anisotropy. To date, no scalar-coupling based rotamer populations have been reported in solution state for these residues.

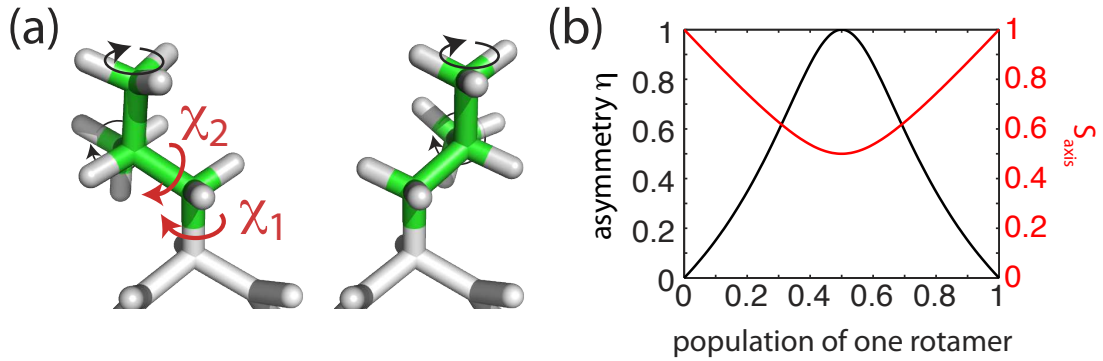

Figure 21. (a) Transitions between two rotamer states in Leu side chains, resulting from correlated jumps around χ1 and χ2 (b) Resulting dipolar coupling tensor parameters for the methyl group as a function of the population of one of the two states. Numerical expressions are shown in the Supporting Information of reference [40].

3.3.3 Isoleucines

As in Leu, two torsion angles (χ1, χ2) are necessary to decribe the sidechain motion as probed by the methyl group δ1. However, several rotameric states corresponding to different combinations of χ1, χ2 are generally populated to significant amounts[12, 15-16] requiring more experimental parameters to accurately describe the motion, and we refrain from deriving rotamer populations from a single dipolar coupling measured on the δ1 site. The REDOR curves of two side chains (δ1 methyl groups of Ile13 and Ile36, Figs. 2a and 1b) could not be fit satisfactorily by a single dipolar-coupling tensor. The minimum reduced chi-square values for these sites are 8 and 22, respectively. There are two possibilities to explain the fact that a general asymmetric dipolar coupling cannot explain these data:
(i) a conformational exchange process that is slow (i.e. occurring at an exchange rate smaller than the coupling strength, i.e. slower than ~10 μs), between two or more conformations. Such a process would lead effectively to a (weighted) superposition of REDOR recoupling curves. We consider the simplest possible model of two exchanging sites, each described by a general dipolar-coupling tensor. A fit with such a model leads to a good description of the experimental curves with a χ^2_{red} of 2.6 and 3.1 for Ile13 and Ile36, respectively (green lines in Figure 17). This improvement is statistically significant, as investigated by an F-test.[40]
(ii) Alternatively, the curves might also be explained by a dynamic process in which two or more conformations interconvert on a time scale that is similar to the inverse of the coupling strength (i.e. on time scales of hundreds of nanoseconds to a few microseconds). As shown in Figure 5, such a intermediate timescale motional process would also effectively "flatten out" the REDOR curves.

Table 1. Rotamer jumps for Val/Leu side chains in ubiquitin as derived from dipolar coupling tensors.

Side chains	Population ranges derived from dipolar coupling measurements [%][b]			Populations derived from solution-state NMR measurements [%][c]		
Valines[a]	p_1	p_2	p_3	p_1	p_2	p_3
5 (γ2)	81–88	6–19	0–9	92±3 (g−)	6±2 (t)	2±2 (g+)
17 (γ1)	83–87	6-17	0-8	96±3 (t)	4±3 (g−)	0±2 (g+)
26 (γ2)	82–86	7–16	0–8	100±1 (g−)	0±1 (g+)	0±3 (t)
70 (γ1)	58–63	20–29	9–18	59±10 (t)	36±11 (g−)	5±5 (g+)

Leucines	p_1[b,d]	p_2[b,d]	S_{axis}, expected from p_1/p_2[b]	S_{axis}, experimentally observed [b]
67 (δ1)	68–74	26–32	0.6–0.67	0.46–0.49
67 (δ2)	57–73	27–43	0.51–0.66	0.44–0.47
69 (δ1)	80–83	17–20	0.74-0.77	0.44–0.49

[a] Data for the two equivalent methyl groups on the same side chain are in agreement, and only one is reported. [b] Confidence limits of the populations were derived from confidence intervals of η and S_{axis}. [c] Data as reported in Ref. [14]. t, g+, and g− denote *trans*, *gauche*+, and *gauche*− rotamers, respectively. [d] Populations within the model of Figure 5, derived only from values of η.

3.3.4 Possibilities of studying other side chains, and characterizing side chain motion in even more detail

In this study we have only used methyl groups residing on the end of the side chain to characterize the motional processes. Accordingly, the availability of only two tensor parameters for each terminal methyl position may not allow to detect more complex modes of motion or distinguish between different models. Our approach can be extended to other moieties in the protein backbone and along the side chains. Having access to more coupling tensors will allow the characterization of the side-chain and backbone mobility at higher precision and with less ambiguity. Measuring the dipolar-coupling tensors at multiple positions, in combination with selective or sparse labeling[17] will allow the separation of small-amplitude fluctuations (librations) and rotamer jumps around different dihedral angles and thus provide a comprehensive picture of backbone and side-chain motion. Importantly, a single experiment provides this information simultaneously for many sites, covering a wide range of time scales, as contrasted by studies of motional asymmetry in solution[18], requiring several experimental parameters and interpretation within motional models.

In conclusion, we have shown for the first time that MAS solid-state NMR spectroscopy allows an accurate determination of dipolar-coupling tensors in terms of both the anisotropy and the asymmetry. The hitherto never exploited information about dipole tensor asymmetries provides direct access to the characterization of dynamics, as exemplified here with the exchange between side chain rotameric states. Such large-scale motions may be crucial to the function of membrane proteins[2d] and other proteins in the solid state.

4 Time scales and amplitudes of protein backbone dynamics in the solid-state[#]

Conformational flexibility is a key prerequisite for function and stability of proteins. A comprehensive description of protein function, therefore, requires not only information about the static ground-state structure, but also information about the thermally accessible conformational space, which can be obtained in the form of amplitudes and time scales of conformational fluctuations. NMR spectroscopy has emerged as a very successful tool to study protein dynamics in solution[1-3] because of its ability to provide residue-resolved insight into the dynamics over a wide range of time scales. Relaxation measurements in solution state are routinely used to probe fluctuations on time scales shorter than the overall molecular-tumbling correlation time, i.e., shorter than about 5 ns[4]. Motions in the microsecond to millisecond regime can be probed by T_2 or $T_{1\rho}$ relaxation-dispersion experiments[5,6]. The time window from the overall tumbling correlation time up to microseconds (i.e., the nanosecond window) is inherently inaccessible in isotropic solution, but can be studied by an analysis of residual dipolar couplings (RDCs), measured in at least five different samples with different molecular alignment. [7-10]

Spectral resolution and sensitivity of solid-state NMR has recently reached a point that allows structural studies of crystalline proteins[11-15] and non-crystalline samples such as amyloid fibrils[16-20] or membrane proteins in a native-like environment.[21,22] These achievements also form the basis for studying protein dynamics with residue resolution in solids[18,23-31] that complement and extend studies using single-site labeling approaches, as used for low temperature measurements.[32,33] The absence of overall molecular tumbling opens new possibilities for the study of dynamics. Firstly, the full range of time scales of internal motions is visible in solid-state NMR relaxation measurements in contrast to solution-state NMR relaxation measurements where all information about internal dynamics that are slower than the overall tumbling are masked. Dynamics on a nanosecond to microsecond time scale which may involve significant structural rearrangements and can be of functional relevance, can, therefore, be characterized quantitatively in terms of amplitudes and time scales. Secondly, anisotropic interactions such as dipolar couplings are not averaged to zero and their magnitude can be measured. Of particular interest is the dipolar coupling between directly bonded nuclei, such as side-chain or backbone C-H or amide N-H dipolar couplings, for which the rigid-limit value can readily be calculated without any knowledge of the 3D structure from the almost constant bond length. The measurement of these one-bond dipolar couplings leads to a direct determination of order parameters, S, that characterize the amplitude of motions occurring on time scales up to the inverse of the coupling strength, i.e., typically up to microseconds.

Here we present a comprehensive study of the backbone dynamics of the protein ubiquitin over time scales from picoseconds to several microseconds. In order to obtain residue-resolved order parameters and time scales of backbone dynamics in the crystal, we use the combined information from ^{1}H-^{15}N dipolar couplings and ^{15}N relaxation data. A large set of data is then used to fit motional models, and comparisons to solution-state data investigate the effect that the crystal lattice may have on ubiquitin's motion.

[#] This work was published in Schanda, P.; Meier, B. H.; Ernst, M. *J Am Chem Soc* **2010**, *132*, 15957 and Haller, J. D.; Schanda, P. *J Biomol NMR* **2013**, *57*, 263.

4.1 Proton-detected spectroscopy on ubiquitin: assignments and qualitative conclusions about dynamics

We have used a perdeuterated sample of ubiquitin in microcrystalline form, protonated at 30% of the exchangeable hydrogen sites, to record scalar-coupling based ^{1}H-^{15}N and ^{1}H-^{15}N-^{13}C correlation spectra. Figure 3a shows a ^{1}H-detected ^{1}H-^{15}N HSQC spectrum. A total of 63 out of the 76 residues in ubiquitin could be observed. From a set of scalar-coupling based HNCA, HNCO and HN(CO)CA experiments[72], all amide cross peaks in the ^{1}H-^{15}N spectrum were assigned site specifically[16]. Missing correlation peaks can be an indicator of line broadening induced by dynamics in the corresponding regions and are investigated more closely. Besides the proline residues that do not bear an amide ^{1}H and the N-terminal residue, the non-observable resonances (shown in Figure 3b) are located in the loop connecting the first two β-strands (L8 and T9), in the α-helix (E24 and N25) and in the C-terminus (residues 72-76). It is noteworthy that the residues located in the first loop as well as the C-terminal residues are also unobservable in dipolar-coupling based solid-state NMR experiments [73,74]. While this observation could be attributed to a strong motion-induced reduction of the dipolar couplings, which makes dipolar-coupling based transfer steps in such experiments inefficient, the fact that these correlation peaks are also invisible in scalar-coupling based experiments points to different mechanisms.

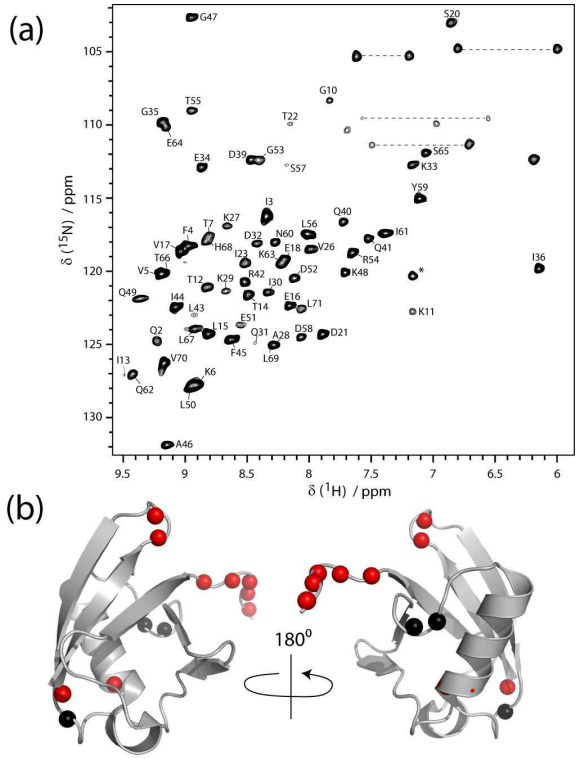

Figure 22. (a) ^{1}H,^{15}N correlation spectrum obtained for the highly-deuterated ubiquitin sample used in this study, measured at 301 K at a magnetic field strength of 19.96 T and a MAS frequency of 45 kHz. Residue-specific resonance assignment is indicated. A cartoon representation of the backbone structure is shown in (b). Amide sites for which no ^{1}H,^{15}N cross peaks are observable (M1, L8, T9, E24, N25, R72, L73, R74, G75, G76) are depicted as red spheres and proline residues are shown as black spheres. Note that residue M1 is not observable in solution either, because of fast solvent exchange. The cross peak of I13 is weak in CP and J-coupling based spectra.

A number of dynamic scenarios could explain the broadening of some peaks beyond detection. One possibility is the presence of conformational-exchange processes on microsecond-to-millisecond time scales, that involve states with different chemical shifts. This situation would lead to an apparent increase in the transverse relaxation-rate constant, also referred to as "exchange contribution to R_2".[4] Alternatively, Redfield relaxation through dipolar and CSA mechanisms could

also be the origin of the line broadening, assuming that the amplitude is relatively large or the time scale is long. In this case, one expects that ^{15}N CSA, ^{1}H-^{15}N dipolar cross-correlated relaxation is efficient, and one might be able to recover some of the signals using TROSY-type spectroscopy, depending on the exact nature of the motion in terms of amplitudes and time scale.[48] Such a scenario has been observed in solid-state NMR, where TROSY-type techniques resulted in significant enhancement and sharpening of signals broadened almost beyond detection in experiments using decoupling.[48] As a third possible scenario, static disorder or exchange between different states on time scales much slower than the chemical-shift difference of the involved states could also be an explanation for the disappearance of the cross peaks. In this scenario, the signal would be distributed over several states with different frequencies (or a continuum of states), which can result in very broad lines below the detection limit.

To further investigate the origin of the disappearance of cross peaks in microcrystalline ubiquitin, we have measured the transverse decay-rate constant, R_2', at high magic angle spinning frequency (57 kHz) (see Figure S13 in the Supporting Information). Although in the solid state this rate constant not only depends on incoherent relaxation processes, but also contains contributions from coherent broadening mechanisms, which prohibits a rigorous analysis in terms of dynamics, it is interesting to note that the observable residues in the first loop (T7, G10, K11) show significantly faster transverse decays than other residues in the protein. This suggests the presence of dynamics in this region that leads to line broadening of the unobservable residues L8 and T9 either through chemical-shift modulation or enhanced Redfield-type relaxation. The observation of efficient ^{15}N CSA, ^{1}H-^{15}N dipolar cross-correlated relaxation in observable residues in this loop region (*vide infra*) suggests that the latter scenario is at the origin of the line broadening. Residue I23, preceding the unobservable residues E24 and N25, also displays enhanced transverse dephasing. However, it does not show significantly increased cross-correlated relaxation as compared to other secondary structure elements. In solution state it has been found that this N-terminal part of the α-helix displays conformational exchange dynamics on a microsecond time scale in solution, as probed by $T_{1\rho}$ experiments[75] and multiple-quantum experiments.[76] [77] It is tempting to speculate that this conformational exchange dynamics is preserved in the solid state, providing an explanation for the invisibility of residues E24 and N25 in HSQC spectra. The reasons why the C-terminal residues are unobservable remains unclear, because there is no clear evidence of enhanced transverse relaxation or cross-correlated relaxation in the residues preceding this region.

Finally, we considered the possibility that missing cross peaks can be recovered by the use of TROSY spectroscopy,[48] or experiments performed at different temperatures. However, neither a TROSY experiment[78] (recorded at 14.09T, 28°C) nor scalar-coupling based 2D experiments at lower (5°C) or higher temperature (35°C) revealed any additional cross peaks.

4.2 Insight into sub-microsecond backbone motion from experimental data: theoretical considerations

Different approaches have been proposed in recent studies of protein dynamics, as to which type of the above data should be used for determination of motional parameters, as well as to how these experimental data should be acquired [16,20,41-43], and even whether they should be interpreted in terms of local or global motion [44]. In this manuscript, we systematically investigate ways to determine backbone dynamics in proteins using various longitudinal and transverse ^{15}N relaxation rates, as well as ^{1}H-^{15}N dipolar coupling measurements. Figure 1 shows the computed relaxation rate constants for ^{15}N longitudinal relaxation R_1, and transverse relaxation, i.e. R_2 (that can be obtained at fast spinning from $R_{1\rho}$ measurements [20]), and ^{1}H-^{15}N dipole/^{15}N CSA cross-correlated relaxation [45] (in the following denoted briefly as "CCR"), as a function of the amplitude of motion and time scale within the simple model-free (SMF) approach. These relaxation rates are shown for time scales ranging from picoseconds – a time scale often found in solution-state analyses of local backbone fluctuations – to microseconds, where the Redfield theory reaches its limit of validity [17].

These plots show that R_1 relaxation is most sensitive to motion on time scales of nanoseconds, as expected from its dependence on $J(\omega_N)$; both R_2 and the dipole-CSA cross-correlated relaxation are sensitive to motions on time scales exceeding about 1ns (leading to a measurable relaxation rate of about 1 s^{-1}). For completeness, Figure 1 also shows the information content from dipolar couplings measurements, which directly reflect the motional amplitude, independently of the time scale.
The measurement of a single relaxation rate yields only very limited information, constraining the amplitude and time scale of motion to all combinations of S^2 and τ falling on a given contour line in Figures 1a, b, d. Obtaining amplitudes and time scales of motion from relaxation data requires the measurement of several relaxation data. Due to the different dependencies of longitudinal and transverse relaxation rates on motional parameters, it may be possible to derive these parameters from measurement of R_1 and R_2/CCR measurements at a single static magnetic field. In addition, one may complement such data with measurements at different field strengths, as these relaxation rates (slightly) depend on the field strength (see Supporting Information in [16]). To investigate how well such an approach would perform in practice, we calculated in-silico relaxation rates for a number of dynamic scenarios, and subjected them to a fit routine, assuming realistic error margins on the rate constants.

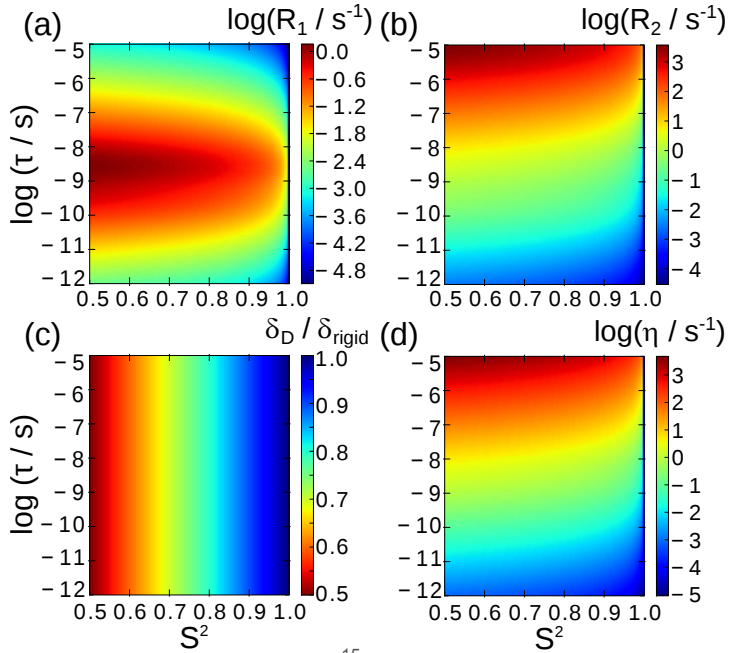

Figure 23. Dependencies of (a) longitudinal ^{15}N relaxation rates R_1, (b) transverse relaxation, R_2, (c) ^{1}H-^{15}N dipolar order parameters, given as the ratio of measured and rigid-limit dipolar coupling, and (d) ^{1}H-^{15}N dipole-^{15}N CSA cross-correlated relaxation rate constants on the amplitude and time scale of motion in the framework of the simple model-free description.

To this end, we have assumed a N-H bond vector that undergoes motion that is described by one order parameter and one time scale (SMF). Relaxation rates and dipolar couplings were back-calculated for different settings of S^2 and τ, random noise was added and the data were fit with the SMF formalism. Figure 2a-d show the results of such fits for the case that the motion is in the picosecond range (a,b), or in the nanosecond range (c,d). If only relaxation data are used (panel a), and if the motion is fast then the fit does not provide reliable results, and the order parameter is very poorly defined. Given the insensitivity of transverse relaxation parameters to fast motion (see Figure 23), this behavior is expected. Interestingly, even the inclusion of relaxation data at multiple fields does not significantly improve the situation, and the uncertainty of the fit remains essentially the same (data not shown). If the motion is in the nanosecond range, the use of relaxation data alone provides reasonable estimates of the motion (Figure 24), as transverse relaxation data contain information about motion on this time scale. The situation is generally greatly improved if dipolar coupling data are available (Figure 24b,d), and in this case both the time scale and the order parameter are correctly obtained, irrespective of the time scale of motion.

It appears unlikely that the backbone exhibits only one single motional mode over the range of time scales that the experimental observables are sensitive to (ps-μs). Therefore, we performed a similar investigation, assuming two distinct motional modes, within the extended model-free approach (EMF). As above, various values of amplitudes and time scales of the two motional modes were assumed. The resulting back-calculated relaxation rate constants were fitted with the SMF and EMF approach. Here we assumed that the total order parameter is constant, and the two order parameters, S_f^2 and S_s^2, are varied. The results of such fits, are shown in Figure 24e,f. If only relaxation data are used, and the data are fitted with the SMF approach, then the resulting order parameter is always overestimated. This overestimation is particularly pronounced if the underlying motion is predominantly fast, i.e. if S_f^2 is low (and, according to our assumption, S_s^2 is high). Again, this reflects the fact that relaxation data alone are not capable of correctly picking up fast motion. This mirrors recent studies, where the analysis of relaxation data showed systematically overestimated order parameters [20,46].

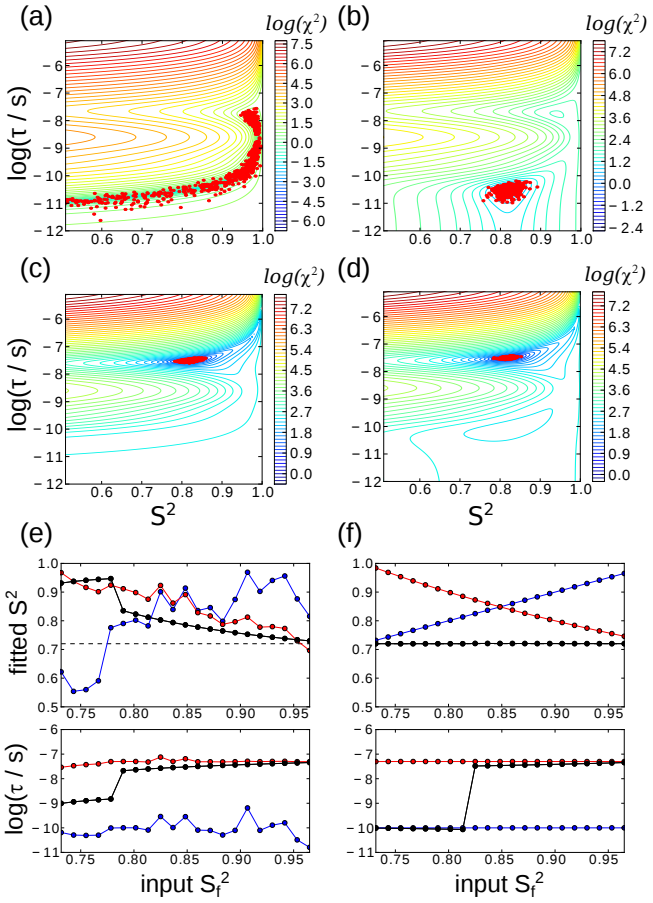

Figure 24. Investigation of the robustness of fitting the amplitude and time scale of motion from different types of data. The left column shows fits using relaxation data alone, while the right column shows fits of relaxation and dipolar-coupling derived order parameters. In (a) and (b), a single motion, with order parameter S^2=0.82 and τ=3.2*10^{-11} s was assumed. From these parameters, ^{15}N relaxation rate constants (R_1, R_2 and η) were back-calculated at a static magnetic field strength of 14.09T via the model-free approach. In panel (a), these three relaxation rates were fitted in the framework of the SMF approach. Shown is the χ^2 surface of obtained from a grid search. A rather poorly defined minimum extending over a wide range of S^2 values is found. Red points shown the best fits of 2000 Monte Carlo runs, obtained from varying these synthetic relaxation rates within error margins of 0.009 s-1 for R_1, 0.46 s^{-1} for R_2 and 1.57 s^{-1} for η, which are typical average values found in the present and a previous study [16]. The swallow minimum of the target function results in a large error margin on S^2 in such a Monte Carlo error estimation. In (b) the dipolar order parameter is added to the relaxation data, greatly improving the accuracy and precision of the determined motional parameters. The error margin on the dipolar order parameter S^2 ($(\delta_D/\delta_{D,rigid})^2$) was 0.018. The dipolar coupling was treated equally as the relaxation data, as in Eq. 5. In (c) and (d), the same analysis is performed with S^2=0.82 and τ=3.2*10^{-8} s.

Fitting the EMF model to relaxation data only essentially fails, as the parameter space is not sufficiently restrained, as was also reported elsewhere [46]. Given that in these analyses a total of 6 relaxation data were used, with 3 magnetic field strengths, it appears unlikely that the addition of even more static magnetic field strengths will improve the situation significantly.
The inclusion of dipolar coupling data changes this situation significantly, as shown in Figure 24f. The order parameter is directly given by the dipolar coupling and therefore, trivially, this value is always correctly retrieved. In the EMF case, the two individual order parameters, S_f^2 and S_s^2, as well as the two correlation times are all correctly obtained. When these data are fitted within the SMF approach, i.e. an oversimplified model, then necessarily the motion is either fast or slow. Interestingly, the fitted correlation time obtained in the SMF fit is very close to one of the two values assumed (lower panel in Figure 24f). Whether the SMF fit retrieves a fast motion or a slow motion depends on their relative amplitudes, S_f^2 and S_s^2, i.e. the fitted τ jumps the fast to the slow regime once the amplitude of the slow motion exceeds a certain level.
These in-silico considerations show that relaxation data alone, even if measured at multiple field strengths, do not provide satisfactory fits, and often lead to systematic errors of order parameters, as sub-nanosecond motion cannot be detected properly with this approach. Only if dipolar couplings are measured, accurate data can be obtained. In the following section we, therefore, investigate how dipolar couplings, which are crucial for obtaining reliable measures of motion, can be measured at high accuracy.

4.3 Amplitudes of backbone motion from NH dipolar couplings

A number of recoupling sequences have been proposed for the measurement of heteronuclear dipolar couplings in proteins, in particular TMREV (Helmus et al. 2010; Hohwy et al. 2000), R18 sequences (Hou et al. 2011; Hou et al. 2013; Levitt 2002; Yang et al. 2009), phase-inverted CP (Chevelkov et al. 2009b; Dvinskikh et al. 2003), DIPSHIFT (Franks et al. 2005; Munowitz et al. 1981) and REDOR (Gullion and Schaefer 1989; Schanda et al. 2010). A detailed description of these pulse sequences and their relative merits and weaknesses is not within the scope of this manuscript. We have recently investigated the robustness of most of these different experimental approaches with respect to experimental artefacts, such as rf field mis-settings and remote spin effects [56], by extensive numerical simulations. The primary source of systematic experimental errors in most of these approaches are mis-set rf field strengths employed during the recoupling pulse train, as well as the inevitable rf inhomogeneity. Notably, systematic errors on δ_D in the range of several percent are easily incurred in many of these recoupling approaches, even if the rf fields are only slightly offset. A notable exception seems to be the case of an approach based on R-sequences, which have been reported to be more robust, at least if samples are center-packed and if three-different experiments are measured and fitted simultaneously [51].
In the present case of dynamics measurements a systematic error even of only a few percent is a major concern: as the motional amplitude is reflected by $(1-S^2)$, an error of a few percent on δ_D, and thus, S (thereby quadratically impacting S^2) can easily lead to an error of the motional amplitude, $(1-S^2)$, by several tens of percent. In the numerical analysis of different measurement schemes, a time-shifted REDOR approach [16] turned out to be the most robust approach, provided proper calibration of the RF fields. REDOR has the additional advantage that fitting is very robust and straightforward: as the data are obtained in a normalized manner (using a reference experiment), one can fit the data with a single parameter (the dipolar coupling of interest). Most other approaches require fitting signal intensities and line widths (and a zero-frequency component in the dipolar spectrum, that is often left our from the fit in a somewhat arbitrary manner) along with the dipolar coupling. These factors motivated our choice to focus here on the REDOR approach, and investigate experimentally how accurately the obtained order parameters can be measured, and how mis-settings of ^{1}H and ^{15}N π pulse power impact the apparent measured dipolar coupling. The REDOR approach is akin to the one shown in Figure 16, except for the use of CP steps instead of INEPT.

Figure 25 shows experimental dipolar coupling data obtained on microcrystalline ubiquitin. Representative REDOR curves for individual residues are shown in Figure 26. These data were obtained taking into account the ^{1}H rf inhomogeneity. Figure 25 shows three different data set. The red data set was obtained on a different spectrometer, different sample and different probe and different pulse programming language than the other two. In the red and blue data sets, calibration was performed with a somewhat lower degree of accuracy, and the rf inhomogeneity was ignored. In Figure 25b these two data sets are shown without any scaling, while in panel (a) a global scaling parameter has been applied to minimize the offset to the black data set, which is the one described above (with rf field inhomogeneity correction and very accurate pulse calibration). Clearly, the data sets with less accurate rf field calibration are systematically lower than the data set that was obtained from the rf calibration and rf inhomogeneity treatment explained above. An underestimation in the other data sets is expected, as any miscalibration and rf inhomogeneity leads to underestimated dipolar couplings[57]. It is interesting to note, however, that if the data sets are scaled by one global scaling factor, as shown in panel (b), the agreement is excellent. This shows that the method yields highly reproducible results for the order parameter profile, even though the data were collected on different samples, different probes and different spectrometers.

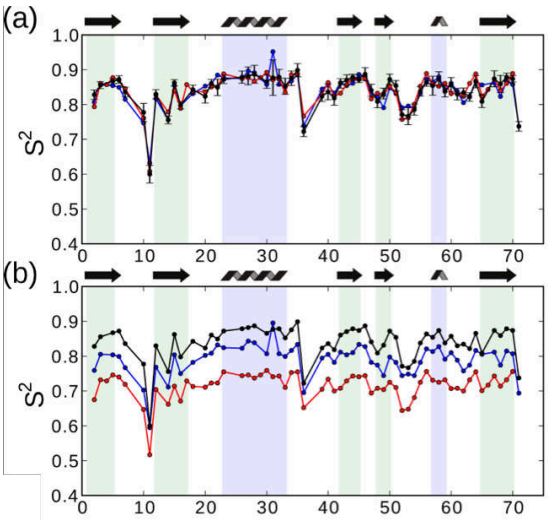

Figure 25. ^{1}H-^{15}N dipolar-coupling derived order parameter in ubiquitin, obtained as $S^2=(\delta_{D,exp}/\delta_{D,rigid})^2$. Plots of S^2 are preferred rather than S or $\delta_{D,exp}$, as possible offsets and differences are accentuated in such an S^2 plot. (a) Measured dipolar-coupling derived S^2 obtained in this study, with the pulse sequence in Figure 3a, accurate ^{1}H π pulse calibration as described in Figure 3, and correction for the ^{1}H rf inhomogeneity are shown in black. The data in red are the data previously published [16], and data shown in blue were data obtained in this study, with a different phase cycling of the ^{1}H π pulses (see Figure S1 in the Supporting Information), and somewhat less accurate ^{1}H pulse calibration. In (b) the latter two data sets are scaled with one global scaling factor as to reduce the offset to the black data set. The scaling factor that was applied to the values of S shown in the red data set was 1.084, and the factor used for scaling the S values of the blue data set was 1.031. The good reproducibility of the data is evident. Note that the data set shown in red is, itself, already an average over three independent measurements, which themselves show high reproducibility of the S^2 profile [56].

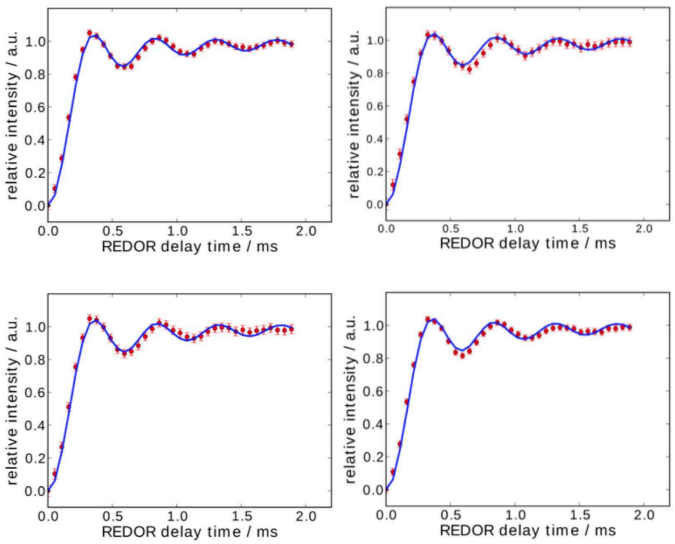

Figure 26. Representative REDOR recoupling curves of the 1H-15N dipolar coupling measurement. The blue lines have one single fit parameter, the D coupling.

4.4 Time scales of backbone motion: insight from different spin relaxation parameters.

In the following, we explore how the available relaxation data and dipolar couplings can be interpreted in a physical model of backbone motion. Altogether, we use up to 7 data sets (in cases of resonance overlap, for some residues less data may be available).

- ^{15}N R_1 at field strengths corresponding to 500, 600 and 850 MHz ^{1}H Larmor frequency
- ^{1}H-^{15}N dipole-^{15}N CSA cross-correlated relaxation at 600 and 850 MHz [16]
- ^{15}N $R_{1\rho}$ at 600MHz (this study, values reported in the Supporting information)
- ^{1}H-^{15}N dipole couplings (this study, values reported in the Supporting information)

As in the theoretical section above, we use either the one-time scale simple model free[58] or the two-time scale extended model-free approach [59].

Figure 27 shows fit results for the SMF approach, using three different implementations. In one case, only the 6 relaxation data sets were used; S^2 are reported as red curve in (a) and the corresponding τ shown in panel (b)). In another implementation, dipolar couplings were added to the fit, but the fitted S^2 was not imposed to match the dipolar-coupling derived one; rather, all relaxation and dipolar-coupling data were equally used for a χ^2 minimization, according to Eq. 5 (S^2 shown as blue data set in panel (a), τ in panel (c)). Finally, a similar fit was performed, but this time the order parameter was fixed to the dipolar-coupling derived value (black curve and panel (d)).

If only relaxation data are used, the obtained order parameters are systematically overestimated, as compared to the dipolar order parameter. Furthermore, the time scale of motion is in the nanosecond range for all residues. This overestimation of S^2 by relaxation data, as well as the finding of nanosecond motion only is in agreement with the above in-silico data (Figure 24). Although there is no physical foundation for such an approach, one might be tempted to search for a scaling factor, that would bring the relaxation-derived S^2 to the level of the dipolar ones. Mollica et al. have shown that for their data set on GB1, that a scaling factor of 0.96 results in reasonable agreement with MD-derived order parameters. We have applied a similar procedure, and find that a scaling factor of 0.967 results in an overall similar level of order parameters, while a factor of 0.93 leads to best match for secondary structure elements. However, this apparent similarity merely reflects the fact that the backbone mobility tends to have a similar level throughout the protein, so it is always possible to find a scaling factor that makes these levels look similar.

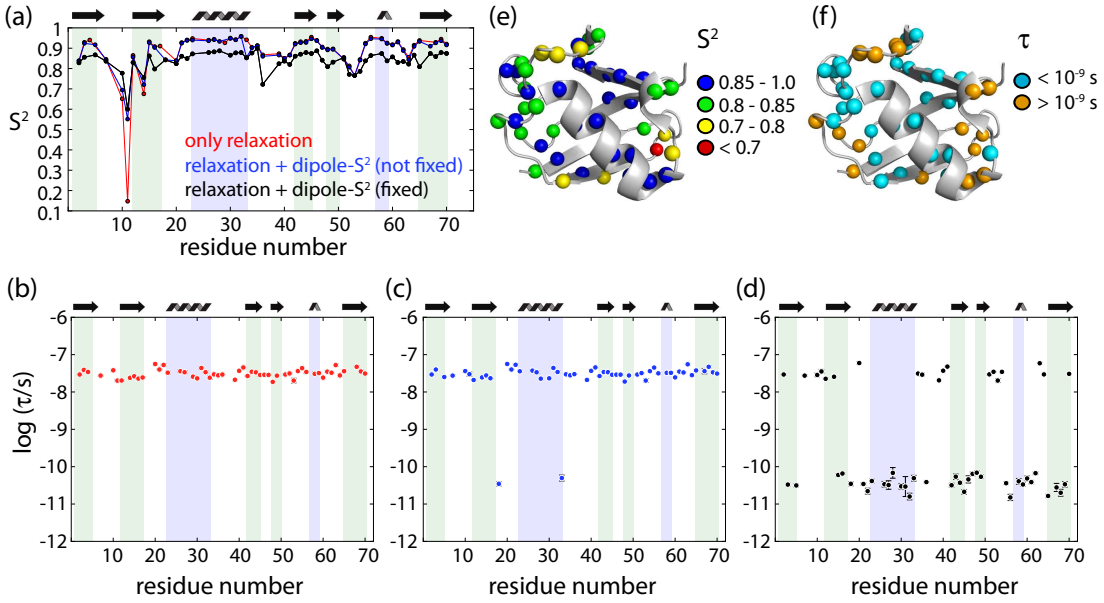

Figure 27. SMF fit of relaxation and dipolar coupling data in ubiquitin. (a) Results from fitting only relaxation data (up to 3x R_1, 2x η and 1x $R_{1\rho}$ per residue) are shown in red. Inclusion of dipolar coupling data results in the blue data set. In this data set, the order parameter was not fixed to the dipolar order parameter, but the dipole coupling was included in the fitting of S^2 and τ in the same manner as the relaxation data, as shown in Equation (3). In the black data set, the order parameter was fixed to the dipolar-coupling derived value. (b), (c) and (d) show the fitted time scales for the three scenarios, using the same color code. The fitted order parameters and time scales from the fit where S^2 was fixed to the dipolar-coupling derived value (black curves) are plotted on the structure in panels (e) and (f). In the fits that included dipolar coupling data, a minimum of 3 data points was required for a residue to be considered; in the fit with relaxation data only, a minimum of 4 data points was required.

Interestingly, if dipolar couplings are added to the SMF fit, but treated in the same manner as relaxation data (i.e. S^2 is not fixed to its dipolar-coupling derived value), the situation does not greatly improve, and a similar level of S^2 is found as if only relaxation data are used (blue data set in Figure 27). This reflects the fact that the larger number of relaxation data outweighs the contribution from the dipolar data in the target χ^2 function. If S^2 is fixed to the REDOR-derived value, which are in close agreement with solution-state S^2 (see Figure Figure 31), an interesting pattern of correlation times is observed, where values of τ fall either in the fast or the slow regime (Figure 27d). This clustering basically corresponds to τ values falling either above or below the regime where the ^{15}N R_1 is maximum (see Figure 23). Interestingly, residues for which we observe a slow motional time scale correspond almost exclusively to loop regions, while the residues for which the SMF fit shows a picosecond motion are mostly located in secondary structure elements. This observation is in line with the fact that loop motions are generally the result of concerted motion of several residues, which is a more rare event than localized motion. Of note, the fit that used only relaxation data did not detect this feature, and all the residues showed only motions on long time scales (tens of nanoseconds). Similar findings of exclusive nanosecond motion were reported also in previous relaxation-based analyses [60]. Based on the in-silico analyses, and on the comparison with the fit including dipolar coupling data, we conclude that this detection of exclusively slow motion for all residues is essentially an artifact arising from fitting relaxation data only.

The SMF approach is tempting for its small number of fit parameters, which makes it applicable even if only one field strength is available. However, the assumption that backbone motion over 6 orders of magnitude in time can be described as a single process appears too simplistic. From a physical point of view, it seems more realistic that for those residues that exhibit slow motion in Figure 27d, the slow motion dominates, rather than being exclusive. We tried to investigate how the simultaneous presence of slow and fast motion would impact a SMF fit procedure. To this end, we performed an analysis extending on the above theoretical considerations of Figure 24f. We assumed that the actual motion can be described with the (somewhat more realistic) EMF model; we systematically varied all the parameters of the model (S^2_f, S^2_s, τ_f, τ_s), back-calculated relaxation and

dipolar-coupling data from these parameters, and then fitted them through an SMF approach. A representative plot of these data is shown shown in Figure 29. Whether the SMF-derived correlation time falls into the slow or fast regime not only depends on the relative amplitudes of slow and fast motion, but also on the correlation times. For example, in the case that the time scale of the slow motion is long (hundreds of nanoseconds) the SMF fit would find a slow motion even if the amplitude of that motion is much smaller than the amplitude of the simultaneously present fast motion. This is expected, as large transverse relaxation rate constants can result even from very low-amplitude motions, as long as the time scale is long enough. We also note that the plot shown in Figure 29 does not depend on the total amplitude of motion, but only on the fast-motion correlation time, τ_f.
We conclude from this analysis that our finding of slow motion for a number of loop residues in ubiquitin (Figure 30d) does not mean that there is no fast motion in the concerned regions, nor does it necessarily mean that the amplitude of slow motion is larger than the amplitude of fast motion, as both the time scale and the amplitude are decisive for whether slow motion is detected in the SMF fit.

We also fitted the more complex EMF model with two motional time scales to our data (i.e. 4 fit parameters). If only relaxation data are used, even if measured at multiple fields (6 data sets in our case), the fit results in an underdetermined parameter space, i.e. very large error bars, and physically rather unrealistic fit parameters, such as high order parameters (data not shown).
Figure 30 shows results of an EMF fit to relaxation and dipolar-coupling data. A number of physically intuitive patterns emerge from this fit. Slow-motion order parameters tend to be lowest in loop regions, while some secondary structure elements have S_s^2 close to unity; the lowest fast-motion order parameters are found in loop regions, similar to solution-state analyses. The time scale of fast motion is in the range of tens to hundreds of picoseconds, while slow-motion correlation times are in the range of tens of nanoseconds for most residues, while for some residues we find values up to about one microsecond. The EMF fit also shows some features that are physically less intuitive. For example, residue 10, located in a loop and exhibiting enhanced transverse relaxation, has a slow-motion close to unity, but a very long correlation time. It's neighbor, residue 11, has a significantly lower S_s^2, and a correlation time that is one order of magnitude shorter.
A statistical analysis of the two fit models, SMF and EMF, using F-test reveals that the EMF model is the accepted model for a 31 out of the 46 residues (data not shown here). In contrast, however, a Akaike Information Criterion test rejects the EMF model for all residues (data not shown). To get further information about the robustness of the EMF fit, we systematically eliminated individual data sets from the fit. The results of these fits, reveal that many of the features are retained if data sets are eliminated, e.g. the amplitude of slow motion is generally smaller than the fast-motion amplitude. However, when seen at a per-residue level, the relative amount of fast vs slow motion, as well as the correlation times, vary in some cases substantially when data sets are eliminated, even for residues that are fitted significantly better with EMF (according to an F-test). As expected, the SMF model is much more robust to elimination of individual data sets, and the fitted correlation time is hardly sensitive, at least as long as both longitudinal and transverse relaxation data are available.

Getting a large set of relaxation data, in particular measurements at multiple field strengths, is often impracticable. Practical problems with multiple-field measurements include the availability of multiple NMR magnets, and fast-MAS probes at the different magnets (as the relaxation rates are best measured at fast spinning), and possibly the need for preparing multiple rotors for the different probes, which may cause problems of comparability of different preparations. In addition, the temperatures in different measurements on different probes may not be exactly identical. Therefore, we investigated the information that can be obtained from fitting data collected at only one magnetic field strength, i.e. using only ^{15}N T_1, ^{15}N $R_{1\rho}$ and ^1H-^{15}N dipole couplings. We left out the dipolar-CSA CCR data, as their information content is similar to the on of $R_{1\rho}$, while in our hands the latter can be measured with higher precision.

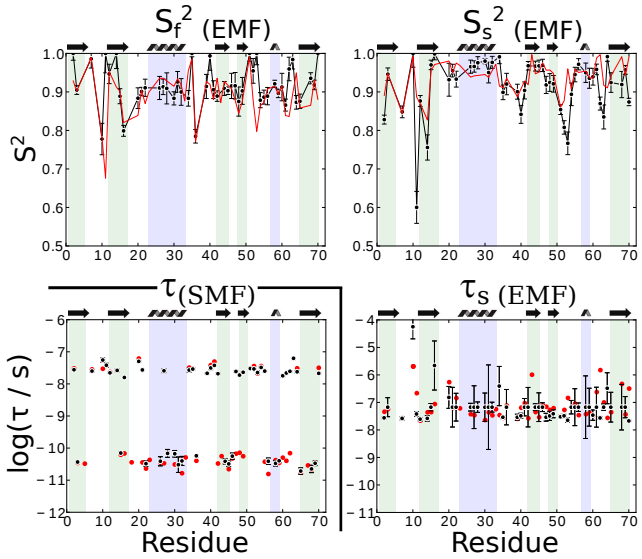

Figure 28. Model-free fits from data obtained at a single magnetic field strength (14.09 T), using dipolar-coupling derived S^2, R_1 and $R_{1\rho}$. Shown are fitted parameters for the SMF and EMF cases. In both cases, the overall order parameter, i.e. the S^2 in SMF, or $S_s^2 * S_f^2$ in EMF, was fixed to the dipolar S^2. In the SMF case, only the time scale is shown, as S^2 is identical to the data shown in Figure 5. In the EMF case, the time scale of fast motion, τ_f, was fixed to 80 ps, as the number of fitted parameters would otherwise exceed the number of observables. Fits using other assumed τ_f are shown in the Supporting Information Figure S8. For comparison, the fit parameters obtained from a fit of all available experimental data (up to 7) are shown in red. In these fits, for all residues three data sets were used (R_1, R_2, S^2).

Figure 28 shows results from such fits. In the case of SMF, the obtained fitted correlation times agree remarkably well with the ones obtained from the full data set that comprises 6 relaxation rates (instead of 2 used here). Note that in this fit the relaxation data serve only to constrain the correlation time, as the order parameter is defined by the dipolar-coupling measurement.

We also investigated EMF fits from a limited data set. Obviously, fitting four parameters from three experimental data sets is impossible. However, our finding of rather uniform values of τ_f (data not shown) prompted us to set τ_f to a fixed value for all residues. Figure 28 shows EMF fit results for the case of τ_f=80ps. Despite the very limited data set, the fitted parameters are in relatively good agreement with the fit that uses the entire data set. However, the choice of the τ_f value has a clear impact on these fits (data not shown here), such that such an approach must be interpreted with some care.

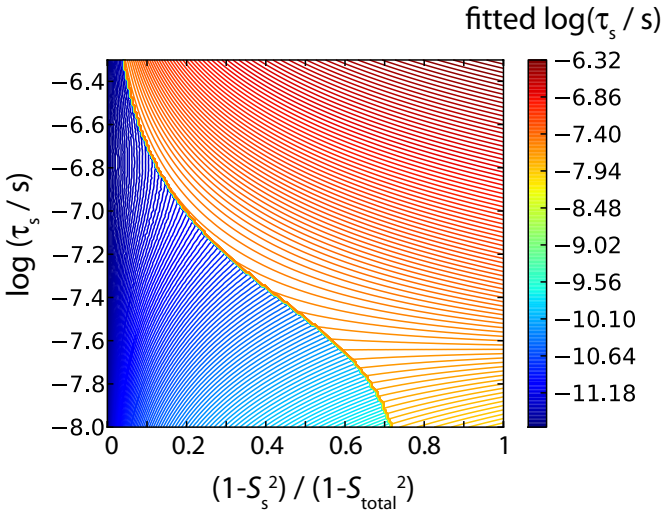

Figure 29. Investigation of the outcome of SMF fits when applied to a two-time scale motion. Shown is the fitted correlation time of motion in an SMF fit, applied to in-silico relaxation (R_1, $R_{1\rho}$ at 600MHz) and dipolar-coupling data, calculated from an EMF model. The slow time scale, τ_s, used in the EMF model, is shown along the vertical axis, while the amplitude of the slow motion, $(1-S_s^2)$, relative to the the total amplitude of motion, $(1-S_{total}^2)$, where $S_{total}^2=S_f^2*S_s^2$, is shown along the horizontal axis. The correlation time of fast motion, τ_f, was assumed as $2*10^{-12}$s.

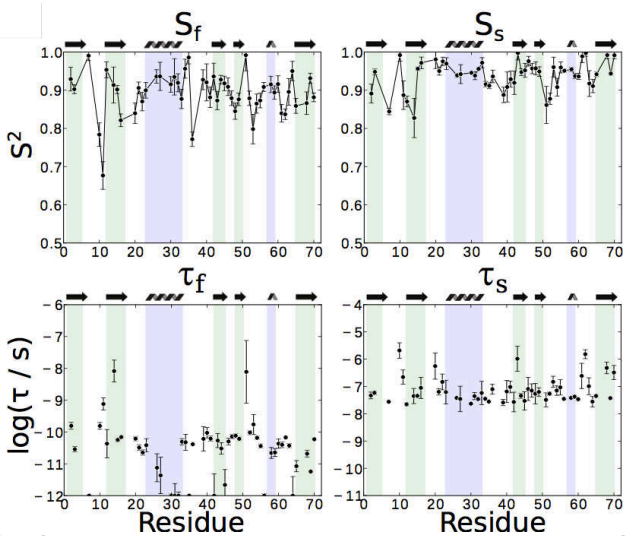

Figure 30. EMF fit of relaxation data and dipolar couplings. In these fits, the overall order parameter $S^2_s*S^2_f$ was fixed to the REDOR-derived value. In all fits a minimum of 4 data points was requested per residue, residues for which fewer data are available were discarded.

4.5 Comparison to solution-state NMR: does the crystal lattice impact protein dynamics?

The solid-state sample investigated in this study is a densely packed three-dimensional crystal. Although protein crystals contain a large amount of water (approximately 50 % of the volume), intermolecular contacts may alter the dynamics. Figure 31 compares the amplitudes of motion on time scales of picoseconds to a few microseconds, as seen by REDOR, with solution-state relaxation-derived order parameters, which are sensitive to a smaller time window, reaching from picoseconds up to a few nanoseconds only.

The order parameters obtained from these different techniques on different protein sample states are remarkably similar. This finding, that mirrors also similar findings in the protein SH3 [61], indicates that the protein exhibits overall very similar sub-microsecond motion in crystals and in solution. There is a notable exception to this finding, however: residue 62, located in the α2-β5 loop, shows

large-amplitude motion in solution, but appears rigid in the crystal. We will address this issue below (section 4.6) by comparing different crystal polymorphs.

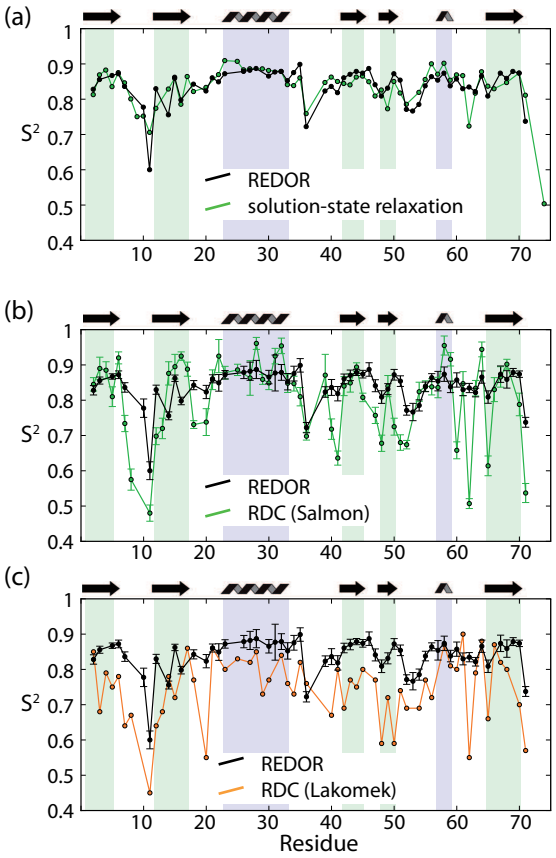

Figure 31. Comparison of REDOR-derived order parameters with different solution-state order parameters of internal motion: (a) relaxation-derived S^2 [62], (b) RDC-derived S^2 values in solution, using two different approaches, according to [63] (a) and [64] (b).

In recent years, a number of studies have addressed protein dynamics in solution from residual dipolar couplings (RDCs). RDCs are sensitive to motion on time scales from ps to ms, and thus overcome the limitation of solution-state relaxation measurements. Due to difficulties to disentangle the amount of alignment in anisotropic solution, the structural component to the RDC, and the amount of dynamics, RDC analyses are challenging. Solid-state dipolar couplings might provide complementary insight, as they are only sensitive to local motion, but not to the structure [61]. It is, thus, interesting to compare our present dipolar-coupling data to order parameters from solution-state RDC analyses. Of course, one does not necessarily expect perfect agreement between these data sets, because dynamics may be impacted by the crystalline environment. Figure 31 b/c shows the comparison of REDOR-derived S^2 with S^2 derived from an extensive set of RDC data, analyzed with two different approaches [63,64]. Overall, the amplitude of motion seen in our REDOR data appears to match better the data set shown in (a) [63] than the one in (b) [64]. In both cases, a number of notable differences can be seen between solution-state RDC order parameters, and REDOR order parameters. Notably, the RDC-derived order parameters have much more site-to-site variation. This may appear surprising, as the solution-state relaxation-derived order parameters agree much better with the solid-state REDOR order parameters (panel a). For a number of residues (e.g. residues 60, 62, 65) the RDC data show markedly lower RDC-order parameters than the REDOR data. One possible explanation could be found in the presence of motion on time scales between the one relevant for solid-state (~10μs) and solution-state (~10ms). In fact, there is some experimental evidence for motion in ubiquitin on a time scale of 10μs [65]. This microsecond motion was, however, detected there for a small set of residues, and these data may not provide an explanation for all residues for which we observe lower RDC order parameters. Somewhat unexpectedly also, in the

RDC data set that matches the REDOR data apparently better (in terms of overall motional amplitude), there are a few residues that have rather large order parameters, i.e. values of S^2(RDC) exceeding the REDOR order parameters (see panel b). In these cases the RDC order parameters also exceed the solution-state relaxation-derived value (which is sensitive to sub-nanosecond motion). This is an unphysical situation, as has been noted before [63], and it has been speculated that uncertainties in the relaxation order parameters may be the origin. Although we cannot exclude this possibility, the good match of solution-state relaxation data with REDOR data seems to weaken this argument. An alternative explanation to both the large site-to-site variation of RDC-order parameters, and the unphysically high values might also lie in uncertainties in the determination of the RDC order parameters. Our new dipolar coupling data might be useful as a benchmark for continued development of approaches to analyze RDC data. As has been pointed out previously, the REDOR data might also be compared directly to solution-state order parameters, and differences might be interpreted in terms of ns-µs motion [61].

4.6 The impact of the crystalline environment from comparisons of different crystal polymorphs

The above comparisons of the dynamic behavior of ubiquitin in crystals vs solution indicated that the crystalline environment has only little impact on sub-microsecond motion. Nonetheless, some differences, e.g. for residues 62 were detected, that might reveal the impact of the crystal. The methodologies used – solution vs solid-state approaches – and the time scales they probe are different, so the observed differences in order parameters might rather point to methodological differences rather than changes in dynamics. This prompted us to perform experiments on different polymorphs of ubiquitin, and apply exactly the same methodology.

To this end we prepared another crystal form of ubiquitin, obtained with poly-ethylene glycol (PEG) and zinc acetate. The obtained crystals have two non-equivalent molecules in the unit cell, and we indeed obtain two sets of chemical shifts in the spectrum (Figure 32). We used proton-detected as well as carbon-detected experiment to obtain the residue-specific assignment, which is shown in the right panel of Figure 32. Details of the preparation and the assignment procedure are not within the scope of this manuscript.

Figure 32 shows the comparison of order parameters and ^{15}N R_1 relaxation rates in two ubiquitin polymorphs. Overall, the parameters, in particular R1 rates, are very similar – except for two regions: the β1-β2 loop (residues 10/11) and the α2-β5 loop (residue 62). The former has large-amplitude motion in MPD-crystals (black), but restricted motion in PEG-crystals, while the opposite is the case for the α2-β5 loop. Interestingly, the difference in the α2-β5 loop is also evident from the comparison to solution-state order parameters (Figure 31): this loop is flexible in solution and in PEG-crystals, but rigid in MPD-crystals.

4.7 Conclusions

In this chapter, we have provided a detailed analysis of some approaches for determining protein backbone motion on time scales from picoseconds to microseconds, both from the perspective of simulated data, as well as from a rather extensive set of experimental data, including previously unpublished data sets of ^{15}N $R_{1\rho}$ data as well as ^{1}H-^{15}N dipolar couplings.

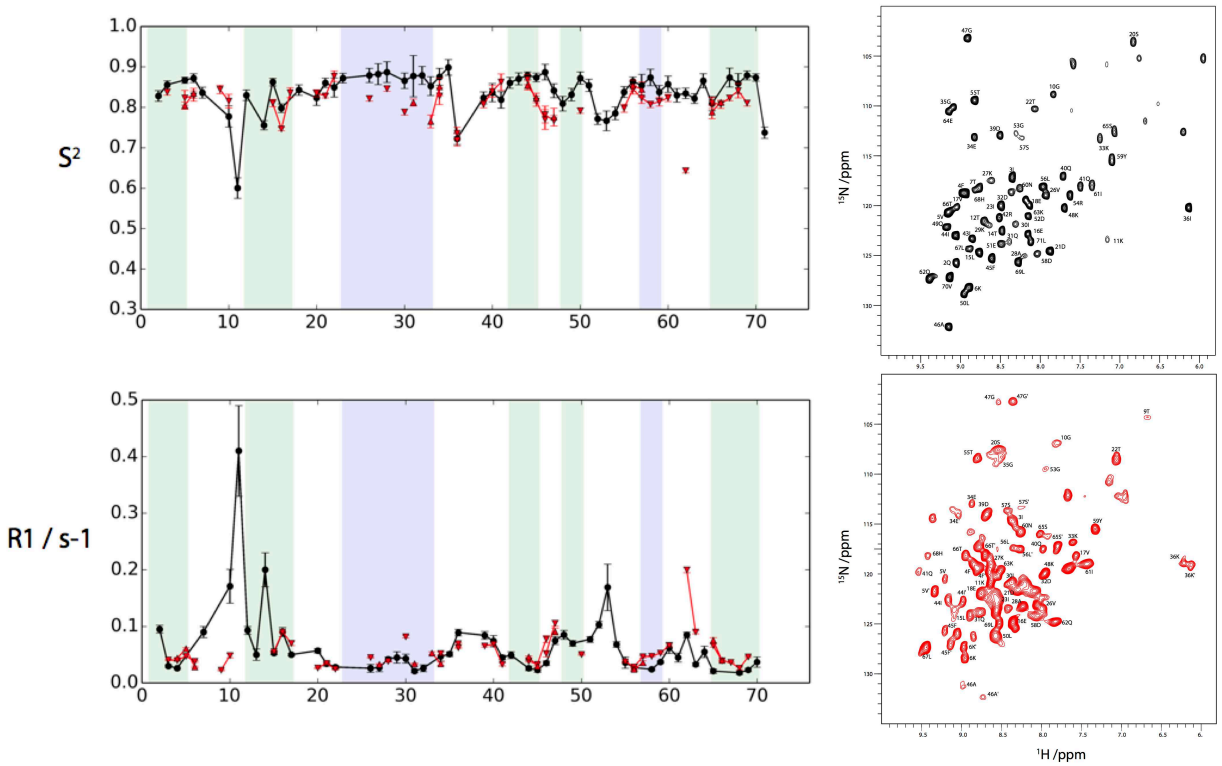

Figure 32. Investigation of dynamics in two different ubiquitin polymorphs. Shown in black are the MPD crystals used in the sections above as well as in all other chapters of this work. Shown in red are data obtained on ubiquitin crystals obtained with PEG and zinc acetate as precipitants. Shown are squared order parameters, ^{15}N R_1 rates and the corresponding ^{1}H-^{15}N correlation spectra.

We have analyzed in detail the protocol to determined one-bond dipolar couplings in deuterated proteins, placing particular emphasis on eliminating possible sources of systematic errors. From our investigations it has become clear that rf mis-settings and inhomogeneities may introduce systematic errors of a few percent, which is a substantial error when seen on the scale of the motional amplitude, $1\text{-}S^2$. The REDOR experiment has a significant advantage over other recoupling schemes, namely its reliance on a train of well-separated π pulses. Calibrating such pulses is more straightforward than calibrating rf fields for continuous-irradiation based approaches, such as TMREV [47,48], R18 sequences [41,49], phase-inverted CP [43,52]. Furthermore, phase transients and instability of the rf fields impact these sequences more than the REDOR sequence. The only limitation of the REDOR experiment is its requirement for rather well isolated spin pairs, such as 1H-15N in deuterated proteins [56]. Our new data, obtained with accurate pulse calibration and consideration of the rf inhomogeneity, also point to systematic offset of a previously published data set, but reveal that the profile of S^2 values over the sequence is highly reproducible.

We have shown that it is crucial to have such dipole-coupling data for fitting backbone dynamics. Using relaxation data alone generally leads to systematic bias of order parameters, i.e. an overestimation of S^2. Furthermore, fitting R_1 and $R_{1\rho}$ or CCR data will essentially always lead to fits that indicate nanosecond motion, even if there is no such motion present. This has been shown by simulations (Figure 24) and experimental data (Figure 27). In this sense, the detection of nanosecond motion, that has been claimed in recent studies [44,60,66], are likely to be artifactual, just as the nanosecond motion that is detected in fits shown here, using only relaxation data, are artefacts..

We show that measurements at a single magnetic field strength are sufficient if only the SMF approach is used.

The findings and protocols that are shown here for ^{15}N sites along the backbone likely also apply to other sites, that have so far received less attention, such as methyl side chains [40,67], or backbone carbon sites [31]. We foresee that for these sites it will be equally important to complement relaxation data with dipolar coupling measurements. Given appropriate labeling, such as recently proposed selective methyl labeling [40,67] or random sparse protonation [68], the findings reported here for ^{15}N amide sites can readily be applied to other backbone and side chain sites. Such studies will allow to provide a comprehensive picture of protein motion, including proteins that are inaccessible to other techniques, such as insoluble or very large protein assemblies.

5 Site-resolved measurement of microsecond to millisecond conformational-exchange processes in proteins by solid-state NMR spectroscopy[#]

5.1 Introduction

Functional processes in proteins, such as enzymatic catalysis, ligand binding or allosteric signal transmission rely on the ability of proteins to sample multiple conformational states, differing in structure and free energy. There is increasing evidence that the actual functional states of proteins are in many cases higher-energy conformers in dynamic equilibrium with the major, lowest-energy conformer, rather than the lowest-energy state itself.[7,9,23,69] In many cases, the exchange processes between these different functional states occur on a microsecond to millisecond (μs-ms) time scale, which also coincides with typical time scales of enzyme catalysis and protein folding. Therefore, the accurate characterization of dynamic processes on this time scale, and the identification and structural characterization of higher-energy conformations in equilibrium as well as the relative populations and exchange kinetics, is of primary importance for understanding protein function. Due to their low population and short life times, detecting and characterizing such higher-energy conformers is a major experimental challenge.
NMR spectroscopy in solution state is playing a prominent role in studies of conformational exchange processes and is able to provide information at atomic resolution.[70] In NMR, the presence of low-populated conformational states, exchanging with the major conformation on μs-ms time-scales, is manifest as enhanced decay of single- or multiple-quantum coherences. Thus, a first indication about conformational exchange processes may be obtained from inspection of transverse relaxation rates (e.g. R_2 rate constants of ^{15}N). Higher-than-average values of R_2 may indicate the presence of exchange processes. In solution NMR, a variety of more quantitative and direct techniques have been developed to probe conformational exchange processes with great detail and accuracy.[70,71] The most prominent ones of those are Carr-Purcell-Meiboom-Gill (CPMG) relaxation-dispersion (RD)[71,72] and $R_{1\rho}$ relaxation-dispersion[73] techniques and the analysis of differential relaxation of multiple-quantum coherences[74-76] These methods allow the determination of thermodynamic and kinetic parameters in terms of relative populations and exchange-rate constants, as well as site-specific chemical-shift differences between the major, observable state and the higher-energy conformation. Structural information about these minor, not directly observable states can thus be obtained.

Studies of protein dynamics in the solid state have recently attracted great interest,[48,61,77-81] motivated by numerous important biophysical questions related to insoluble proteins, such as the dynamics and gating of membrane proteins in native membranes or the conformational flexibility in fibrils. Magic-angle spinning (MAS) solid-state NMR methods that probe either fast (sub-microsecond) motions, or slow (ms-to-seconds) dynamics in an atom-resolved manner are available,[82-84] but so far a quantitative investigation of processes occurring on the μs-ms time scale has remained a major challenge.
In this chapter, I present approaches for the detection and quantitative measurement of μs-ms conformational exchange processes by MAS solid-state NMR, that exploit the effect that conformational exchange processes have on single- and multiple-quantum line widths. We demonstrate two independent approaches, namely the measurement of differential line broadening of zero- and double-quantum coherences, and CPMG relaxation dispersion. Both approaches rely on *differences* between line widths (or, equivalently, life times), to extract information about

[#] This work was published in Tollinger, M.; Sivertsen, A. C.; Meier, B. H.; Ernst, M.; Schanda, P. *J Am Chem Soc* **2012**, *134*, 14800.

conformational exchange, rather than on the line widths themselves. This is crucial, as solid state NMR line widths typically contain contributions from coherent mechanisms (e.g. dipolar dephasing).[20] We find that under suitably chosen experimental conditions, these differences in line widths are only weakly dependent of coherent dephasing mechanisms, allowing thus - to a good approximation - the quantitative analysis of the experimental data in terms of conformational exchange (vide infra).

In order for our approaches to be successful, it must be ensured that the life times of the involved single- and multiple-quantum coherences are sufficiently long, such that the differences can be measured with the needed precision. For example, CPMG RD experiments, such as used in solution state, typically use delays of tens of milliseconds during which the coherence decay is monitored in the presence of a train of refocusing pulses. In a typical solid protein sample undergoing MAS at moderate frequency, coherence life times are generally only a few milliseconds at most, without high-power proton decoupling, and CPMG approaches are, therefore, not readily applicable. High-power ^{1}H decoupling can extend these life times to 10-20ms, although at the cost of sample heating, which impedes quantitative dynamical analysis. We circumvent these limitations by using highly deuterated protein samples and high magic-angle spinning frequencies. As reported earlier by several groups, ^{15}N single-quantum life times in such conditions become very long, often exceeding 100-200ms.[32,34,85] As we find here, even heteronuclear multiple-quantum ^{1}H-^{15}N coherences have life times of tens of milliseconds under such conditions. These long life times open the way to use transverse relaxation parameters for quantitative measurement of conformational exchange. We make use of this potential, and obtain insight into conformational exchange processes in microcrystalline ubiquitin. We find evidence for a conformational exchange process involving residues that also undergo exchange in solution, but at a rate that is more than one order of magnitude slower than in solution.

5.2 Results and Discussion

5.2.1 Differential zero- and double-quantum ^{1}H-^{15}N line broadening reveals conformational exchange.

As a first approach for the study of conformational exchange in solid protein samples, we investigate the differential rate of dephasing of ^{1}H-^{15}N multiple-quantum coherences (MQC). Differential line broadening of zero- and double-quantum coherences (ZQC/DQC) is expected whenever the isotropic and/or anisotropic components of the chemical shifts of the two involved nuclei undergo simultaneous fluctuations.[74,86] This effect has been exploited in solution state to probe conformational exchange,[75,87,88] and is often referred to as differential zero- and double-quantum relaxation. (Although when considering µs-ms processes, it is not a relaxation phenomenon in the sense of Redfield theory.[17] In this paper, we will preferentially use the terms "differential line width" or "differential decay" instead of "differential relaxation".) Here, we explore the feasibility of exploiting these effects in the solid state, by studying correlated chemical-shift modulation in amide ^{1}H-^{15}N spin pairs.

We first analyze the properties of differential zero- and double-quantum coherence decay in the solid state by numerical spin simulations. To this end we consider the simplest possible model, a two-spin ^{1}H-^{15}N system undergoing stochastic jumps between two distinct conformations differing in the orientation of the bond vector and CSA tensor orientations and/or in the isotropic chemical shifts of the two nuclei. Figure 33 shows representative results of such simulations for a system undergoing exchange between a major (90%) and a minor (10%) conformation. Shown is the differential ZQC/DQC decay rate, $\Delta R_{MQ}=R_{DQ}-R_{ZQ}$, for various exchange-rate constants. In order to identify the origin of the differential decay, separate simulations were performed for (i) a scenario where minor and major state have different isotropic chemical shifts but identical chemical-shift anisotropy (CSA) tensors (blue), and (ii) a situation where the two states have identical isotropic shifts, but the two CSA tensors undergo orientational fluctuations (green). Modulation of the

isotropic shifts only (scenario i), leads to differential MQC decay rates if exchange occurs on a time scale of microseconds to a few milliseconds, slightly depending on the exchange parameters and chemical-shift differences. This is identical to solution-state NMR[74,86,89] and the simulations can be fully described by a formalism derived previously.[89] Fluctuations of the magnitude and/or the orientations of the two CSA tensors (scenario ii) also induce differential decay, which can be understood as an interference between MAS and these CSA fluctuations. The origin of such fluctuations may be an exchange process between a major and a minor conformation, as shown in Figure 33 or bond librations within a continuum of conformers, such as restricted orientational diffusion. Irrespective of the precise motional model, such CSA/CSA modulations will lead to strong differential MQ decay whenever they occur on a time scale of tens of nanoseconds to about one millisecond. Finally, we note that via either of the two mechanisms (CSM/CSM or CSA/CSA), the ΔR_{MQ} can be positive or negative, depending on the sign of the isotropic chemical-shift changes of the two nuclei, and the CSA parameters. Taken together, these simulations indicate that the differential multiple-quantum line broadening in the solid state is a sensitive reporter of conformational-exchange processes on time scales in the range of tens-of-nanoseconds to milliseconds.

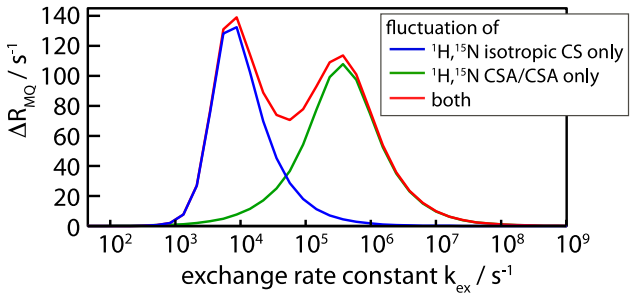

Figure 33. Numerical simulations of the differential decay rates of zero- and double-quantum coherences (differential multiple-quantum decay rate), $\Delta R_{MQ}=R_{DQ}-R_{ZQ}$, in a ^{1}H-^{15}N spin pair undergoing exchange. A two-site exchange system involving a major state (populated at 90%) and a minor state (10%) was assumed, with an exchange rate $k_{ex}=k_{AB}+k_{BA}$, where k_{AB} denotes the forward rate constant. ΔR_{MQ} is shown as a function of the exchange-rate constant. The different simulations assume either only isotropic chemical-shift modulation ($\Delta\nu_N$=160Hz, $\Delta\nu_H$=800Hz), only CSA/CSA modulations (jumps by 30°) or both, as indicated in the insert. Details about the simulation parameters and additional simulations are provided in the Supporting Information.

To test the practical usefulness of differential MQC decay for dynamics studies in the solid state, we have applied the experiment shown in Figure 34a to u-[^{2}H,^{15}N]-labeled microcrystalline ubiquitin, reprotonated stochastically at 20% of the exchangeable sites, undergoing MAS at a frequency of 50kHz, at a sample temperature of 300K. In the pulse sequence of Figure 34, an initial state $2H_xN_x$ (a combination of ZQ and DQ coherences) is prepared utilizing the scalar coupling. Such a J-coupling transfer is enabled by the long coherence life times of ^{1}H and ^{15}N.[34] During the subsequent MQC evolution delay, the operator $2H_yN_y$ builds up from the initial $2H_xN_x$ whenever ZQC and DQC decay differently. From two separate experiments, probing the $2H_xN_x$ and $2H_yN_y$ operators, respectively, one can quantify the differential decay rate $\Delta R_{MQ} = R_{DQ}-R_{ZQ}$. For this experiment to be successful, it is necessary that the MQC are sufficiently long-lived, such that the buildup can be followed. Under the conditions employed in this study, we were able to follow the ^{1}H,^{15}N MQC decay over tens of milliseconds.

Figure 34b shows experimental buildup curves of the state $2H_yN_y$ from $2H_xN_x$ for a set of representative residues. Fits of the differential decay-rate constant ΔR_{MQ} to these curves are indicated as solid lines, and residue-wise values of ΔR_{MQ} are shown in Figure 34c. Most strikingly, large ΔR_{MQ} values are observed for residues I23, K27 and T55, with respective values of ΔR_{MQ}=179±47, 53±16 and 172±44 s^{-1}, greatly exceeding average values for the other residues (average value of -1.4 s^{-1}, standard deviation 12.3s^{-1}). Figure 2d shows the location of these residues in the structure of ubiquitin.

The large values of ΔR_{MQ} reveal fluctuations of the isotropic and/or anisotropic components of the chemical shifts of the $^1H/^{15}N$ nuclei of residues I23, K27 and T55. As shown above, the two mechanisms (CSA/CSA, CSM/CSM) are sensitive to different time scales of motion. From the present data alone it is not possible to determine whether the underlying process involves CSA/CSA fluctuations, (tens of nanoseconds to tens of microseconds time scale), or if it arises from fluctuations of the isotropic chemical shifts (tens of microseconds to a few milliseconds). However, several arguments indicate that isotropic chemical-shift modulations on a µs-ms time scale are at the origin of the differential decay. The most important experimental evidence comes from our recently reported ^{15}N-^1H dipole/^{15}N CSA cross-correlated relaxation measurements.[16] This cross-correlated relaxation rate is sensitive to motion occurring on the same time scale for which CSA/CSA fluctuations induces differential MQC decay.[90] Notably, residues I23, K27 and T55 did *not* show elevated ^{15}N-^1H dipole/^{15}N CSA cross-correlated relaxation-rate constants, showing that these residues do not undergo large-scale nanosecond-to-microsecond motion.[16] This finding rules out the possibility that CSA/CSA fluctuations are the main reason for the observed the differential MQC decay. As a further indication for isotropic chemical-shift modulations, the neighboring residues E24 and N25 are invisible in proton-detected scalar-coupling-based NMR spectra,[16] presumably as a consequence of short coherence decay times. Thus, the pronounced differential MQC decay found here for the three residues strongly suggest the presence of a conformational exchange process involving fluctuations of isotropic chemical shifts occurring on a time scale of tens of microseconds to a few milliseconds. CPMG relaxation dispersion data below confirm this analysis. In principle, it would be possible to discriminate between isotropic and anisotropic chemical-shift fluctuations as the cause the of the large differential decay-rate constants by performing the experiment at a different MAS frequency, which alters the position of the maximum of the CSA/CSA contribution, or through rf irradiation during the MQC evolution.[91,92]

Figure 34c shows that some variation in ΔR_{MQ} values is also found for other residues in ubiquitin. We ascribe these residue-wise differences to local variations of motional amplitudes, causing enhanced ΔR_{MQ} via the CSA/CSA mechanism; for example, larger than average $|\Delta R_{MQ}|$ are observed in the loop comprising Gly10 and Lys11, for which we have previously reported extended mobility on a time scale of hundreds of nanoseconds[16] (see also section 4). The relatively large ΔR_{MQ} for L43 is not statistically significant; indeed, CPMG experiments do not show any conformational exchange for this residue (see below).

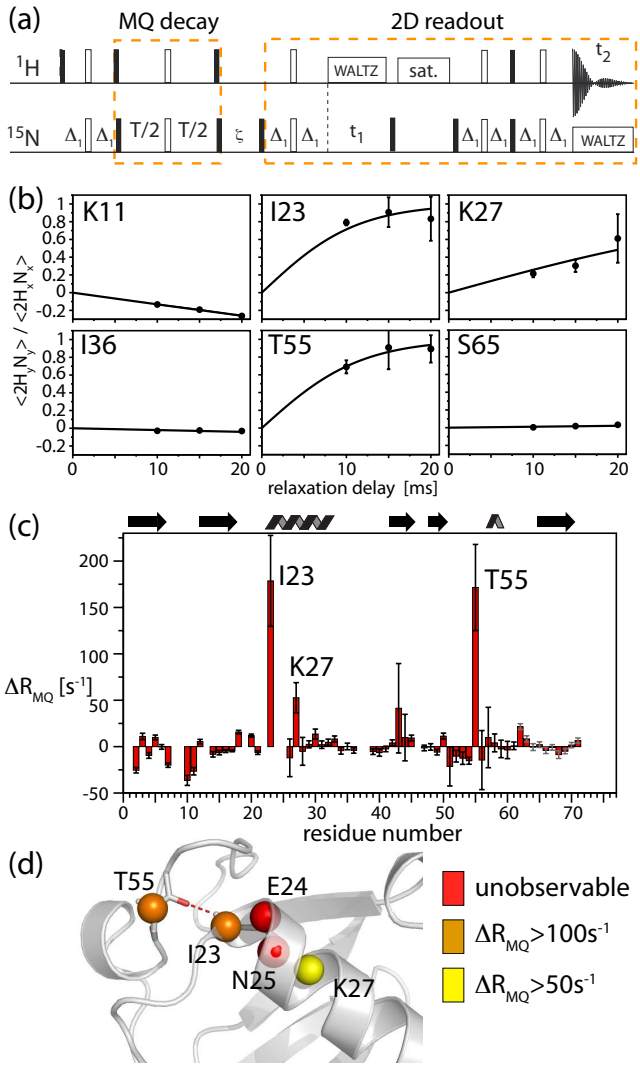

Figure 34. Measurement of differential multiple-quantum decay rates. (a) Pulse sequence used in this study. Differential zero- and double-quantum line broadening is obtained from separate experiments that probe the coherences, $2H_xN_x$ and $2H_yN_y$, respectively, which are selected by setting the phases of the pulses at the end of the MQC evolution delay.[74] (b,c) Experimental data obtained on a microcrystalline sample of ubiquitin at 300K. (b) Representative examples of the buildup of $2H_yN_y$ from $2H_xN_x$, along with best-fit curves, $\Delta R_{MQ} = (2\ \mathrm{atanh}(\langle 2H_yN_y\rangle / \langle 2H_xN_x\rangle))/T$. Error bars were obtained from two times the standard deviation of the spectral noise. (c) Fitted residue-wise differential multiple-quantum decay-rate constants ΔR_{MQ} , using three different relaxation delays. Error margins were determined from Monte Carlo simulation based on error bars determined from twice the spectral noise. Residues with particularly large ΔR_{MQ} are indicated. Note that, in principle, a single relaxation delay would suffice to determine ΔR_{MQ}. (d) Residues for which large ΔR_{MQ} are observed (I23, K27, T55) as well as unobservable resonances (E24, N25) in ^{1}H-detected HSQC-type spectra[16] are plotted onto the structure. The H-bonding of I23(HN)-R54(CO) is indicated.

5.2.2 ^{15}N CPMG relaxation dispersion experiments.

In order to obtain more quantitative insight into the exchange process revealed by the above MQC decay data, we explored single quantum ^{15}N CPMG relaxation dispersion as a second experimental strategy to probe conformational dynamics in the solid state. CPMG relaxation dispersion experiments measure the ^{15}N coherence decay as a function of the repetition rates of CPMG refocusing pulses, ν_{CPMG}. In order to be quantitatively accurate, it must be ensured that all coherence decay mechanisms that are not due to isotropic chemical-shift fluctuations do not depend on the CPMG frequency (any CPMG frequency-independent contribution to decay rates, however, would not hinder quantitative accuracy). These mechanisms are (i) Redfield relaxation (in solution and in the solid state), and (ii) coherent mechanisms leading to a decay, in particularly dipolar dephasing in the solid state. In order to ensure that the former (Redfield relaxation) is independent of the CPMG frequency, two approaches have been proposed in solution state: a relaxation-compensated scheme on the one hand,[93] that ensures that in-phase coherence (N_x) and anti-phase coherence ($2H_zN_y$) evolve for the same amount of time irrespective of ν_{CPMG}, as well as an approach that only measures the decay of in-phase coherence, by suppressing the buildup of anti-phase coherence through ^{1}H decoupling.[94] For reasons of decoupling efficiency, in the latter approach the ^{1}H decoupling field is slightly varied between different CPMG frequencies.[94] In the solid state, this latter approach is complicated by the fact that varying the ^{1}H decoupling field strength induces artifacts related to partial interference between MAS and ^{1}H irradiation, which can lead to a partial reintroduction of dipolar couplings. Therefore we opted here for the former approach, a constant-time[95] relaxation-compensated[93] scheme. This experiment measures the effective rate of ^{15}N coherence decay, R_{2eff}, as a function of the CPMG pulsing rate (see Figure 35a), by using a single constant time delay without ^{1}H decoupling. Long ^{15}N SQ coherence life times even without ^{1}H decoupling[34] under fast MAS conditions enable this experiment.

In addition to ensuring that the Redfield relaxation part is independent of ν_{CPMG}, it must also be ensured that the decay induced via coherent mechanisms (dipolar dephasing) is independent of the CPMG frequency. We have investigated this issue experimentally and through numerical simulations, as follows. Representative experimental CPMG dispersions, i.e., the effective transverse decay rate, R_{2eff}, as a function of the pulse repetition rate ν_{CPMG}, are shown in Figure 35b, measured at two different B_0 field strengths (14.1T, 18.8T). Measurements at several B_0 field strengths are valuable as the isotropic chemical shift changes upon exchange (in Hertz) depend on the magnetic field, and thus dispersion profiles change with B_0.[96] Large dispersions, i.e. a pronounced dependence of R_{2eff} on ν_{CPMG}, are observed for residues I23, K27 and T55 – the same residues for which large ΔR_{MQ} values also pointed to conformational exchange of these residues. However, the overwhelming majority of residues display flat CPMG dispersion curves, as exemplified in Figure 35b (K11, I36, S65). The observation of such flat CPMG curves indicates that the ν_{CPMG}-dependent variations of decay due to coherent mechanisms are small, a consequence of the strong reduction of the dipolar coupling network in our sample. In order to obtain a more detailed understanding of the properties of CPMG experiments in a rotating solid sample undergoing exchange, as required for any quantitative interpretation, we then turned to numerical spin simulations. These simulations, reveal that in the general case, CPMG dispersion profiles in a rotating solid are more complex than in solution. Interference effects between time-dependent fluctuations of anisotropic interactions (dipolar couplings, CSA), MAS rotation and the CPMG pulses may arise. These interferences generally lead to increased decay rates R_{2eff}. These increased decay rates are only slightly dependent on the CPMG frequency (a ν_{CPMG}-independent shift of dispersion profiles would be irrelevant for data analysis). Variations of R_{2eff} with ν_{CPMG} that are not due to isotropic chemical-shift fluctuation are estimated to be below about $5s^{-1}$. This is within the error bar of our experiments. We therefore conclude from experimentally observed flat CPMG curves and from simulations, that the possible systematic errors in the CPMG curves – which might prohibit quantitative interpretation of such curves in terms of dynamics – are below our

experimentally observed error bars. The large dispersions observed for I23, K27 and T55 are clearly dominated by isotropic chemical shift fluctuations.

We therefore applied the Bloch-McConnell formalism, which is strictly valid in solution-state, but which neglects any effects specific to solid-state NMR, to interpret the dispersion profiles found for residues I23, K27 and T55. A common exchange event for the three residues was modeled, with a population of the minor state, p_B, and exchange rate constant $k_{ex}=k_{AB}+k_{BA}$ (where k_{AB} and k_{BA} denote forward and backward rate constants), along with individual residue-specific chemical-shift differences between major- and minor-state, $\Delta\omega_{AB}$. Solid lines in Figure 3b show the best-fit curves for such a fit. The data can be explained by a higher-energy conformation populated to p_B=10.0% (±3.2%), and an exchange rate k_{ex} of 2100 s^{-1} (±700s^{-1}). The chemical-shift differences, $|\Delta\omega_{AB}|$, for Ile23, Lys27 and Thr55 were obtained as 3.8ppm (±1.2ppm), 1.5ppm (±0.6ppm) and 2.0ppm (±0.7 ppm), respectively. We note that fitting the residues individually results in identical populations and rate constants (within error margins) as a joint fit, although at lower precision.
We also reassured that the use of the simplistic Bloch-McConnell treatment, i.e. the neglect of the effect of coherent mechanisms, does not introduce large systematic errors. To this end, we simulated a larger (4-spin) system undergoing exchange with the above parameters, as well as MAS and fluctuations of anisotropic interactions. The exchange parameters resulting from a Bloch-McConnell fit to these simulations shows that the systematic errors in the fitted values of p_B, k_{ex} and $|\Delta\omega_{AB}|$ are below their respective random error levels given above (data not shown here).
The extracted exchange parameters for I23, K27 and T55 can be used to estimate the differential decay experimental data: the proton chemical shift difference required to reproduce the experimental ΔR_{MQ}, based on these exchange parameters, are of the order of 0.5ppm.
Finally, we note that the plateau levels of R_{2eff} vary substantially among the non-exchanging residues. For example, while for Ile36 and Ser65 we find values of R_{2eff} in the range of 10-20s^{-1}, Lys11, which also displays a flat dispersion curve, has much faster transverse decay (about 50-70s^{-1}). The absolute values of these plateaus cannot rigorously be interpreted in terms of motion, as these plateau levels contain contributions from coherent dephasing mechanisms. However, the variability in these values between different residues points to previously identified large amplitude motions on nanosecond time scales in this region of the protein (loop spanning residues 8-11), that increases the transverse relaxation-rate constants.[16]

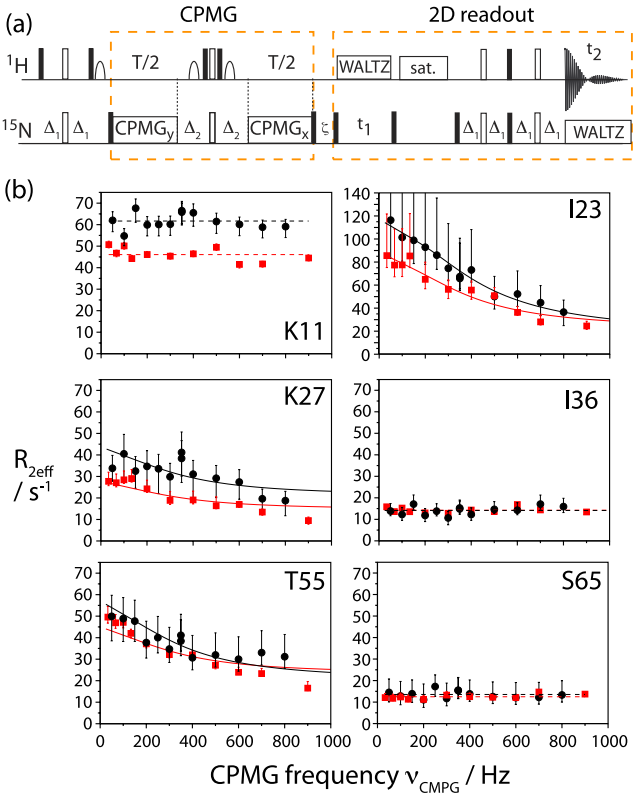

Figure 35. (a) Pulse sequence used in this study to measure ^{15}N CPMG relaxation-dispersion data on deuterated proteins in the solid state. Details are shown in the Supporting Information. (b) ^{15}N CPMG relaxation-dispersion solid-state NMR data obtained on microcrystalline ubiquitin at 300 K sample temperature, collected at a ^{1}H Larmor frequency of 600 MHz (red) and 800 MHz (black). Note the different scale in the data of Ile23. Upper and lower error bars of R_{2eff} were determined from Monte Carlo simulations, based on twice the spectral noise (see Supporting Figure S17). For residues I23, K27 and T55, solid lines represent the Bloch-McConnell fit, in other cases lines represent the mean values of the individual data points. Data for all other residues are shown in the Supporting Information of reference [97].

5.2.3 Comparison to conformational exchange in solution.

The above data reveal a conformational exchange process in microcrystalline ubiquitin in which the N-terminal part of the α-helix and the adjacent loop (Figure 2d) are in exchange with a minor conformation populated to 10%. At 300K this process occurs at a rate of about 1400 to 2800 s^{-1}. It is interesting to compare our findings to data obtained in solution. Comparative studies of dynamics in solution and in crystals have been reported recently for the case of sub-microsecond motion,[40,61,67,98] and we can perform such a comparison here for the first time for µs-ms motion.
Conformational exchange processes in ubiquitin have been addressed in a number of solution-state NMR studies.[65,75,88,99-102] Two regions have been found to undergo exchange, (i) the region comprising residues I23-N25 and T55, i.e. the N-terminal part of the α-helix and the adjacent loop, and (ii) residue V70; these processes are thought to be independent.[65,103] The exchange process involving V70 is fast in solution, and could initially only be detected with $T_{1\rho}$ measurements at low temperatures, including supercooled water,[65,102], and later with experiments that selectively probe µs motion.[100] Even at low temperatures (260-278K), the exchange process involving V70 occurs at a time scale of about 100µs.[65,102] Such fast motions would not induce CPMG dispersions of significant amplitude, and may thus escape from detection in our CPMG experiment, particularly as our experiments were performed at higher temperature (300K), where the process is expected to be even faster. An exchange process on a time scale of tens of microseconds should, however, induce

differential MQC decay via the CSA/CSA mechanism, which we do not observe. This suggests possible differences in the motion of V70 between solution and microcrystals.

Interestingly, the other region for which conformational exchange is present in solution, i.e. the N-terminal part of the helix and adjacent loop, corresponds exactly to the region for which our experiments reveal conformational exchange. However, the rate constant of this process is clearly different. In solution, the conformational exchange process occurs at a rate of about $12500s^{-1}$ to $25000s^{-1}$,[65,75,101] at temperatures of 277-280K, i.e. ~20K lower than the temperature used here (300K). At 298K, the process is essentially undetectable by $T_{1\rho}$ measurements in solution, presumably because it is too fast (several tens of thousand per second). The population of the higher-energy conformation could not be obtained from solution-state measurements, as populations and chemical-shift differences cannot be disentangled in the fast exchange regime from $T_{1\rho}$ measurements. Our data show that in the crystalline state the motional rate constant is more than one order of magnitude slower than in solution. We also investigated whether differences in the solvent conditions, such as pH or viscosity may explain such a large slowdown of the motion. However, solution-state CPMG and differential MQC decay data in solvent conditions very similar to the crystallization conditions, including up to 45% (v/v) precipitant, do not show any detectable exchange (data not shown here). Thus, we conclude that it is indeed the crystalline environment that causes the slowdown of the exchange process.

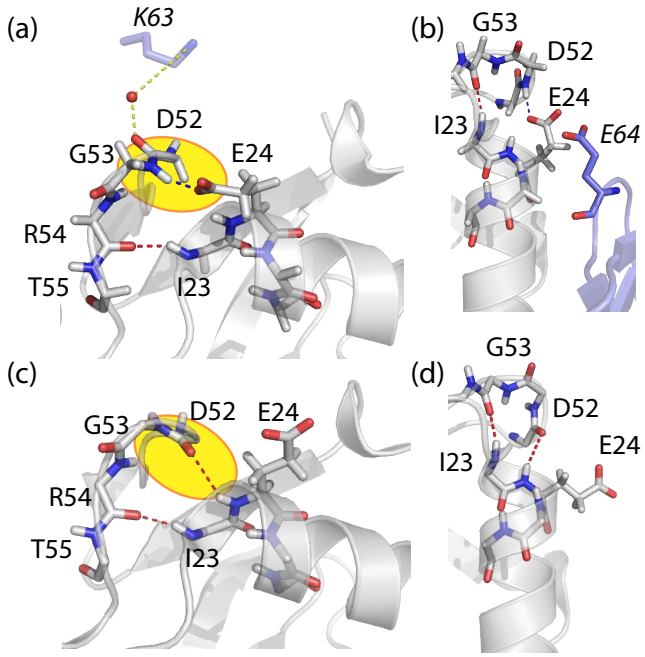

Figure 36. Structural comparison of the microcrystals used in this study, pdb 3ons[104] (a, b) and a solution structure of ubiquitin, pdb 1d3z[105] (c, d). Intramolecular H-bonding among backbone atoms and H-bonds involving side chains are indicated in red and blue. Water-mediated intermolecular H-bonds are shown in yellow. Neighboring molecules in the crystal lattice are shown in light blue in (a) and (b), highlighting residues *K63* and *E64* of the neighboring molecules. Note the different conformation of the loop E51-R54 in the two structures (a,b) and (c,d), resulting in a flip of the orientation of NH(G53) and CO(D52).

It is interesting to speculate about the origin of the different exchange rates in solution and microcrystals. In solution state, a mechanistic picture of the observed conformational exchange process has been proposed recently, primarily from mutation studies[103] and analyses of chemical shifts,[101] as well as from inspection of conformational heterogeneity in various solution and X-ray structures. The conformational heterogeneity is illustrated in Figure 36, showing ubiquitin's structure in the microcrystals used in this study (a, b), and in solution (c, d). Most importantly, these structures differ in the conformation of the loop D52 to T55. In microcrystals (panels a, b) this loop adopts a type II β-turn conformation, with a H-bond between E24 (side chain) and G53 (NH). The available solution structure, as well as other crystal structures (e.g. 1ubi), show a type I β-turn conformation and a H-bond between D52 (NH) and E24 (CO), i.e. the two structures differ by a flip of the peptide plane D52-G53. The exchange process as detected by solution NMR is thought to correspond to an exchange between the type I and the type II β-turn, as well as to the breaking of the H-bond of I23(NH)-R54(CO) and side chain reorganization.[75,101,103]
The structural differences between the major conformational states in solution (type I β-turn) and in microcrystals (type II β-turn) provide one explanation for the different exchange rate constants: it appears that the relative energy of the lowest-energy state and higher-energy states are reversed in solution and microcrystals. In addition, a number of intermolecular contacts could also contribute to a slowdown of the motion in microcrystals. Particularly, in microcrystals the backbone carbonyl of D52 is H-bonded via a water molecule to a lysine of a neighbor molecule (Figure 4a), and the conformation of E24's side chain is stabilized by an intermolecular contact to E64 of another molecule (Figure 36b), thus stabilizing the type II β-turn conformation. An exchange process involving a flip of the backbone of D52/G53, would require that all these interactions be broken. The free-energy barrier that needs to be overcome for breaking these interactions in microcrystals would certainly slow down the exchange process.

5.3 Conclusions

In summary, we have provided the first direct quantitative analysis of the µs-ms dynamics of a protein in the solid state, using two independent approaches based on transverse coherence decay. To the best of our knowledge, transverse decay parameters have not been used in a quantitative manner as measures of µs-ms conformational exchange in solid-state NMR. The advent of deuteration and fast MAS is changing this situation, thus providing new possibilities for studying dynamics quantitatively.

The measurement of the differential MQC decay explored here allows identifying the regions undergoing slow motional processes. In contrast to solution-state experiments, both isotropic and anisotropic chemical-shift fluctuations contribute to the differential MQC decay and report on events on long time scales (hundreds of nanoseconds to milliseconds). We foresee that similar approaches will be useful for spin pairs other than ^{1}H,^{15}N, e.g. ^{13}C,^{15}N or ^{13}C,^{13}C pairs. From a suite of such experiments using different nuclei, a comprehensive picture of the exchange process may be obtained. Moreover, in the solid state MQC may be established even for spins remote in sequence, and the differential decay of these coherences may provide insight into correlated motions over longer distances. Recent reports of proton-proton double-quantum transfer over up to 10Å may be one possible route in this direction.[37,38] At this point, we did not attempt a quantitative analysis of differential MQC decay in terms of exchange parameters. Such an analysis is complicated by the fact that a single experimental observable, i.e. the differential line broadening, is sensitive to a number of parameters, including chemical-shift parameters for two nuclei and exchange rates. As shown here, CPMG RD experiments can provide such quantitative information about conformational exchange processes. When combined with advanced deuteration and back-protonation schemes, similar approaches as used here for ^{15}N may become applicable also to other backbone and side chain moieties. For example, using sparse random protonation[68] or methyl-selective labeling[40,67] very long ^{13}C coherence life times are achieved, which enable CPMG experiments, opening possibilities towards a detailed characterization of higher-energy conformations in proteins in the solid state. Deuteration and fast MAS will also enable the measurement of other probes of conformational exchange, such as $T_{1\rho}$ relaxation dispersions, and may also be interpretable in terms of quantitative exchange parameters. Progress in this direction has been reported recently.[20,106]

This study has focused on a microcrystalline protein. We find the conformational exchange process to be altered by the crystalline environment, relative to free solution. This direct demonstration of the impact of the environment on dynamics is of physico-chemical interest, and it also indicates that one must be careful in interpreting data from crystalline preparation in terms of biological relevance in solution state. Importantly, the proposed experiments open new avenues for the study of more complex molecules, for which the solid-state is the biologically relevant preparation, such as membrane proteins and amyloid fibrils. It has been shown recently that proton-detected experiments, akin to the approaches used here, can also be applied to highly-deuterated samples of membrane proteins or amyloid fibrils.[27,28] Long heteronuclear coherence life times in such samples are expected to enable similar experiments as shown here. Further improvements in experimental design in terms of more efficient coherence transfers (CP instead of INEPT), proton decoupling and optimized levels of protonation may be envisaged to improve sensitivity, which will be particularly useful for such challenging samples. We foresee that studies of µs-ms motion will be instrumental for understanding complex biomolecular processes, such as allosteric binding and gating of membrane proteins.

6 Structural Insight into Transient Conformational States of Proteins by Solid-State $R_{1\rho}$ Relaxation-Dispersion NMR Spectroscopy[#]

6.1 Introduction

The function of proteins depends on their ability to sample a variety of states differing in structure and free energy. Deciphering how the various thermally accessible conformations are connected, and understanding their structures and relative energies is crucial to rationalize protein function. Many biomolecular reactions take place within microseconds to milliseconds (μs-ms), and this time scale is therefore of central functional importance. Solution-state NMR spectroscopic techniques, and in particular so-called relaxation-dispersion (RD) NMR approaches, have proven very successful for studying μs-ms motion and characterizing the exchanging short-lived conformations.[73,107] RD NMR techniques exploit the effect of conformational exchange processes on line broadening, i.e. on the relaxation rates of nuclear spin coherence (R_2, $R_{1\rho}$). By quantifying spin relaxation rates in the presence of a variable radiofrequency (rf) field, RD approaches provide information about relative populations and exchange rates, as well as chemical shifts of short-lived conformational states, and thus about local structure.[21,73,107-109] In the cases of very large assemblies or insoluble aggregates, where solution-state NMR is severely challenged, magic-angle spinning solid-state NMR (MAS ssNMR) is rapidly emerging as a tool for the study of structure and dynamics. However, the characterization of μs-ms conformational exchange dynamics in the solid state remains challenging. Herein, we show a ssNMR approach in which amide-^{15}N $R_{1\rho}$ RD data, i.e. the rate of coherence decay under ^{15}N spin-lock fields of variable field strengths, are quantitatively analyzed and interpreted in terms of conformational dynamics, allowing to get insight into short-lived states in terms of chemical shifts and bond vector orientations.

6.2 The properties of $R_{1\rho}$ experiments in MAS solid-state NMR: insight from numerical simulations

Conformational fluctuations between different states expose a given nuclear spin in a protein to different local environments, characterized by different bond geometries. A simple case, exchange between two states, is shown in Figure 37a. As a result of conformational-exchange dynamics, a given spin will experience a fluctuation of its chemical shift (CS), as well as of its bond vector orientations and, thus, dipolar-coupling interactions with neighbouring spins and CS anisotropies (CSA). In solution-state NMR, dipolar-coupling and CSA interactions are averaged to zero by the Brownian molecular tumbling. Consequently, only fluctuations of the isotropic CS are relevant when considering μs-ms dynamics. $R_{1\rho}$ RD experiments in solution state can, thus, only pick up conformational μs-ms dynamics if they involve a change in the isotropic CS. The relevant theory is well established, and the effects of exchange can be described by the Bloch-McConnell equations.[110] In MAS ssNMR, where the stochastic molecular tumbling is absent, anisotropic interactions (dipolar couplings and CSA) are periodically modulated by magic-angle sample spinning (MAS), and are averaged out over a sample rotation period (in the μs range). This averaging leads to the line narrowing required for high-resolution studies. However, when considering molecular dynamics and rf irradiation, as is the case in $R_{1\rho}$ RD experiments, the various

[#] This work was published in Ma, P.; Haller, J. D.; Zajakala, J.; Macek, P.; Sivertsen, A. C.; Willbold, D.; Boisbouvier, J.; Schanda, P. *Angewandte Chemie (International ed in English)* **2014**, *53*, 4312.

time-dependent processes (sample rotation, rf irradiation and conformational exchange) may interfere, leading to different decay processes. Consequently, the situation is more complex than in solution-state NMR.[111-113] Before considering experimental implementations of MAS ssNMR $R_{1\rho}$ RD experiments, we thus investigate the properties of ^{15}N $R_{1\rho}$ decay in an exchanging system undergoing MAS by numerical simulations.

Figure 37b,c shows simulated ^{15}N $R_{1\rho}$ RD profiles for a ^{1}H-^{15}N spin pair that undergoes exchange between two states, populated to 90% and 10%, respectively, and which is subject to MAS and a ^{15}N spin-lock rf field of variable amplitude. We assumed different exchange scenarios that involve either only a fluctuation of the ^{15}N spin's isotropic CS, or a change of the NH bond orientation within the molecular frame of reference, or both. The results of these simulations can be summarized as follows. (i) If exchange takes place between two states that differ only in their isotropic CS, but not in bond orientations, $R_{1\rho}$ RD profiles can be described by the Bloch-McConnell formalism (black curves in panels b/c), as in solution-state NMR.[73] (ii) If bond angle fluctuations are involved upon conformational exchange (thus reorienting the dipolar-coupling and CSA interactions), the situation gets more complex. $R_{1\rho}$ rate constants in this case are overall increased, because the fluctuating anisotropic interactions induce relaxation.[114] Of particular note for the present discussion is the fact that the increase of $R_{1\rho}$ rates is particularly pronounced when the spin-lock field strength (ν_1) approaches the sample rotation frequency (ν_{MAS}), i.e. close to the so-called rotary resonance conditions.[113,115] Importantly, as shown in Figure 37 and Figure 38 and reported previously,[111,112,114] conformational exchange broadens these rotary resonance recoupling conditions, and the $R_{1\rho}$ relaxation rate in the vicinity of the rotary resonance conditions depends on kinetics of the exchange, the relative populations of the involved states and the jump angle between the different conformations. Taken together, these simulations demonstrate that MAS ssNMR $R_{1\rho}$ RD experiments may provide rich information about conformational exchange, and that they may report not only on chemical shift fluctuations between the states (as is the case in solution-state NMR measurements), but also on the bond angles by which a short-lived "excited" state differs from the predominant "ground-state" conformation.

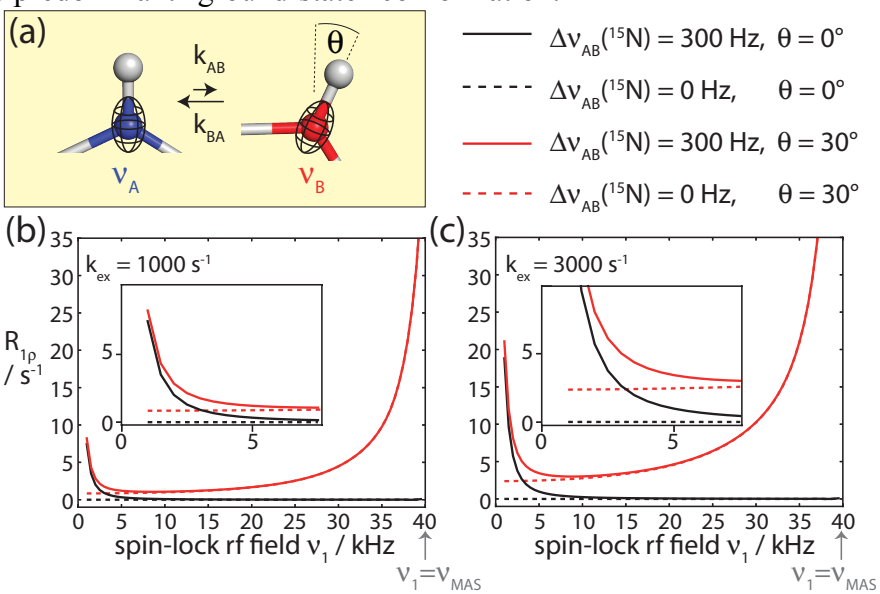

Figure 37. The effect of conformational exchange processes on ^{15}N $R_{1\rho}$ relaxation rates, as revealed by numerical simulations. (a) Schematic representation of a two-spin N-H system that is in dynamic exchange between a minor and a major conformation, differing by the ^{15}N chemical shift and the orientation of the NH bond vector. The ^{15}N CSA tensor is assumed collinear with the NH bond. (b,c) Simulated ^{15}N $R_{1\rho}$ RD profiles obtained for this 2-spin system, assuming relative populations of p_B=10%, p_A=90%. Different scenarios were assumed, regarding the ^{15}N isotropic CS (solid/dotted lines), and the change of the bond angle orientation, θ, occurring during exchange (red/black), as indicated. More simulations are shown in Figure 38. The inserts in (b,c) shows a zoom into the low-rf field regime.

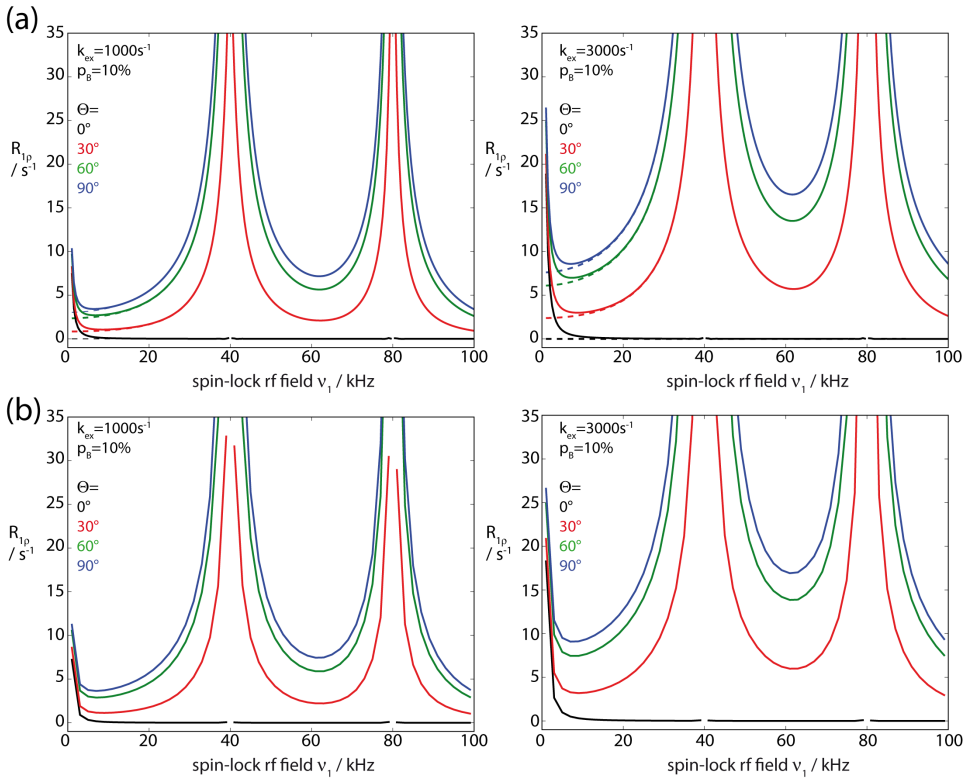

Figure 38. Numerical simulations of R1ρ relaxation dispersion profiles, showing the effect of exchange rates and jump angles. (a) The simulations are similar to the ones shown in Figure 37, with exchange rates, populations and jump angles as shown in the panels. In (b), a three-spin ^{1}H…^{1}H-^{15}N spin system was assumed, where the second ^{1}H spin in the major state is separated from the first ^{1}H spin by 2.5 Å.

6.3 Experimental implementation of $R_{1\rho}$ relaxation dispersion

Exploiting the potential of MAS ssNMR $R_{1\rho}$ RD experiments to quantitatively analyze conformational exchange in proteins – shown by the above simulations – has so far been hampered by the fact that $R_{1\rho}$ decay rates in ssNMR not only contain a dynamics-related component, but also have substantial contributions from coherent decay mechanisms (i.e. dipolar dephasing). Dipolar dephasing contributes to $R_{1\rho}$ decay particularly in multi-spin systems, such as proteins with numerous proton spins. Extracting the dynamics-related part of $R_{1\rho}$ decay rates thus requires suppressing this dipolar-dephasing part. As shown recently, at high MAS frequencies of ~40 kHz or higher, and spin-lock fields above ~15 kHz this dipolar dephasing is significantly reduced and appears negligible even in the proton-rich environment of a protein;[20] however, the requirement for high spin-lock fields eliminates the possibility of observing $R_{1\rho}$ RD in the window below ~5-10 kHz spin-lock field, where RD profiles are particularly sensitive to isotropic CS fluctuations. We circumvent these limitations here by employing high degrees of sample deuteration, which strongly reduces the dipolar-dephasing contribution to ^{15}N $R_{1\rho}$ rates.[25,32,34] In highly deuterated samples, i.e. samples that are fully deuterated at non-exchangeable sites, and in which the exchangeable (amide) sites are (partly) re-protonated, the proton dipolar coupling network is strongly diluted, allowing for high-resolution highly-sensitive proton-detected ssNMR spectra, and long ^{15}N coherence life times.[30,34,85] Figure 39a shows representative examples of residue-wise $R_{1\rho}$ RD profiles obtained on a sample of deuterated microcrystalline ubiquitin, that has been re-protonated at exchangeable sites to 50 %. ^{15}N $R_{1\rho}$ data have been measured at MAS frequency of 39.5 kHz, and spin-lock rf field strengths of 2-15 kHz, i.e. far from the n=1 rotary resonance condition (which is at 39.5 kHz). The reported rate constants are on-resonance $R_{1\rho}$, i.e. the R_1 contribution in the tilted rotating frame has been eliminated (using standard formulae[73]).

For the vast majority of residues, e.g. residues Ile 3, Leu 15, Lys 33 and Gly 47 in Figure 39a, we find that the RD profiles are flat over the entire range of rf field strengths. This finding confirms

that coherent dephasing is indeed efficiently suppressed by deuteration and fast MAS; it further suggests that non-flat $R_{1\rho}$ RD profiles can safely be ascribed to motional processes. Indeed, for a few residues we observe non-flat $R_{1\rho}$ RD curves, i.e. increased relaxation rate constant at low spin-lock rf fields, as expected for the Bloch-McConnell regime of exchange. The residues with such non-flat ^{15}N $R_{1\rho}$ RD profiles are located in a well-defined region of ubiquitin, in the N-terminal part of the helix and a loop that is hydrogen-bonded to this helix (residues Ile 23, Lys 27, Glu 51, Asp 52, Arg 54, Thr 55). Conformational exchange in this region of the protein has been reported in numerous studies in solution-state,[75,100,101] and we have recently also reported conformational exchange in this part of the protein in microcrystals from Carr-Purcell-Meiboom-Gill (CPMG) RD and multiple-quantum relaxation experiments.[97]

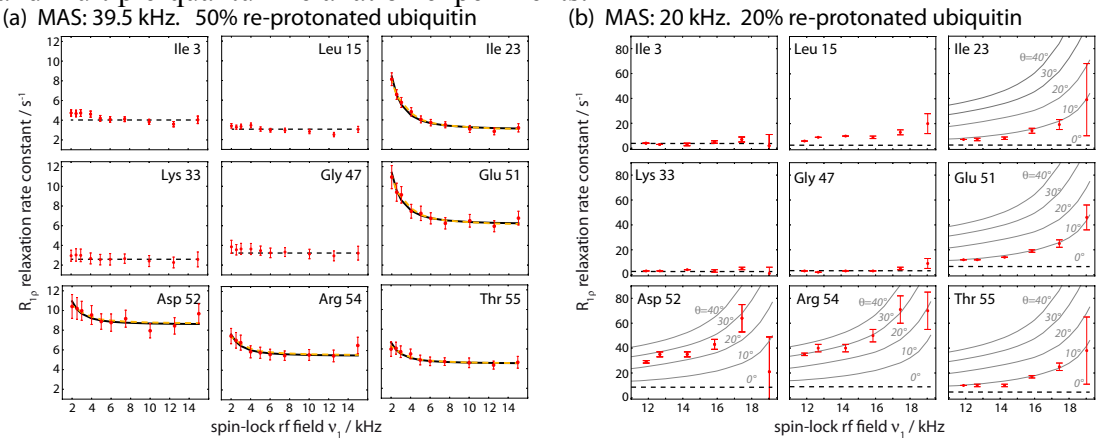

Figure 39. Experimental 15N RD data obtained on perdeuterated ubiquitin at a sample temperature of 300K, obtained from proton-detected experiments. Plotted is the on-resonance R1ρ, i.e. corrected for chemical-shift offset (see Supporting Information). (a) RD profiles obtained at 39.5 kHz MAS and low spin-lock rf field strengths of 2-15 kHz. Solid black lines show the result of a Bloch-McConnell fit of a two-state exchange model using only R1ρ-derived data, while orange lines are derived from a fit that includes CPMG data for residues 23, 27, 55 at 600 MHz, as reported earlier. Straight dashed lines (constant R1ρ rate) in panels (a) and (b) show the relaxation rate constant obtained at 39.5 kHz MAS and 15 kHz spin-lock field strength, which is considered as free from exchange effects. (b) RD profiles obtained at 20 kHz MAS on a fully deuterated, 20% re-protonated sample of ubiquitin.Solid lines show simulated $R_{1\rho}$ RD profiles assuming an exchange rate k_{ex} = 2900 s^{-1} and population p_B = 9.3%. All available RD profiles, as well as experimental details are shown in the Supporting Information.

6.4 Kinetics and thermodynamics of conformational exchange: fitting the Bloch-McConnell-regime of $R_{1\rho}$ dispersion curves

In order to obtain quantitative insight into the exchange process occurring in this part of the protein, we have fitted an exchange model to the $R_{1\rho}$ RD profiles of these residues using the Bloch-McConnell formalism. The application of this formalism is strictly speaking not correct in MAS ssNMR if bond reorientation is involved (cf. Figure 38). However, it appears justified here by the fact that the RD curves of Figure 39 were collected in a range of rf fields well outside the rotary-resonance conditions; bond angle fluctuations have only very small impact on $R_{1\rho}$ RD in this regime, especially when changes in the bond vector orientations are small (cf. Figure 38). That bond angle fluctuations are indeed rather small is justified *a posteriori* with independent measurements (*vide infra*). We performed a fit of a two-state exchange model to the $R_{1\rho}$–derived RD profiles of residues 23, 27, 51, 52, 54 and 55 (Figure 39). Because of their close spatial proximity, we assumed that these residues are involved in the same exchange process. Consequently, the exchange rate constant, $k_{ex}=k_{AB}+k_{BA}$ and minor-state population, p_B, were assumed to be identical for all these residues, and only the chemical-shift differences between major and minor state, $\Delta\delta$, which are sensitive to the local-environment changes, were assumed to be specific to individual residues. Solid lines in Figure 39a show best-fit curves of this fit. The fit yields an exchange rate constant k_{ex} of 8600±1700 s^{-1} and a minor-state population p_B of 3.1±1.2%. Residue-wise chemical-shift differences $\Delta\delta$ are in the range of 2-5 ppm.

In order to investigate the reliability of these results, obtained from a single $R_{1\rho}$ RD measurement, we explored the inclusion of additional, independent data sets: a first possibility, often used in solution-state NMR, would be the measurement of $R_{1\rho}$ RD at additional static magnetic field strengths (requiring, however, access to another spectrometer equipped with a fast-MAS probe). As an alternative, we use here a combined fit with CPMG RD data, obtained previously under similar conditions of fast-MAS and deuteration (see chapter 5). CPMG RD is sensitive to exchange processes on µs-ms time scales, making a combined fit with $R_{1\rho}$ possible. Such an analysis of the present $R_{1\rho}$ RD data with CPMG data, also obtained at 14.1 T magnetic field strength, yields values of $\Delta\delta$ that are very similar to the ones obtained from the above fit of only $R_{1\rho}$ RD data. The obtained exchange rate k_{ex} is 2900 ± 140 s^{-1}, and the population p_B is 9.3 ± 0.6%. Although these values slightly differ from the ones obtained from fitting only a single $R_{1\rho}$ RD data set (where k_{ex}=8600±1700 s^{-1}, p_B=3.1±1.2%) it is noteworthy that the fit curves of the combined $R_{1\rho}$/CPMG fit, shown as orange lines in Figure 39a, are almost indistinguishable from the fits of $R_{1\rho}$ data only, which shows that the present data are in excellent agreement with independent CPMG data. The differences of the fitted parameters point to the well-known fact that it is difficult to disentangle all fit parameters from a single measurement (here, a single B_0 field strength).

The $R_{1\rho}$ RD experiment has advantages over the previously proposed CPMG RD experiment, described in chapter 5. In solids, even at fast-MAS and high degrees of deuteration, measured R_2 rates contain a substantial amount of dipolar dephasing, in contrast to $R_{1\rho}$.[20] This has two important consequences: (i) due to the more rapid coherence decay, sensitivity in the CPMG experiment is significantly lower than in the $R_{1\rho}$ experiment. (ii) The remaining coherent contributions to the effective R_2 rates in a CPMG experiment are almost, but not entirely independent of the CPMG frequency.[97] Thus, observed variations of the effective R_2 in the CPMG experiment may to some extent be artefactual. We note that the time scales probed by $R_{1\rho}$ and CPMG RD experiments overlap but are not exactly identical, such that the approaches should be considered as complementary.

As we outlined already in chapter 5, the conformational exchange process found in microcrystalline ubiquitin is clearly different from the one in solution state. In solids, at 300 K the exchange occurs at a rate of about 3000 s^{-1}. In solution state the same part of ubiquitin undergoes conformational exchange, but the process is much faster than observed here. Even at 20K lower temperature than what was used here, the exchange occurs at about one order of magnitude faster than here (k_{ex} ~12500-25000s^{-1}).[75,100,101] At 298 K, a similar temperature as used here, the $R_{1\rho}$ RD profile in solution e.g. for Ile 23 is flat (to within 0.5 s^{-1}),[101] which is in stark contrast to the pronounced dispersion of $R_{1\rho}$ seen in crystals in this study (see Figure 39). This is in agreement with the CPMG study (chapter 5), and we have ensured there also that this apparent slow-down of the motion is not due to the increased viscosity of the crystallization solution.
Our findings thus unequivocally establish that the motional process in microcrystals is slowed down compared to the one in solution state because of intermolecular contacts, acting as additional energy barriers for motion in the crystal.

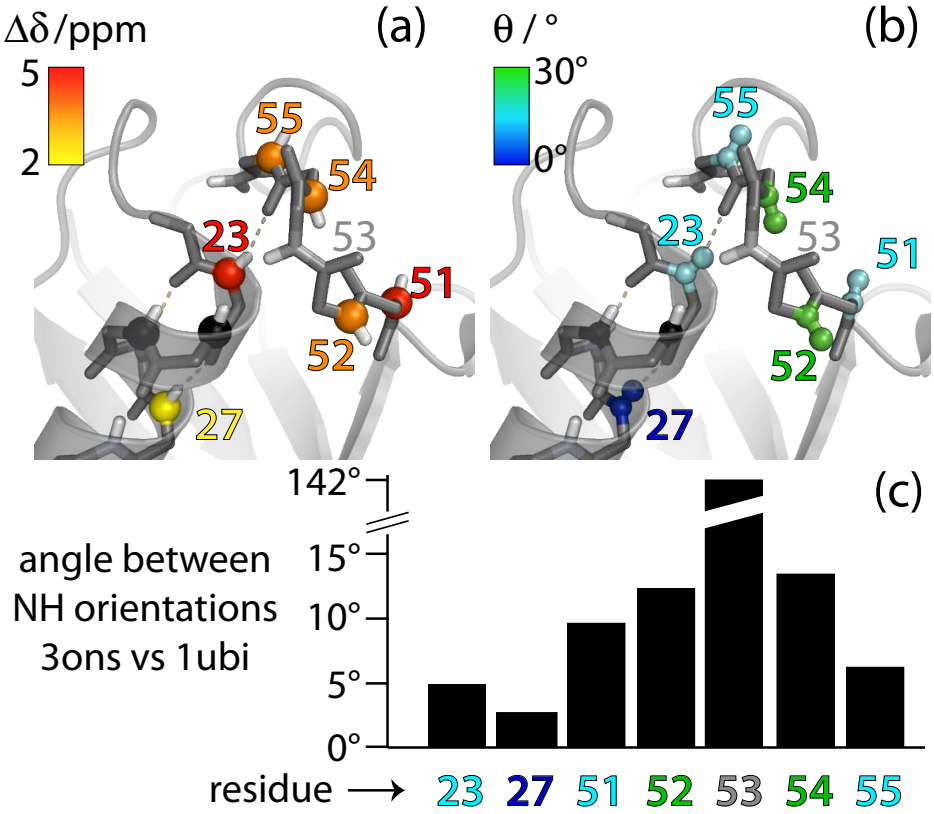

Figure 40. Residues involved in the conformational exchange process in ubiquitin. (a) Residue-wise chemical-shift differences Δδ (obtained from data in Figure 39a) and (b) jump angles θ (obtained from Figure 39b) are plotted onto the structure of ubiquitin crystals used in this study (pdb 3ons). Amides 24 and 25 (black spheres) are invisible in NH correlation spectra, presumably due to exchange broadening.[97] (c) Residue-wise differences of the N-H orientations in the crystal structure used here (type-II β-turn) and in a structure featuring a type-I β-turn (pdb 1ubi). These angles were obtained by aligning the two structures to all secondary structure elements and extracting the direction of the respective N-H bonds.

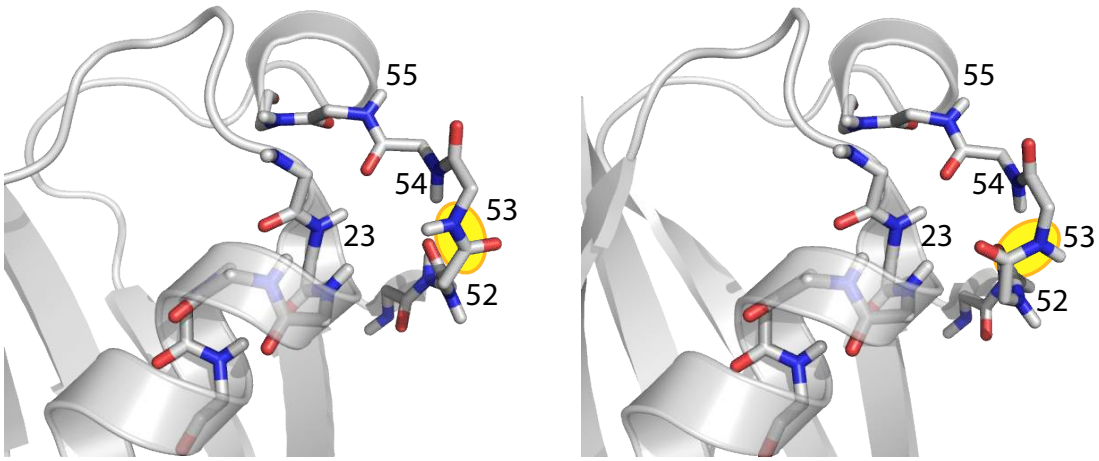

Figure 41. Comparison of crystal structures of ubiquitin. Left: The structure of microcrystals obtained in methyl-pentane-diol, used in this study (pdb entry 3ONS). Right: Crystal structure reported in pdb entry 1UBI. Note the different orientation of peptide plane 52/53, highlighted in yellow. The two structures were aligned along all residues located in secondary structure elements (1-7, 13-17, 23-34, 42-45, 48-50, 57-59, 65-70)

6.5 Beyond chemical shift information: bond orientation changes upon the structural transition to the excited state

Having thus established that $R_{1\rho}$ RD experiments at high MAS frequencies can provide information about the thermodynamics and kinetics of exchange, as well as site-specific chemical-shift values of the minor states, akin to the situation in solution-state NMR, we investigated whether additional structural information about the minor state may be obtained. As Figure 37 and Figure 38 show, ^{15}N $R_{1\rho}$ RD profiles in the vicinity of the rotary resonance condition ($\nu_1 \sim \nu_{MAS}$) are sensitive to the angle by which the NH bond (i.e. the dipolar coupling and ^{15}N CSA) is altered upon the conformational transition. This opens the possibility to measure the angular changes that arise in the conformational exchange process, by measuring $R_{1\rho}$ RD profiles close to the MAS frequency. For technical reasons we refrained from performing such measurements at high MAS frequencies, because the required high spin-lock field strengths ($\nu_1 \sim \nu_{MAS}$) would challenge the integrity of hardware and sample. Instead, we performed experiments at lower MAS frequency (20 kHz), where the rotary-resonance condition is met at lower rf field. To ensure that coherent contributions to the ^{15}N $R_{1\rho}$ decay remain negligible even at slower MAS, we employed a higher degree of deuteration (20% re-protonation of amide sites instead of 50%); the larger volume of the sample rotor that can be used at lower MAS frequency compensates the resulting sensitivity loss.

Figure 39b shows representative examples of ^{15}N $R_{1\rho}$ RD profiles obtained at spin-lock field strengths of ~12-19 kHz. Many of the residues, such as Ile 3, Leu 15, Lys 33 and Gly 47, show flat RD profiles over the entire range of sampled spin-lock field strengths, or only show an increase when the spin-lock field strength is within ~2-3 kHz from the n=1 rotary resonance condition. Interestingly, the obtained plateau values are similar to the values obtained at fast MAS, implying that coherent contributions to $R_{1\rho}$ are indeed efficiently suppressed, even at the lower MAS frequency. This finding, that is consistently found for many residues is apparently in contradiction to data shown by Lewandowski et al.[20] Their analysis of $R_{1\rho}$ rates in crystalline SH3 as a function of the MAS frequency indicated that at 20 kHz MAS the $R_{1\rho}$ rates do not match those at higher MAS frequency. The discrepancy of these data is at this point not clear. One possible reason is that the SH3 data were collected exclusively in a 1D manner, rather than in the site-resolved manner used here, and the data thus represent a superposition of many side chain and backbone sites. The CP efficiency at different MAS frequencies may differently weigh different sites, and this might explain why their $R_{1\rho}$ rates are MAS-dependent even in highly deuterated samples.

An increase of $R_{1\rho}$ when approaching the rotary resonance condition ($\nu_1=\nu_{MAS}$) can be understood from partial recoupling of dipolar-coupling and CSA interactions,[113] or from nanosecond motion via the $J(\omega_1-\omega_{MAS})$ spectral density.[114] It could thus arise even in the absence of µs conformational exchange. Strikingly, however, those residues that have the strongest dependency of $R_{1\rho}$ on the spin-lock field strength are the ones for which we have detected conformational exchange also through the isotropic CS mechanism, namely residues 23, 27, 51, 52, 54 and 55 (Figure 39). Based on the simulations in Figure 37 and Figure 38, which reveal that the angle of reorientation upon exchange impacts the RD profiles, we estimated the jump angles that can explain the RD profiles of Figure 39b. Grey curves in panel b show simulations that assume different angles. Extracted jump angles vary between the residues, and the largest angular fluctuations are observed for residues Asp 52 and Arg 54 (20-30°), while residues Ile 23, Lys 27, Glu 51 and Thr 55 show smaller reorientational motion along the exchange process, with jump angles of 10° or below. Residue Gly 53 is spectrally overlapped and no data are available.

It is interesting to confront these data with structural models of the exchange process. As deduced from various NMR data,[75,100,101] mutations[103] and inspections of different crystal structures of ubiquitin, the proposed mechanism of the exchange process involves a ~140-degree flip of peptide

plane D52/G53, and a rearrangement of the hydrogen bonding between this loop and the helix comprising residues 23-33. Figure 40 shows that in the microcrystal used in this study the NH bond of residue 53 points towards the helix (a so-called type-II β-turn); in most other structures deposited in the pdb it points outward (type-I β-turn, see Figure 41).

We assume here that the conformational exchange observed in our sample corresponds to a transition between these two types of β-turns. To test this hypothesis, we extracted the angles by which the NH orientations differ in representative X-ray structures featuring type-I and type-II β-turns. The largest differences in the NH orientations are found for Asp 52 and Arg 54, which are neighboring the peptide plane of Gly 53 that is flipped. Residues 23, 27, 51 and 55 show smaller differences of their respective NH bond orientation (Figure 40c). This is in good qualitative agreement with our data of Figure 39b, which also reveal the largest reorientational motion for Asp 52 and Arg 54, and significantly smaller jump angles for the other residues involved in the exchange process. These data indicate that $R_{1\rho}$ RD data can provide structural insight into excited states, in addition to chemical-shift data. This feature, together with the increased capabilities of relating chemical shifts to structure, may be of great value to derive structures of short-lived conformations, including for systems that were so far out of reach for atomic-resolution studies, such as very large or insoluble proteins.

7 Atomic model of a cell-wall cross-linking enzyme in complex with an intact bacterial peptidoglycan

7.1 Introduction

For over 70 years, peptidoglycan (PG) has played a pivotal role in the development of antibacterial chemotherapy.[116] In the quest for new drugs, the biosynthetic pathway of this ubiquitous cell wall polymer has been deciphered and essential peptidoglycan-synthesizing enzymes have been identified as putative antibacterial targets. Peptidoglycan precursors are synthesized in the cytoplasm, exported and assembled in the extracytoplasmic space by Penicillin-Binding Proteins (PBPs) that are the essential targets of β-lactam and glycopeptide antibiotics[117]. In ampicillin–resistant mutants of *Enterococcus faecium*[118] *a*nd in wild-type *Mycobacterium tuberculosis*[119] peptidoglycan cross-linking is not catalyzed by PBPs but by L,D-transpeptidases (Ldts). The Ldt from *Bacillus subtilis* (Ldt_{Bs}) was shown to catalyze this reaction *in vitro*[120]. Ldt_{Bs} consists of an N-terminal Lysin-Motif domain (LysM, residues 1 to 54) linked to the C-terminal catalytic domain (residues 55 to 169). The two domains have close contacts, remaining in a fixed relative orientation, as shown by NMR and X-ray studies.[121,122] The catalytic domains of Ldt_{Bs} and Ldts from *E. faecium* (Ldt_{fm})[123] and *M. tuberculosis* (Ldt_{Mt2}, Ldt_{Mt1})[124-126] display similar folds but the proteins have different domain compositions. The active site of Ldts contains a catalytic cysteine, which forms a covalent adduct with the tetrapeptide stem used as the acyl donor in the cross-linking reaction. Then, the Cys-bound tripeptide stem reacts with an adjacent peptide stem acting as an acyl acceptor, resulting in cross-linking and release of Ldt. The active-site Cys residue is also acylated by β-lactams of the carbapenem class resulting in irreversible enzyme inactivation.

LysM domains are widely spread in both prokaryotes and eukaryotes[127] and are known to bind non-covalently to peptidoglycan and chitin by interacting with *N*-acetylglucosamine residues.[128] In bacteria, various enzymes involved in peptidoglycan morphogenesis during growth and cell division are known to use one or several modular LysM domains to bind to peptidoglycan.[129,130] However, little is known on the role of LysM in determining the localization of the proteins in physiologically relevant sites within the peptidoglycan layer and how recognition of specific peptidoglycan patterns by LysM domains might modulate protein function. Addressing these questions ideally the study of intact peptidoglycan.

Atomic-resolution studies of proteins interacting with an intact bacterial cell wall are challenging. The peptidoglycan sacculus is a gigadalton-large, dynamic and microscopically heterogeneous structure, which hampers structural investigations by X-ray crystallography as well as solution-state NMR. Electron cryotomography and atomic-force microscopy offer insight into the overall structure and architecture of peptidoglycan, but the resolution presently obtained with these techniques does not allow resolving structural details of protein/peptidoglycan complexes at atomic resolution. The considerable flexibility of peptidoglycan[131] represents a further challenge for EM and AFM. For these reasons, there are currently no atomic-resolution data available about the structure of proteins in interaction with intact cell wall peptidoglycan, or about the dynamics of such complexes. Fragments of peptidoglycan may be used to reconstitute complexes, which may crystallize or be amenable to solution-state NMR.[132] However, these fragments may only partially reproduce the structure and affinities of the intact cell wall.

Solid-state NMR (ssNMR) can circumvent these limitations, because it provides atomic resolution, independently from the size or crystallinity of the molecular system studied. SsNMR has been applied in a few cases to entire organelles, membranes or whole cells.[11,133] In the case of peptidoglycan, its repetitive nature, composed of disaccharide-peptide building blocks (see Figure 43A), and flexibility lead to relatively simple and well-resolved spectra. In the context of bacterial

cell wall, ssNMR has proven to be a useful tool to obtain information about chemical modifications, local structure and dynamics of peptidoglycan, as well as interactions of the polymer with antibiotics and ions.[131,134,135] Here we show for the first time that it provides even information about the structure and dynamics of a protein/PG complex, by investigating the interaction of the L,D-transpeptidase Ldt_{Bs} with its physiological substrate, the peptidoglycan from *B. subtilis*.

7.2 Experimental Section

7.2.1 Sample preparation

Samples of *B. subtilis* peptidoglycan were prepared as described previously.[135] Briefly, *B. subtilis* strain 168 cells were grown in rich medium, and harvested at an OD_{600} of ~0.7. The cell membranes and cytoplasm was removed by treatment with SDS, DNAse and RNAse. The samples were in aqueous suspension during the entire treatment, including the subsequent NMR measurements, and are well hydrated, retaining a high degree of flexibility. Proteins were produced by bacterial over-expression using standard protocols. After extensively washing the peptidoglycan with the protein buffer (50 mM HEPES, pH 7.2) by repeated resuspension and centrifugation cycles, protein-peptidoglycan samples were obtained by incubating peptidoglycan suspensions with Ldt_{Bs} solution (0.3-1 mM protein concentration). For solid-state NMR, this highly hydrated suspension was pelleted into either 1.6 mm or 3.2 mm ssNMR MAS rotors (Agilent) using a centrifugal device. A full 3.2 mm rotor, with a total sample mass of 25 mg wet protein/peptidoglycan pellet, typically contained about 3 mg protein. Different samples were used in this study, with proteins either unlabeled, u-[$^{13}C^{15}N$]- or u-[$^{2}H^{13}C^{15}N$]-labeled. Peptidoglycan was either unlabeled (for protein-detected experiments) or u-$^{13}C^{15}N$-labeled.

7.2.2 NMR spectroscopy and structure calculation

All NMR experiments reported in the main text were carried out on a Agilent 600 MHz VNMRS spectrometer, operating either with a MAS solid-state equipment (1.6 mm probe for ^{1}H-detected experiments or 3.2 mm triple-resonance HXY probe for ^{13}C-detected experiments), or a room-temperature solution-state probe. Additional ^{13}C-detected experiments reported in the Supporting Information were recorded on a 1000 MHz Bruker spectrometer with a 3.2 mm HCN probe. All experiments were performed at a sample temperature of 298 K, and temperature calibration in solids was performed using external temperature calibration with Kbr, which was found to be in very good agreement with temperature measurement of the bulk water line relative to the DSS signal in wet protein samples. Solid-state NMR experiments used MAS frequencies of either 7.716 kHz (for the $R18_1^7$ experiment on peptidoglycan), 12 or 12.5 kHz (for ^{13}C-detected experiments on Ldt_{Bs}) or 39 kHz (for ^{1}H-detected experiments on Ldt_{Bs}). Spectra were processed with nmrPipe and analyzed with CCPNMR or python scripts based on NMRglue. Dipolar-coupling data were fitted with the use of numerical spin simulations implemented in SIMPSON (for $R18_1^7$) or GAMMA (for REDOR) and in-house written python programs. Dipolar order parameters are given relative to rigid-limit values of the dipolar coupling, $D_{rigid,}$ based on 1.12 Å and 1.02 Å bond lengths for H-C and H-N, respectively, i.e. $S=D_{measured}/D_{rigid}$.

The docking was performed using HADDOCK/CNS protocols. As starting structures of the two binding partners we used the solution-NMR structure of Ldt_{Bs} and a set of ten structures of hexameric muropeptide fragment, as described in the Supporting Information. The docking protocol used ambiguous restraints to the protein residues that showed significant chemical-shift perturbation in H-N-CA experiments (larger than twice the standard deviation over the whole sequence). For the muropeptide, where no unambiguously identified binding sites are available, all atoms were defined as passive ambiguous interaction restraints. The knowledge about the catalytic site in Ldt_{Bs}, residue C142, was exploited by adding a distance restraint between the sulfur of C142 and the carbonyl of the DAP residue in one of the peptides of the hexameric muropeptide. Best convergence was achieved when the constraint was applied to the fifth di-saccharide-tetrapepeptide residue.

7.3 Results

7.3.1 Ldt_{Bs} tightly binds to peptidoglycan

Peptidoglycan is a highly flexible three-dimensional polymer, and its dynamic nature critically relies on the aqueous environment. Consequently, only samples containing well-hydrated pellets of peptidoglycan were used for all experiments that aim at visualizing its interactions with Ldt_{Bs} protein, and the impact of this binding on its dynamics. Upon incubating *B. subtilis* peptidoglycan suspension with its the purified Ldt_{Bs} protein, the protein concentration in the supernatant dropped (as evidenced by spectrophotometry at 280 nm), indicating that the protein binds to the peptidoglycan sacculi. This apparent absorption of the protein by peptidoglycan sacculi was found to be saturable, i.e. when adding protein above a certain protein:peptidoglycan ratio, the excess protein stayed in solution; typically, this ratio was of the order of about 1.5 mg of protein for 10 mg of ultracentrifuge-pelleted wet peptidoglycan. In order to obtain atomistic details of this interaction, we transferred the protein/peptidoglycan sacculi suspension into MAS rotors for analysis by solid-state NMR.

In a first sample, containing unlabeled peptidoglycan and u-[^{13}C,^{15}N]-labeled Ldt_{Bs}, we visualized the fate of the protein through one-dimensional ^{13}C-detected experiments. Three types of experiments were used that employ either (I) direct ^{13}C excitation, (ii) cross-polarization from ^{1}H to ^{13}C prior to ^{13}C-detection or (iii) scalar-coupling based refocused-INEPT transfer. The first type of experiment detects all the protein in the sample, independently of whether the protein is tightly bound to peptidoglycan or tumbling freely in the surrounding solution. In the second type of experiment, only protein bound to the (solid-like) peptidoglycan sacculi is detectable, while freely tumbling protein would be undetectable due to the reorientational motion. The third type of experiment, refocused INEPT, would lead to detectable signal only in the presence of large-amplitude flexibility, such as overall tumbling. These experiments thus provide a qualitative picture of the protein's dynamic behavior. Intense protein signal is observed in the cross-polarization experiment indicating that Ldt_{Bs} is tightly bound to peptidoglycan, adopting the spectroscopic properties of a solid-state sample (Figure 42). In contrast, in a refocused-INEPT experiment we do not detect signal (data not shown), confirming the view that Ldt_{Bs} is not freely tumbling. Taken together, these data reveal that upon incubation with PG, Ldt_{Bs} adopts the properties of a solid-state sample, showing its attachment to the large, solid-like peptidoglycan sacculi.

In order to obtain more quantitative insight into the dynamics of the protein in this state, we investigated the amide ^{1}H-^{15}N dipolar couplings of the backbone amide sites. The dipolar-coupling can be directly related to the order parameter that describes the motional freedom of the individual ^{1}H-^{15}N bond vector over time scales faster than tens of microseconds. This order parameter, S, ranges from 0 for complete disorder to 1 in the absence of any local or global motion. We used a one-dimensional version of a REDOR experiment[26,27] with ^{1}H detection, and integrated the whole amide region in this measurement, to obtain an effective average value. The bulk amide H-N order parameter is S=0.82 (i.e., S^2=0.67, data not shown here). Although this value is clearly lower than what one would expect for a completely immobilized protein in a crystal or a precipitate (where S is generally larger than 0.9), it confirms that the protein has adopted the spectroscopic properties of a protein in the solid state. (In a freely tumbling protein the dipolar-coupling order parameter is zero.) The fact that the order parameter is lower than in typical crystalline samples might point to the fact that the protein is attached to PG, which itself shows relatively large amplitude motions (see section below). Further evidence for such overall motion of the protein comes from a comparison of the REDOR-derived order parameter with solution-state order parameters: the order parameters of internal motion in Ldt_{Bs}, as expressed by a model-free order parameter are around S^2=0.8, significantly larger than the value of S^2=0.67 found in the solid-state measurement. Residual overall flexibility of PG would necessarily impart some degree of overall motion on the attached Ldt_{Bs} protein.

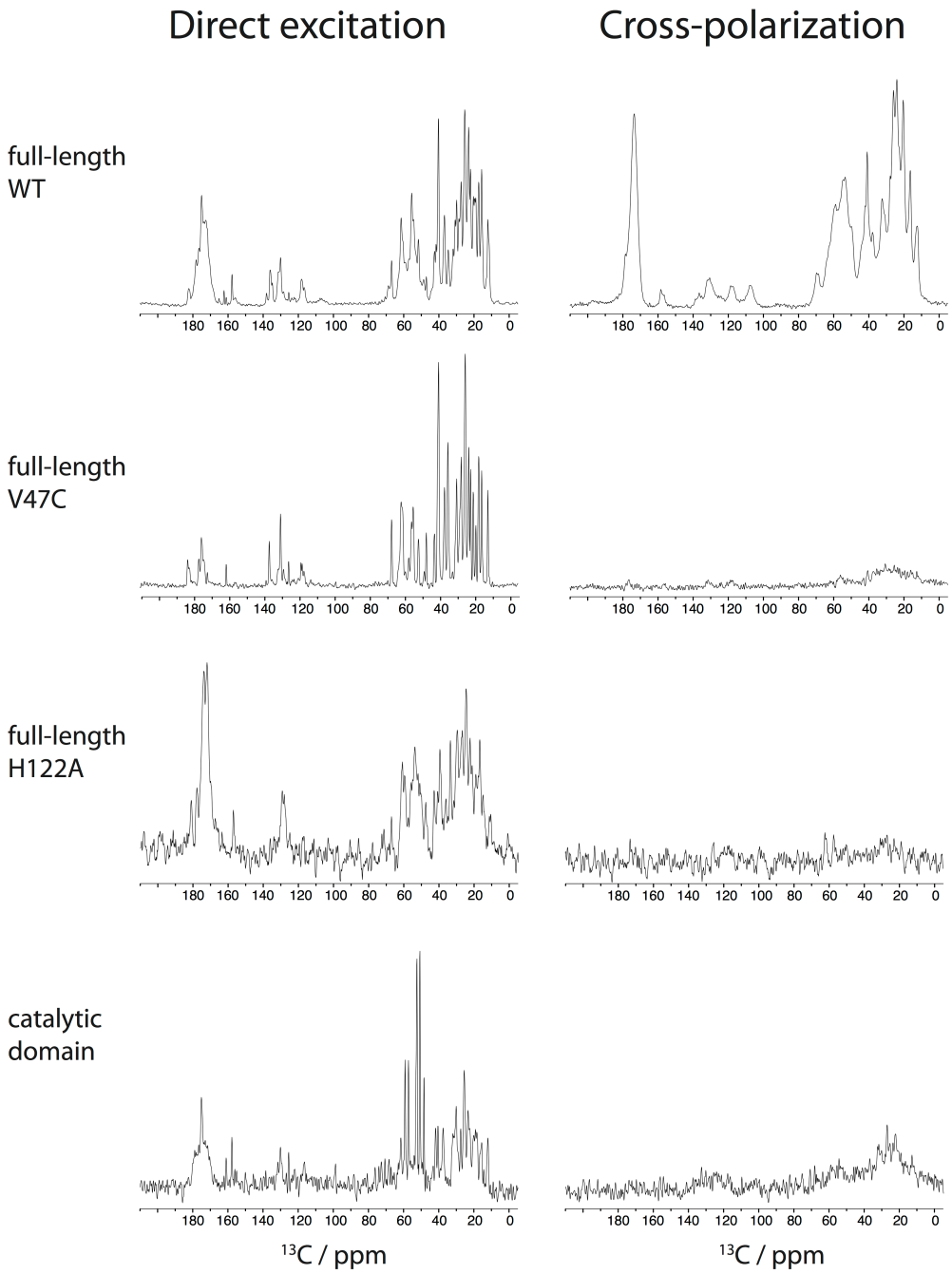

Figure 42. 1D ^{13}C solid-state NMR spectra of peptidoglycan:protein samples collected at a MAS spinning rate of 12.5 kHz and a sample temperature of 298 K. Spectra were collected with different [U-^{13}C,^{15}N] Ldt_{Bs} constructs: A) full length Ldt_{Bs}; B) full length V47C Ldt_{Bs} mutant; C) full length H122A Ldt_{Bs} mutant; D) the catalytic domain of Ldt_{Bs} (residues 55-169). Spectra on the left were recorded with a direct ^{13}C excitation (90° pulse) followed by a 20 ms ^{13}C acquisition period, during which a TPPM proton decoupling scheme with approximately 95 kHz radiofrequency field was applied. These spectra show the overall protein content in the rotor. Spectra on the right were collected using a ^{1}H-^{13}C cross-polarization (CP) of 1.5 ms duration. The ^{1}H radiofrequency field was ramped from approximately 65 to 75 kHz, and the ^{13}C rf field was chosen to match the n=1 Hartmann-Hahn condition (~60 kHz). TPPM decoupling and acquisition time were the same as in the direct-excitation spectra. These CP spectra reflect the portion of the protein that resides on the peptidoglycan and thus shows a solid-like behavior. These data show that while the wild-type full-length protein has the spectroscopic properties of a solid state (efficient CP transfer), mutation or truncation leads to a drop in this transfer efficiency, showing the protein not to be tightly bound to peptidoglycan.

We have also measured bulk ^{15}N $R_{1\rho}$ relaxation rates in a highly deuterated protein at fast magic-angle spinning, which are sensitive to motion on time scales of tens of nanoseconds to microseconds. We find a bulk $R_{1\rho}$ relaxation rate of 14 ± 3 s^{-1}, significantly higher than corresponding values in microcrystalline proteins,[34–36] where typical average $R_{1\rho}$ are below 5 s^{-1}.

Taken together, these dynamics measurements show that Ldt_{Bs} in the presence of peptidoglycan adopts the behavior of a protein in the solid state, but it has slightly higher flexibility than proteins embedded in a crystal lattice, presumably due to the flexibility of its binding partner, peptidoglycan. This prompted us to analyze the dynamics of peptidoglycan in bound and unbound states.

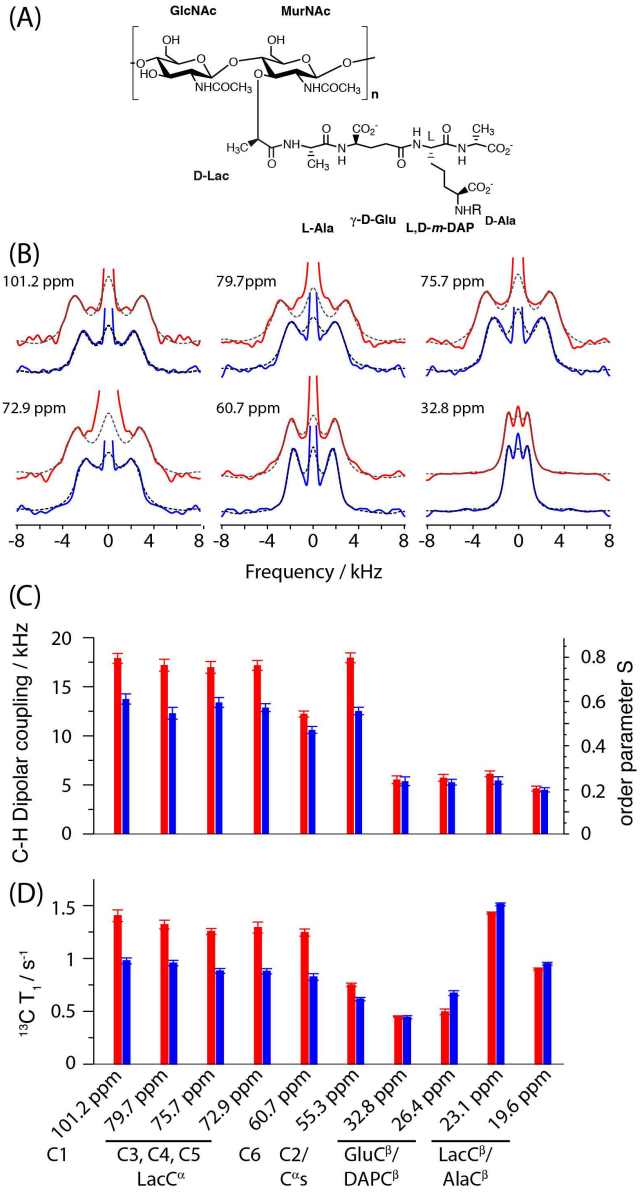

Figure 43. The impact of protein binding on peptidoglycan dynamics. (A) Chemical structure of peptidoglycan. (B) Measurement of one-bond ^{1}H-^{13}C dipolar couplings in peptidoglycan, using a windowed $R18_1^7$ sequence at a MAS frequency of 7.716 kHz. Dipolar splittings are measured in the absence (blue) and presence (red) of Ldt_{Bs}. Dotted lines show best-fit curves, based on numerical simulations of the pulse sequence (see Methods section). (C) C-H dipolar couplings in peptidoglycan without (blue) and with (red) Ldt_{Bs}. (D) ^{13}C T_1 relaxation time constants without (blue) and with (red) Ldt_{Bs}.

7.3.2 Peptidoglycan dynamics in the protein-bound state

In order to obtain insight into the effect of protein binding on peptidoglycan conformation and dynamics we performed ^{13}C-detected experiments on samples containing [U-^{13}C,^{15}N]-labeled peptidoglycan.

Figure 43B shows site-resolved measurements of ^{1}H-^{13}C dipolar couplings for various sites of the peptide and sugar moieties in peptidoglycan samples with and without Ldt_{Bs}, measured using an improved version[136] of a proton-detected local field $R18_1^7$ sequence.[37] These dipolar couplings

directly reflect the degree of motional freedom of the bond vectors. In the absence of protein, we find order parameters of sugar-bonds in the range of S=0.6. C-H bonds of the peptide moieties have values in the range of S=0.2-0.3. These values are clearly much lower than typical order parameters found in rigid biomolecules, such as microcrystalline, fibrillar or precipitated protein samples, that have typical values around 0.9 for ^{1}H-^{13}C and ^{1}H-^{15}N bonds.[41,43,54] The significant flexibility of peptidoglycan, reflected in these low values of S, has been reported for hydrated peptidoglycan before.[19] In the presence of Ldt_{Bs}, the order parameters of the sugar moieties are markedly increased from S~0.6 to values in the range of S~0.8 (Figure 43C), similar to Ldt_{Bs}'s NH order parameters discussed in the previous section. For the peptide parts of PG, which are more flexible than the sugar parts, the presence of protein does not lead to significant changes in order parameters. ^{13}C R_1 relaxation parameters, which are sensitive to amplitudes and time scales of motion, provide a very similar picture to the one obtained from dipolar couplings (Figure 43D): the presence of protein leads to prolonged T_1 relaxation time constants of the glycan moieties, while the peptide sites have shorter T_1 relaxation times which are almost identical with and without protein. These measurements therefore unambiguously show that peptidoglycan dynamics are impacted by the presence of protein. The chemical-shift changes upon binding are much less pronounced than the changes in dynamics (data not shown here). This may be related to the known fact that sugar-protein interactions generally lead only to relatively small shifts.[137]

7.3.3 Atomic model of the complex from ^{1}H-detected ssNMR experiments

Having thus demonstrated the complex formation between Ldt_{Bs} and *B. subtilis* peptidoglycan, we attempted to derive an atomic model of this complex. In order to identify the binding site on Ldt_{Bs} at atomic resolution, we investigated the chemical-shift changes upon binding by comparing Ldt_{Bs} NMR spectra of protein in solution (i.e. in the absence of PG) and bound to PG. Care was taken to ensure that the protein, buffer and temperature conditions were identical in the two cases; solution-state NMR spectra were collected with the protein that was subsequently incubated with PG for ssNMR. Figure 44A shows the overlay of two-dimensional proton-detected ^{1}H-^{15}N correlation spectra of [u-^{2}H,^{13}C,^{15}N] Ldt_{Bs} in solution without peptidoglycan (blue), and in the solid state, bound to peptidoglycan (red; collected at a MAS frequency of 39 kHz). The close similarity of peak positions in the two spectra in Figure 44A immediately shows that the protein conserves the same global fold upon peptidoglycan interaction. Significant resonance overlap in the solid-state NMR spectrum of this 19 kDa protein hampers the extraction of an extensive set of site-resolved resonance positions from such 2D spectra. This prompted us to collect three-dimensional spectra. The intrinsic sensitivity of higher-dimensional spectra is lower, which is a challenge particularly in the present context, where the majority of the sample volume is occupied by peptidoglycan rather than protein. In this context, proton-detected ssNMR experiments on a deuterated protein sample turned out to be crucial. The improved sensitivity of proton-detection under fast MAS allowed the collection of a 3D (H^{N})CANH^{N} ^{1}H-^{13}C$^{\alpha}$-^{15}N correlation experiment. Figure 44B shows excerpts from this 3D experiment, overlaid with a corresponding solution-state HNCA experiment. Figure 2C shows the chemical-shift perturbation (CSP) upon binding, i.e. the combined difference of ^{1}H-^{13}C$^{\alpha}$-^{15}N chemical shifts, as a function of the residue number, as derived from these 3D spectra. Residues with a CSP greater than two standard deviations are represented in red on the free Ldt_{Bs} structure in Figure 45A. Residues with significant chemical-shift perturbation upon the peptidoglycan interaction are located both in the LysM and catalytic domains.

Based on these residue-specific interaction data, we calculated a structural model of the complex using HADDOCK, a data-driven docking protocol based on CNS. In this approach, residue-specific CSP data are used as ambiguous distance restraints between the respective protein residues and the peptidoglycan during an energy minimization process performed on the two interacting molecules. For Ldt_{Bs}, the input structure was the solution-state NMR-derived structure of the protein. For peptidoglycan, a fragment consisting of six di-saccharide-tetrapeptide subunits was chosen. This fragment is sufficiently long to cover the whole binding surface of Ldt_{Bs}; longer

fragments lead to similar solutions but increase the number of redundant solutions in which the PG fragment is translationally shifted. Since peptidoglycan is flexible, a set of ten structures was generated for the hexamer by an energy-minimization process, and docking was performed with all these conformers as starting structures. The catalytic mechanism of Ldt_{Bs} involves the formation of a covalent link between the C142 of Ldt_{Bs} and the carbonyl of L-Lys in the donor peptide stem. For this reason, a distance restraint between the C142 sulfur and the carbonyl carbon of one of the DAP residues was used in addition to the CSP data of Figure 44C for the docking procedure. As discussed in the Supporting Information, this restraint improves the convergence of the calculation. However, the result without the restraint is similar in the sense that the final solution with the C142-restraint is among the two best-scoring solutions in a calculation performed without this restraint (data not shown here).

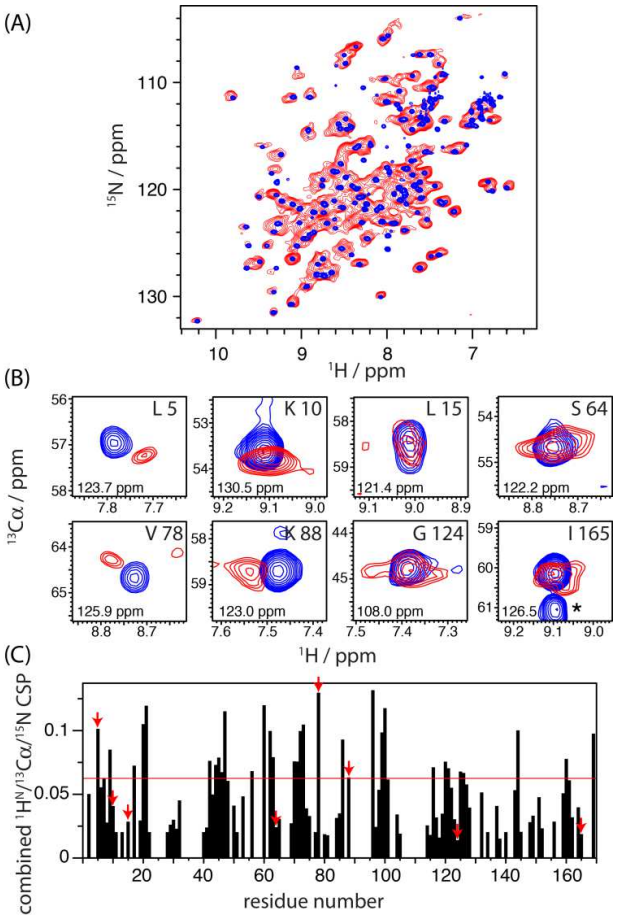

Figure 44. ssNMR characterization of the interaction between Ldt_{Bs} and *B. subtilis* peptidoglycan. A) Comparison of 1H-15N correlation spectra of [U-2H,13Cn15N] Ldt_{Bs} in solution (blue) and in the presence of peptidoglycan (red). The latter spectrum was collected at a MAS frequency of 39 kHz, using cross-polarization (CP) transfer steps. B) Representative excerpts from 3D 1H-13C$^{\alpha}$-15N correlation spectra. The peak labeled with an asterisk (lower right) arises from the correlation to the C$^{\alpha}$ of the preceding residue 164, which cannot be observed in the solid state due to pulse sequence design. Numbers in each panel refer to the 15N chemical shift at which the displayed 1H-13C planes were extracted. C) Combined chemical shift perturbations (CSP) between free and bound protein, calculated as the square root of the sum of the squared absolute chemical shift difference in the 1H,13C, 15N dimensions, weighted by the relative gyromagnetic ratios. Red arrows indicate the residues shown in panel (B). The red horizontal line displays two standard deviations over all residues.

The lowest energy model of this calculation are presented in Figure 45B. In these models, the LysM domain interacts with each of the six muropeptide subunits. Additional contacts occur between residues 90-100, 115-125, and 142 of the catalytic domain and muropeptides 2 to 5 of the hexamer.

The interaction site of the peptidoglycan on the LysM domain of Ldt_{Bs} differ from the one observed for other LysM domains in complex with short soluble oligosaccharides.[138] The two types of complexes involved the same highly conserved LysM residues but an opposite orientation of the sugar residues (see Figure 46). The novel interaction geometry proposed here not only accounts for binding of the LysM domain of Ldt_{Bs} to peptidoglycan but also for a catalytically productive orientation of the stem peptide with respect to C142 of the catalytic domain.

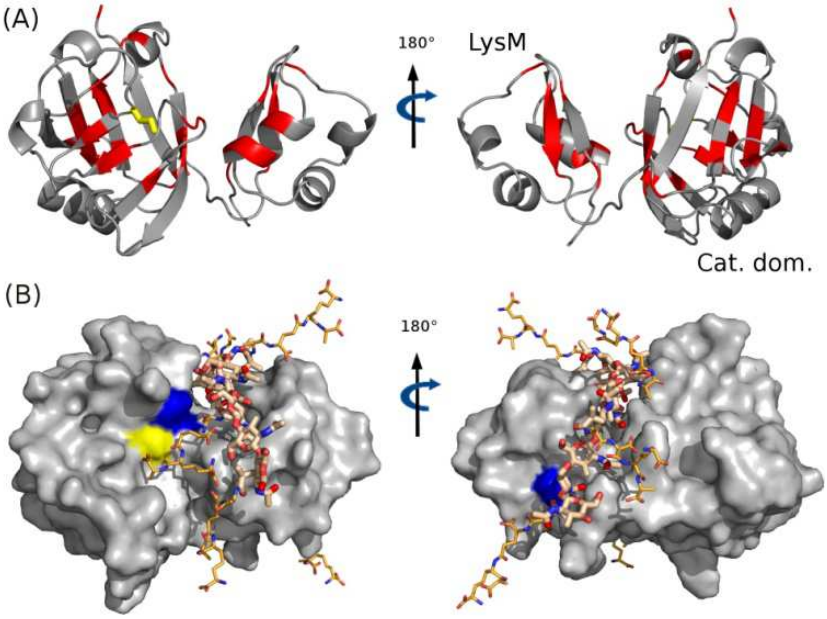

Figure 45. NMR chemical-shift perturbation (CSP) induced by the peptidoglycan on Ldt_{Bs} and result of the HADDOCK calculation. A) CSP are displayed in red on a ribbon representation of Ldt_{Bs} B) Lowest energy structure obtained for the peptidoglycan-Ldt_{Bs} complex. The catalytic cysteine (C142) is shown in yellow. The residues shown in blue are H122 (left panel) and V47 (right panel), used for mutation experiments.

7.3.4 Mutants and isolated domains have different binding affinities than full-length wild-type Ldt_{Bs}

In order to independently validate this structural model, we explored how a perturbation of the binding site would impact the binding. To this end we performed site-directed mutagenesis of Ldt_{Bs}-residues V47 and H122 which in our structural model are predicted to be in the interaction site (shown in blue in Figure 45B). Residue V47 of the LysM domain interacts with the MurNAc and peptide moieties of the second disaccharide-peptide subunit of the hexamer, and H122 is close to the DAP residue of the fifth disaccharide-peptide. NMR spectra of the mutant proteins in solution in the absence of peptidoglycan showed that the V47C and H122A substitutions did not perturb the overall structure of Ldt_{Bs}. Moreover, the substitutions did not prevent binding of Ldt_{Bs} to peptidoglycan since pull-down experiments revealed the expected decrease in the absorbance at 280 nm in the supernantant upon incubation, similar to wild-type Ldt_{Bs}. As with wild-type protein, we performed one-dimensional ^{13}C-detected experiments to follow the behavior of the protein. The presence of the two proteins in the PG-pellet is evidenced by direct-excitation ^{13}C ssNMR spectra (Figure 42). However, the ^{1}H-^{13}C cross-polarization transfer was almost entirely suppressed in both variants, in strong contrast to the wild-type protein. This cancellation of the ^{1}H-^{13}C dipolar transfer can be explained by dynamics, such as a rapid exchange between free and bound forms of the protein, which averages out the dipolar coupling. Thus, these data show that upon mutation of V47 or H122, Ldt_{Bs} interacts less tightly with peptidoglycan and thereby changes its spectroscopic behavior. This finding confirms the implication of these residues in the complex formation.

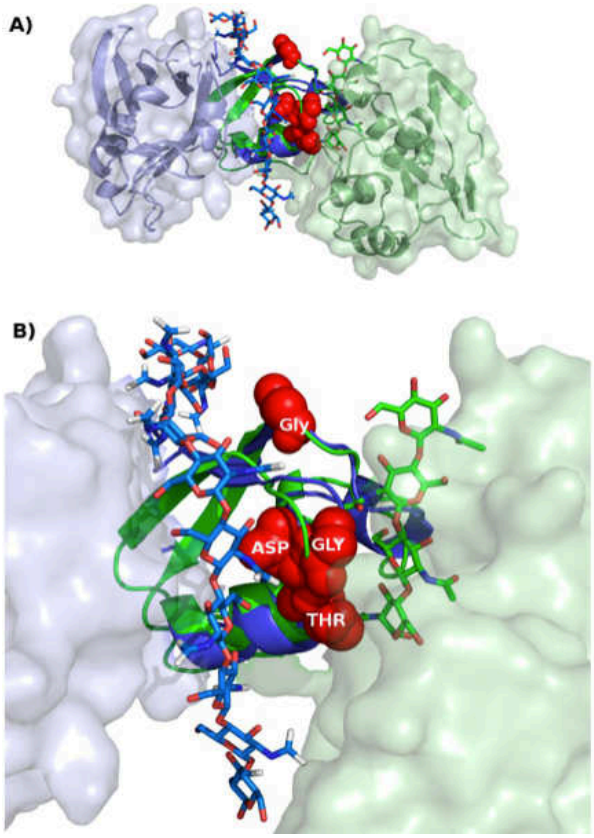

Figure 46. Comparison of LysM-oligosaccharide interaction sites in two different protein complexes. The peptidoglycan fragment-Ldt_{Bs} complex of the present study is compared to a chitin tetramer-*Cladosporium fulvum* effector Ecp6 complex (4B8V). The LysM domains of both complexes have been superimposed (RMSD 0.95 Å, sequence identity 35%) and are displayed as a ribbon whereas the rest of the proteins is represented with a semi-transparent surface. A) complete view of the superimposed proteins B) Enlargement of panel A centered on the two superimposed LysM domains. The muropeptide hexamer interacting in the groove formed by the Ldt_{Bs} LysM (blue ribbon) and catalytic (light blue surface) domains is displayed with blue sticks. The chitin tetramer interacting with one of the LysM domain (green ribbon) and the additional domain of the EPC6 receptor (light green surface) is shown with green sticks. The conserved residues described from consensus sequences of LysM domains are shown as red spheres and are all involved at the interface between the ligand and the LysM domain of the considered proteins, Ldt_{Bs} and Ecp6, respectively.

To evaluate the respective roles of the LysM and catalytic domains in the formation of the Ldt_{Bs}-peptidolgycan complex, the two domains were separately produced and individually incubated with peptidoglycan. A decrease in the supernatant absorbance upon incubation with peptidoglycan showed that both individual domains still interact with peptidoglycan. Likewise, direct-excitation ^{13}C ssNMR spectra confirmed the presence of the proteins in the peptidoglycan pellet (Figure 42). However, similar to the V47C and H122A mutants, the cross-polarization transfer was found to be very weak, showing that the interaction of the individual domains is less tight than the interaction of the full-length protein. Interestingly, for the LysM domain, we found efficient transfer in an INEPT-type experiment under MAS. This experiment selectively detects either highly flexible parts of a protein in a solid immobilized state, or proteins tumbling freely in solution, but it generally fails to detect proteins in a rigid solid-like state. The observation of LysM in the INEPT experiment can be rationalized by a rapid exchange of LysM between a free state in solution and a peptidoglycan-bound state. This observation prompted us to perform solution-state NMR experiments on the peptidoglycan/LysM slurry without MAS. Indeed, LysM is observable in solution-state NMR in the presence of peptidoglycan (Figure 47). 2D ^{1}H-^{15}N solution-state HSQC correlation spectra of LysM in the absence and presence of peptidoglycan allowed identification of the perturbed residues upon interaction (Figure 47D). Mapping the corresponding CSP data (Figure 47E) identifies the β-sheet structure of LysM as the peptidoglycan interaction site. This part is also involved in the interaction within the full-length protein. This structural element also comprises V47, that was shown to be important in the interaction from the above mutation experiments.

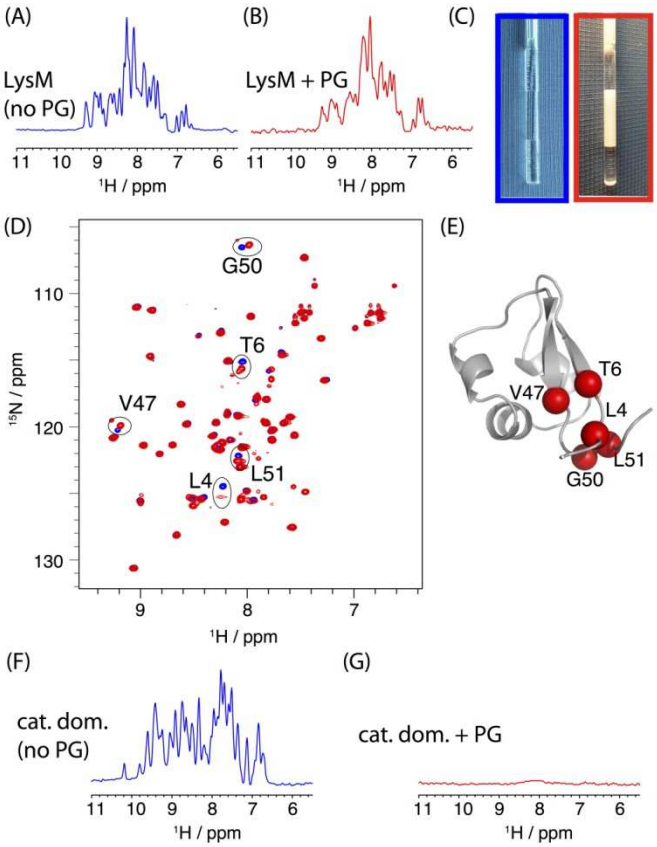

Figure 47. Solution-state NMR performed on the individual LysM and catalytic domains. A,B) 1D 1H NMR spectra of the LysM domain recorded in the absence (A, blue) or presence (B, red) of peptidoglycan. C) Photographs of the respective samples described in A) and B). (D) 1H-N5N HSQC spectra recorded on these two LysM samples. Peaks corresponding to residues with significant chemical shift perturbation (CSP) upon peptidoglycan interaction are highlighted. Residue-wise CSP plots are shown in Figure S7. (E) Position of the backbone sites of residues with significant CSP are show as red spheres. The orientation of the LysM domain is identical to that used in Figure 2A (right panel). (F, G) 1D 1H NMR spectra of the catalytic domain recorded in the absence (F, blue) or presence (G, red) of a peptidoglycan suspension. All 1D spectra resulted from 128 scans except for the spectrum in panel (G) for which 1024 scans were accumulated.

The catalytic domain shows a slightly different behavior. Unlike LysM, the protein is unobservable in INEPT experiments (Figure 47G), showing that it is not in fast exchange between bound and free states. The cross-polarization (CP) transfer is also inefficient (Figure 42), contrasting with the behavior of full-length Ldt_{Bs}, which suggests that the catalytic domain is not tightly attached to peptidoglycan. A possible explanation for this observed behavior is an exchange between different states (different bound state(s) and possibly also free states) on a microsecond-to-millisecond time scale. Such a dynamic exchange regime would render both INEPT and CP transfers inefficient.

Taken together, all the MAS ssNMR and solution-state NMR spectra show that the individual domains of Ldt_{Bs} interact with peptidoglycan and that the LysM binding sites are similar for the isolated domain and for the full-length protein. However, the affinities of individual domains are clearly lower than the affinity of full-length Ldt_{Bs}. This apparent reliance on both domains for high-affinity interaction is in agreement with our structural model, in which both domains make extensive contacts with peptidoglycan.

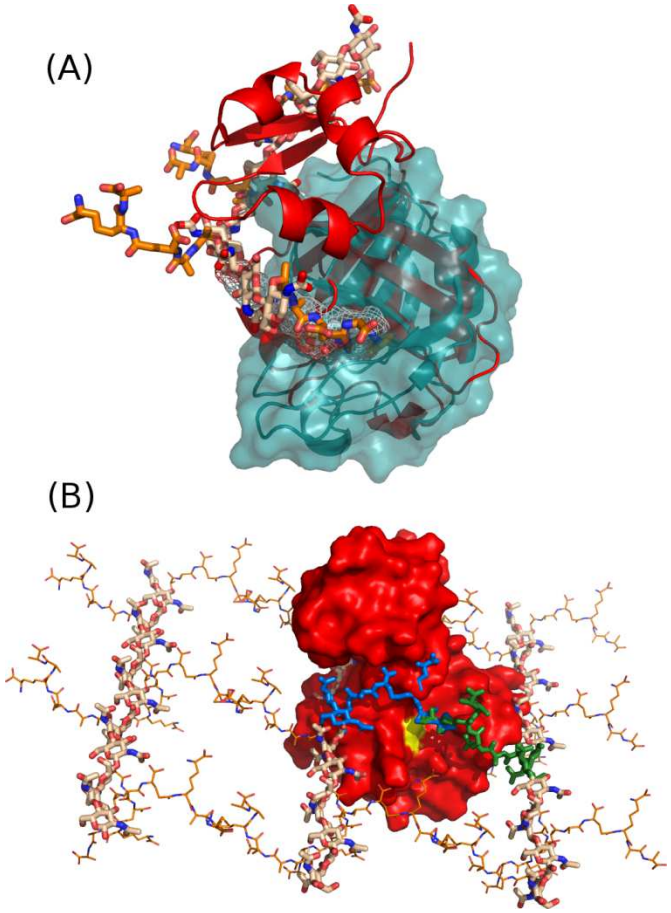

Figure 48. Possible localization of the peptidoglycan peptide stems into the catalytic pocket. A) Superimposition of our HADDOCK Ldt_{Bs}:peptidoglycan-hexamer model (Ldt_{Bs} cartoon structure in red and peptidoglycan in orange sticks) with the Ldt_{fm} acylenzyme structure (cyan cartoon and surface), with ertapenem (grey mesh). A peptide stem of peptidoglycan is localized in the same acyl donor pocket as the carbapenem antibiotic. B) Extension of our HADDOCK Ldt_{Bs}:peptidoglycan-hexamer model to a complete peptidoglycan polymer. The hexamer muropeptides of our model was overlapped with one of the glycosidic chain of the complete peptidoglycan polymer. The peptidoglycan was modeled using a threefold axis for the glycan chains. The peptide conformation was adapted to allow the cross-linking between adjacent glycan chains.[24] Possible acceptor and donor peptide stems are represented in green and blue, respectively. The catalytic cysteine is shown in yellow.

7.4 Discussion

Peptidoglycan cross-linking by Ldt_{Bs} and related L,D-transpeptidases involves two stem peptides that act as acyl donor and acyl acceptor. In the first step of the transpeptidation reaction, the catalytic cysteine forms a covalent thioester bond with the backbone carbonyl of the third residue of the acyl donor stem. This reaction can be blocked by β-lactam antibiotics of the carbapenem class, which also acylate the catalytic cysteine. The NMR structure of Ldt_{fm} L,D-transpeptidase covalently bound to the ertapenem carbapenem has recently been reported.[121] Figure 48A shows the superposition of this acylenzyme structure with the model derived here for the peptidoglycan-Ldt_{Bs} complex. Interestingly, the peptide stem of the fifth disaccharide-peptide subunit occupies the antibiotic pocket in our HADDOCK models. Thus, this peptide stem is likely to occupy the position of the acyl donor of the transpeptidation reaction.

To explore possible locations of the acceptor stem, we have represented our model in the context of a complete peptidoglycan structural model generated from a regular network (Figure 48B). To generate this new model, the glycosidic chain of the complete peptidoglycan structure was superimposed with the muropeptides hexamer of the HADDOCK model. As a result, one of the

muropeptides interacts through its disaccharide motif and peptide stem with the LysM and catalytic domains. In this muropeptide, the backbone carbonyl of the diaminopimelic acid in the third position of the stem peptide points towards the catalytic cysteine, playing the role of the acyl donor. At the same time, the peptide stem attached to a remote glycosidic chain points towards the catalytic cysteine, mimicking the acyl acceptor. This tentative model proposes the possible localization of the different partners required for the transpeptidation reaction.

7.5 Conclusions

In summary, we determined here the first atomic-resolution model of a protein (the L,D-transpeptidase Ldt_{Bs}) bound to intact peptidoglycan sacculi, based on solid-state NMR data. The binding mode of peptidoglycan in this model involves both the LysM and catalytic domains of Ldt_{Bs}. The glycosidic chain is located in the groove between the two domains and in this orientation one of the peptide stems can reach the catalytic cysteine residue. The inferred importance of both domains for high-affinity is supported by NMR experiments performed with isolated domains as well as site-directed mutagenesis. Our dipolar-coupling data show that peptidoglycan still retains considerable flexibility when protein is bound, although less than in the unbound state.

Proton-detected ssNMR has been found to be crucial in order to obtain the structural information reported here, and this study thus provides another example of the versatility of ^{1}H-detection in ssNMR.[27-29] The methodology employed here offers a general strategy for the structural investigation of protein/cell-wall complexes. It may significantly contribute in designing future antibiotics, which do not only target the catalytic site, but also the complete binding interface on the protein.

Future perspectives:
Studying functionally relevant motions in membrane proteins

8 Substrate translocation across the inner mitochondrial membrane

Membrane proteins are responsible for a wide range of key cellular functions including signal transduction, energy generation and transport. The structural plasticity of membrane proteins is important for their function. Large-scale rearrangements such as the opening and closing of channels drive many of the above biological processes. The inherent flexibility of membrane proteins is also underscored by the fact that x-ray studies of a number of proteins, were only possible when an inhibitor was present that freezes the dynamics and locks the protein in one conformation.[11] Despite the importance of these static pictures, it must be stressed that the "locked" conformation revealed in these structures may well be non-functional. It would, thus, be clearly beneficial to study membrane proteins in a form where they exhibit their native and functionally-important flexibility, and directly characterize their dynamics.

Here, I will focus on a particularly important class of membrane proteins, which is responsible for substrate translocation in the mitochondrion. The mitochondrion is an organelle in eukaryotic cells and is implicated in several human diseases including cancer and cardiac dysfunction, and it also plays a role in ageing. The central function of the mitochondrion is to provide energy in the form of ATP. Furthermore, a number of metabolic pathways, such as the Krebs cycle and the urea cycle involve reactions taking place inside the mitochondrion. All the substrates to these pathways, as well as ATP synthesized inside the mitochondrion have to be translocated between the mitochondrial matrix and the cytosol. While the outer mitochondrial membrane is permeable to small solutes (including small proteins), the inner mitochondrial membrane is impermeable. Members of the mitochondrial carrier family (MCF) catalyze this transport of molecules. Depending on the organism, 35 to 45 different mitochondrial carriers (MC) have been identified, each with its specific substrates. They all share a common sequence motif, molecular weights in the range 30-35kDa and are believed to have identical overall fold.[12] Their primary sequence consists of three repeated homologous domains of about 100 residues. The substrates that are translocated by MCs greatly vary in size and structure, ranging from small ions such as phosphate, to NAD+ and coenzyme A. The translocation of substrate from the intermembrane space to the matrix and from the matrix to the intermembrane space proceeds as a 1:1 exchange for most MCs (antiport), although unidirectional transport and co-transport with H+ have also been reported.[12b, 13] In the ADP/ATP carrier (AAC), which is the best-characterized MC[12b], the translocation process occurs on a time scale of milliseconds.[14] Other MCs have been identified and a large body of experimental data about substrate specificity, inhibition and exchange characteristics of the different mitochondrial carriers has been collected, particularly by reconstitution of mitochondrial carriers in liposomes and transport assays[13a, 15].

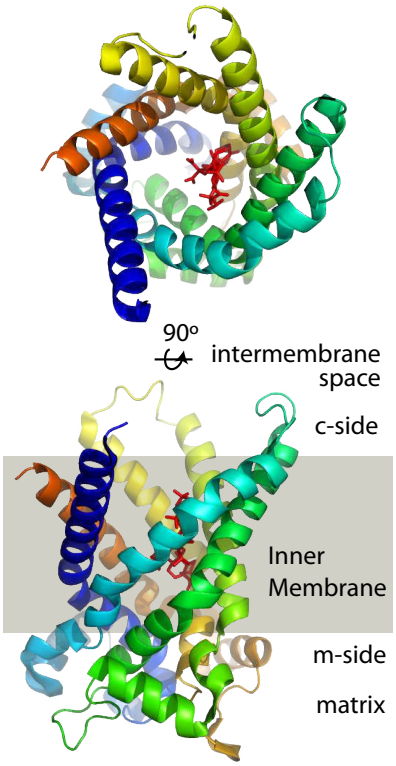

Figure 49. Structure of the ADP/ATP carrier in complex with its inhibitor CATR, as determined from X-ray crystallography (pdb:1OKC).

Atomic-resolution information is available today for only two mitochondrial carriers.[11b, 16] The structure of AAC, locked in its complex with a strong inhibitor (CATR) was solved in 2003 by X-ray crystallography (**Figure 49**).[11b] This structure reveals 6 transmembrane helices and three short helices roughly parallel to the membrane plane, and shows a three-fold pseudo-symmetry. It also features a large cavity that is accessible from the cytosolic side and that is occupied by the inhibitor CATR. A salt bridge network closes the matrix side of the carrier. This conformation is believed to correspond to one extreme conformation ("c-state" or cytosolic state) of the carrier along its functional cycle. Furthermore, it is also thought that the other members of the MCF all share the same overall fold, an assumption that is corroborated by a recent solution-NMR derived structure of UCP2, another mitochondrial carrier.

Many mechanistic questions about substrate translocation remain. In view of the available structures, it is clear that substrate translocation requires large conformational rearrangement. After substrate binding from the cytosolic side of the MC, conformational rearrangements in the MC occur until a transition state is reached, in which a maximum of substrate-protein interactions take place[12b, 17]. Productive translocation is achieved if the carrier undergoes further rearrangement, leading to the complete disruption of the salt bridge network on the matrix side, and opening of the channel towards the matrix side. Direct experimental data about this process lack, however. An experimental demonstration of any intermediate states along this mechanistic pathway, or the experimental demonstration of dynamics that connect different states would be extremely helpful to really understand the mechanism of translocation, and to refine this model. That dynamics measurements have to be in the center of such efforts is also highlighted by a particularly interesting finding: several disease-related mutations of MCs are located in regions of the protein that are not exposed to substrate, but, e.g. point towards the lipid environment.[18] The loss of function of these mutations is thought to be due to a decreased flexibility of the protein, rather than a change in substrate interaction. This hypothesis still awaits experimental investigation.
I will focus in this project on the human mitochondrial ornithine carrier, ORC1, a member of the MCF that catalyzes exchange of ornithine, arginine, lysine and citrulline. This choice is based on ORC's role in human disease (hyperammonemia, hyperornithinemia and homocitrullinuria, or HHH syndrome),[18] on its well-defined and narrow substrate specificity and availability of non-

transported inhibitors[19] and the possibility to produce ORC in sufficient quantities, as shown by preliminary results (see Section b. WP2 b.). I want to answer the question how substrate translocation is related to the intrinsic motion of this carrier in particular, and in MCs in general. More specifically I will focus on the following questions:

- Do MCs undergo continuous exchange between different conformations in the presence of substrate, as suggested by the above model? What can we learn about the rate of such exchange, and are there any intermediate states detectable?
- How do different substrates, e.g translocated at different rates, as well as non-translocated inhibitors affect the motion? Do MCs exhibit large-scale amplitude motions even in the absence of substrates?
- How can we understand the impact of disease-related mutations on the function of mitochondrial carriers?

NMR studies of membrane proteins, and particles as large as the thermosome are very challenging, and require multi-technique approaches. The use of both solid-state and solution-state NMR, will be crucial in order to obtain a comprehensive picture of functional motion.

Figure 50 shows solution-state NMR data of human ORC1 in detergent micelles. The spectra show the complexity expected for a 30 kDa helical membrane protein. Nonetheless, triple-resonance assignment spectra of decent quality can be obtained, and assignments are currently underway in solution-state NMR.
Once assignments are available, we aim at probing the dynamics, an in particular the motion on time scales of milliseconds to microseconds. Ideally, we would like to perform such measurements in the solid state, using proteoliposomes. The methodologies outlined in the previous chapters would ideally address motion in physiologically relevant lipid-embedded proteins.
We will use either these solid-state experiments, or solution-state CPMG methodologies to probe low-populated conformational states in ORC1. Do such states, if existing, correspond to the transition state of transport? At which rates do these states interconvert? Is the inherent function of the protein, rooted in a dynamic interconversion between states, already present without substrate, similar to the motion underlying enzyme kinetics[42]? Quantitative fits of the data will allow to get insight into these questions, and monitor the conformation in the minor states as probed locally by individual nuclei.
We then want to observe changes in dynamics when substrate or inhibitors are present. Do substrates activate the carrier, and result in a higher population of minor conformations or altered exchange kinetics? Likewise, how do inhibitors impact the conformational equilibria and dynamics? We want to answer these questions by performing experiments identical to the ones above on ORC1 samples containing known inhibitors (spermine, spermidine) and substrate which have been shown to be transported in liposomes (L-ornithine, L-lysine, L-arginine).[19]

We will then measure dynamics parameters also for the case of disease-related mutants. Of particular interest will be T32R and P126R, belonging to the MC recognition motif, rather than the proposed substrate-binding region. These sites are thought to provide the hinges around which the kinked helices may alternate from the c-state to the m-state of the carrier. We want to probe whether the inherent dynamics in these mutant carriers are reduced relative to the wild type. A direct evidence for reduced dynamics induced by mutations would provide a direct mechanistic insight into diseases related to membrane translocation.

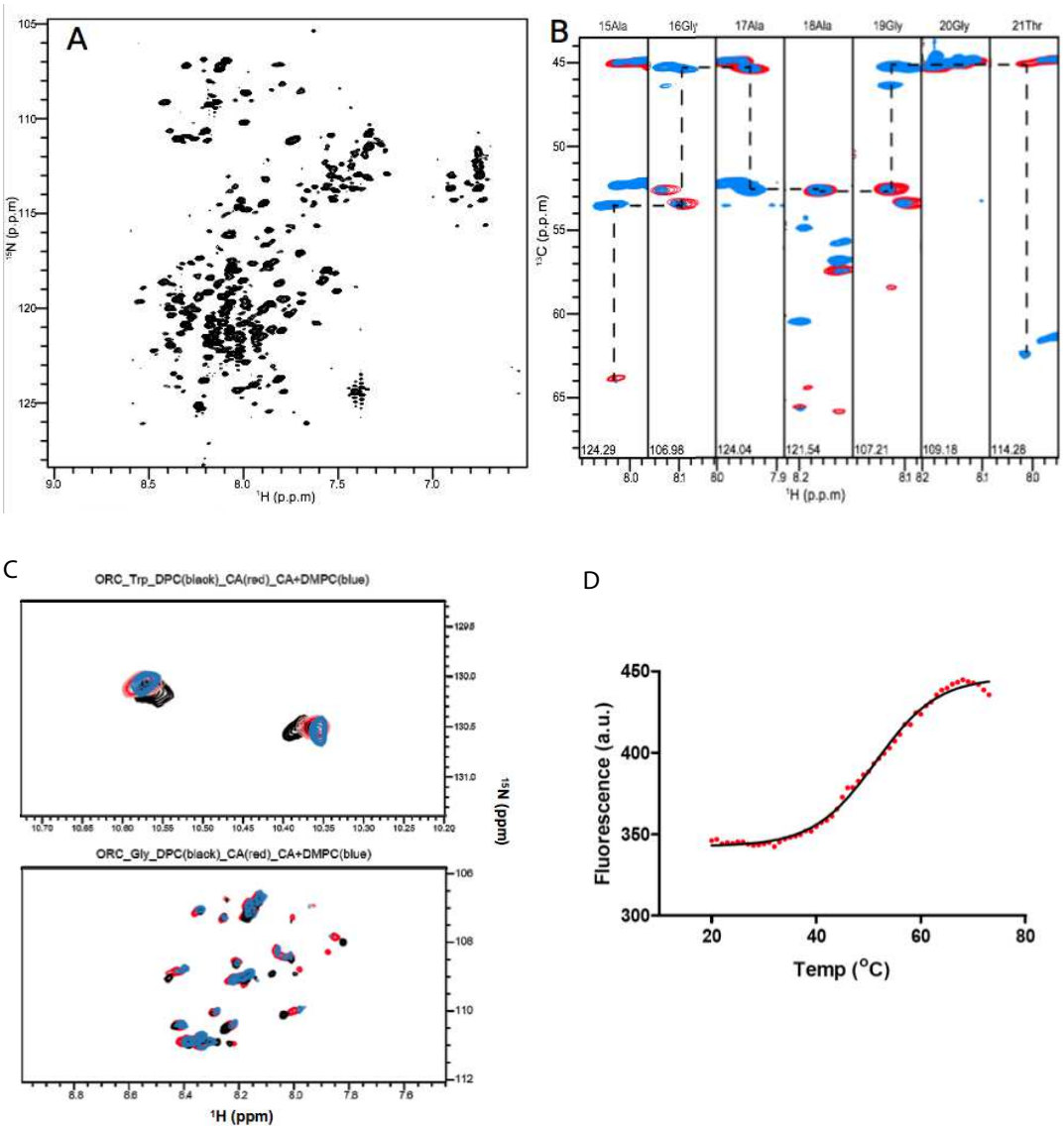

Figure 50. Solution-state NMR results, and thermal-shift assay data of human ORC1.

References

1. de Bakker, P., Furnham, N., Blundell, T. & DePristo, M. Conformer generation under restraints. *Curr Opin Struct Biol* **16,** 160–165 (2006).
2. Lang, P. T., Holton, J. M., Fraser, J. S. & Alber, T. Protein structural ensembles are revealed by redefining X-ray electron density noise. *P Natl Acad Sci Usa* **111,** 237–242 (2014).
3. Fraser, J. S. *et al*. Hidden alternative structures of proline isomerase essential for catalysis. *Nature* **462,** 669–673 (2009).
4. Bourgeois, D. & Royant, A. Advances in kinetic protein crystallography. *Curr Opin Struct Biol* **15,** 538–547 (2005).
5. Buchli, B. *et al*. Kinetic response of a photoperturbed allosteric protein. *P Natl Acad Sci Usa* (2013). doi:10.1073/pnas.1306323110
6. Frederick, K. K., Marlow, M. S., Valentine, K. G. & Wand, A. J. Conformational entropy in molecular recognition by proteins. *Nature* **448,** 325–329 (2007).
7. Henzler-Wildman, K. *et al*. Intrinsic motions along an enzymatic reaction trajectory. *Nature* **450,** 838–U13 (2007).
8. Morrison, E. A. *et al*. Antiparallel EmrE exports drugs by exchanging between asymmetric structures. *Nature* 1–8 (2011). doi:10.1038/nature10703
9. Bruschweiler, S. *et al*. Direct Observation of the Dynamic Process Underlying Allosteric Signal Transmission. *J Am Chem Soc* **131,** 3063–3068 (2009).
10. Goldbourt, A. Biomolecular magic-angle spinning solid-state NMR: recent methods and applications. *Current Opinion in Biotechnology* **24,** 705–715 (2013).
11. Renault, M., Cukkemane, A. & Baldus, M. Solid-state NMR spectroscopy on complex biomolecules. *Angewandte Chemie (International ed in English)* **49,** 8346–8357 (2010).
12. Lewandowski, J. R. Advances in Solid-State Relaxation Methodology for Probing Site-Specific Protein Dynamics. *Accounts of Chemical Research* 130426105512004 (2013). doi:10.1021/ar300334g
13. Hologne, M., Chevelkov, V. & Reif, B. Deuterated peptides and proteins in MAS solid-state NMR. *Prog Nucl Mag Res Sp* **48,** 211–232 (2006).
14. Krushelnitsky, A. & Reichert, D. Solid-state NMR and protein dynamics. *Prog Nucl Mag Res Sp* **47,** 1–25 (2005).
15. Krushelnitsky, A., Reichert, D. & Saalwächter, K. Solid-State NMR Approaches to Internal Dynamics of Proteins: From Picoseconds to Microseconds and Seconds. *Accounts of Chemical Research* **46,** 2028–2036 (2013).
16. Schanda, P., Meier, B. H. & Ernst, M. Quantitative analysis of protein backbone dynamics in microcrystalline ubiquitin by solid-state NMR spectroscopy. *J Am Chem Soc* **132,** 15957–15967 (2010).
17. Redfield, A. G. On the theory of relaxation processes. *IBM J. Res. Devel.* **1,** 19–31 (1957).
18. Cavanagh, J., Fairbrother, W., Palmer, A. G. & Skelton, N. *Protein NMR spectroscopy: Principles and practice. Protein NMR spectroscopy: Principles and practice* (1996).
19. Chevelkov, V. *et al*. Differential line broadening in MAS solid-state NMR due to dynamic interference. *J Am Chem Soc* **129,** 10195–10200 (2007).
20. Lewandowski, J. R., Sass, H. J., Grzesiek, S., Blackledge, M. & Emsley, L. Site-specific measurement of slow motions in proteins. *J Am Chem Soc* **133,** 16762–16765 (2011).
21. Korzhnev, D., Religa, T., Banachewicz, W., Fersht, A. & Kay, L. A Transient and Low-Populated Protein-Folding Intermediate at Atomic Resolution. *Science* **329,** 1312–1316 (2010).
22. Religa, T. L., Sprangers, R. & Kay, L. E. Dynamic Regulation of Archaeal Proteasome Gate Opening As Studied by TROSY NMR. *Science* **328,** 98–102 (2010).
23. Tzeng, S. & Kalodimos, C. Dynamic activation of an allosteric regulatory protein. *Nature* **462,** 368–U139 (2009).
24. Paulson, E. *et al*. Sensitive high resolution inverse detection NMR spectroscopy of proteins in the solid state. *J Am Chem Soc* **125,** 15831–15836 (2003).
25. Zhou, D. *et al*. Solid-state protein-structure determination with proton-detected triple-resonance 3D magic-angle-spinning NMR spectroscopy. *Angew Chem Int. Ed. Engl.* **46,** 8380–8383 (2007).
26. Chevelkov, V. *et al*. 1H detection in MAS solid-state NMR spectroscopy of biomacromolecules employing pulsed field gradients for residual solvent suppression. *J Am Chem Soc* **125,** 7788–7789 (2003).
27. Ward, M. E. *et al*. Proton-detected solid-state NMR reveals intramembrane polar networks in a seven-helical transmembrane protein proteorhodopsin. *J Am Chem Soc* **133,** 17434–17443 (2011).
28. Linser, R. *et al*. Proton-detected solid-state NMR spectroscopy of fibrillar and membrane proteins. *Angew Chem Int. Ed. Engl.* **50,** 4508–4512 (2011).
29. Barbet-Massin, E. *et al*. Rapid Proton-Detected NMR Assignment for Proteins with Fast Magic Angle Spinning. *J Am Chem Soc* (2014). doi:10.1021/ja507382j
30. Reif, B. Ultra-high resolution in MAS solid-state NMR of perdeuterated proteins: implications for structure and dynamics. *J Magn Reson* **216,** 1–12 (2012).

31. Asami, S. & Reif, B. Proton-Detected Solid-State NMR Spectroscopy at Aliphatic Sites: Application to Crystalline Systems. *Accounts of Chemical Research* 130607095515005 (2013). doi:10.1021/ar400063y
32. Chevelkov, V., Rehbein, K., Diehl, A. & Reif, B. Ultrahigh resolution in proton solid-state NMR spectroscopy at high levels of deuteration. *Angew Chem Int. Ed. Engl.* **45,** 3878–3881 (2006).
33. Chen, L. *et al*. J-based 2D homonuclear and heteronuclear correlation in solid-state proteins. *Magn Reson Chem* **45,** S84–S92 (2008).
34. Schanda, P., Huber, M., Verel, R., Ernst, M. & Meier, B. H. Direct detection of (3h)J(NC') hydrogen-bond scalar couplings in proteins by solid-state NMR spectroscopy. *Angew Chem Int. Ed. Engl.* **48,** 9322–9325 (2009).
35. Linser, R., Fink, U. & Reif, B. Proton-detected scalar coupling based assignment strategies in MAS solid-state NMR spectroscopy applied to perdeuterated proteins. *J Magn Reson* **193,** 89–93 (2008).
36. Lange, A., Luca, S. & Baldus, M. Structural constraints from proton-mediated rare-spin correlation spectroscopy in rotating solids. *J Am Chem Soc* **124,** 9704–9705 (2002).
37. Linser, R., Bardiaux, B., Higman, V., Fink, U. & Reif, B. Structure calculation from unambiguous long-range amide and methyl 1H-1H distance restraints for a microcrystalline protein with MAS solid-state NMR spectroscopy. *J Am Chem Soc* **133,** 5905–5912 (2011).
38. Huber, M. *et al*. A Proton-Detected 4D Solid-State NMR Experiment for Protein Structure Determination. *ChemPhysChem* **12,** 915–918 (2011).
39. Chou, J., Case, D. & Bax, A. Insights into the mobility of methyl-bearing side chains in proteins from (3)J(CC) and (3)J(CN) couplings. *J Am Chem Soc* **125,** 8959–8966 (2003).
40. Schanda, P., Huber, M., Boisbouvier, J., Meier, B. H. & Ernst, M. Solid-State NMR Measurements of Asymmetric Dipolar Couplings Provide Insight into Protein Side-Chain Motion. *Angew Chem Int. Ed. Engl.* **50,** 11005–11009 (2011).
41. Yang, J., Tasayco, M. & Polenova, T. Dynamics of Reassembled Thioredoxin Studied by Magic Angle Spinning NMR: Snapshots from Different Time Scales. *J Am Chem Soc* **131,** 13690–13702 (2009).
42. Chevelkov, V., Fink, U. & Reif, B. Quantitative analysis of backbone motion in proteins using MAS solid-state NMR spectroscopy. *J Biomol NMR* **45,** 197–206 (2009).
43. Chevelkov, V., Fink, U. & Reif, B. Accurate Determination of Order Parameters from H-1,N-15 Dipolar Couplings in MAS Solid-State NMR Experiments. *J Am Chem Soc* **131,** 14018–14022 (2009).
44. Lewandowski, J. R., Sein, J., Blackledge, M. & Emsley, L. Anisotropic Collective Motion Contributes to Nuclear Spin Relaxation in Crystalline Proteins. *J Am Chem Soc* **132,** 1246–1248 (2010).
45. Chevelkov, V. & Reif, B. TROSY effects in MAS solid-state NMR. *Concepts in Magnetic Resonance Part A* **32A,** 143–156 (2008).
46. Mollica, L. *et al*. Atomic-Resolution Structural Dynamics in Crystalline Proteins from NMR and Molecular Simulation. *The journal of physical chemistry letters* 3657–3662 (2012). doi:10.1021/jz3016233
47. Schanda, P., Meier, B. H. & Ernst, M. Accurate measurement of one-bond H-X heteronuclear dipolar couplings in MAS solid-state NMR. *J Magn Reson* **210,** 246–259 (2011).
48. Lipari, G. & Szabo, A. Model-Free Approach to the Interpretation of Nuclear Magnetic-Resonance Relaxation in Macromolecules .1. Theory and Range of Validity. *J Am Chem Soc* **104,** 4546–4559 (1982).
49. Clore, G. M. *et al*. Deviations from the simple two-parameter model-free approach to the interpretation of nitrogen-15 nuclear magnetic relaxation of proteins. *J Am Chem Soc* **112,** 4989–4991 (1990).
50. Lewandowski, J. R. *et al*. Measurement of site-specific 13C spin-lattice relaxation in a crystalline protein. *J Am Chem Soc* **132,** 8252–8254 (2010).
51. Chevelkov, V., Xue, Y., Linser, R., Skrynnikov, N. R. & Reif, B. Comparison of Solid-State Dipolar Couplings and Solution Relaxation Data Provides Insight into Protein Backbone Dynamics. *J Am Chem Soc* **132,** 5015–5017 (2010).
52. Lienin, S., Bremi, T., Brutscher, B., Bruschweiler, R. & Ernst, R. Anisotropic intramolecular backbone dynamics of ubiquitin characterized by NMR relaxation and MD computer simulation. *J Am Chem Soc* **120,** 9870–9879 (1998).
53. Salmon, L. *et al*. Protein Conformational Flexibility from Structure-Free Analysis of NMR Dipolar Couplings: Quantitative and Absolute Determination of Backbone Motion in Ubiquitin. *Angew Chem Int. Ed. Engl.* **48,** 4154–4157 (2009).
54. Lakomek, N. *et al*. Self-consistent residual dipolar coupling based model-free analysis for the robust determination of nanosecond to microsecond protein dynamics. *J Biomol NMR* **41,** 139–155 (2008).
55. Ban, D. *et al*. Kinetics of conformational sampling in ubiquitin. *Angewandte Chemie (International ed in English)* **50,** 11437–11440 (2011).
56. Hohwy, M., Jaroniec, C., Reif, B., Rienstra, C. & Griffin, R. Local structure and relaxation in solid-state NMR: Accurate measurement of amide N-H bond lengths and H-N-H bond angles. *J Am Chem Soc* **122,** 3218–3219 (2000).
57. Helmus, J., Surewicz, K., Surewicz, W. & Jaroniec, C. Conformational flexibility of Y154Stop human prion protein amyloid fibrils probed by solid-state nuclear magnetic resonance spectroscopy. *J Am Chem Soc* **132,** 2393–2403 (2010).
58. Levitt, M. Symmetry-based pulse sequences in magic-angle spinning solid-state NMR. *Encyclopedia of Nuclear Magnetic Resonance* **9,** 165–196 (2002).

59. Dvinskikh, S., Zimmermann, H., Maliniak, A. & Sandstrom, D. Heteronuclear dipolar recoupling in liquid crystals and solids by PISEMA-type pulse sequences. *J Magn Reson* **164,** 165–170 (2003).
60. Knight, M. J. *et al*. Structure and backbone dynamics of a microcrystalline metalloprotein by solid-state NMR. *P Natl Acad Sci Usa* (2012). doi:10.1073/pnas.1204515109
61. Agarwal, V., Xue, Y., Reif, B. & Skrynnikov, N. Protein Side-Chain Dynamics As Observed by Solution- and Solid-State NMR Spectroscopy: A Similarity Revealed. *J Am Chem Soc* **130,** 16611–16621 (2008).
62. Asami, S., Schmieder, P. & Reif, B. High resolution 1H-detected solid-state NMR spectroscopy of protein aliphatic resonances: access to tertiary structure information. *J Am Chem Soc* **132,** 15133–15135 (2010).
63. Boehr, D., McElheny, D., Dyson, H. & Wright, P. The dynamic energy landscape of dihydrofolate reductase catalysis. *Science* **313,** 1638–1642 (2006).
64. Palmer, A. G. NMR characterization of the dynamics of biomacromolecules. *Chem Rev* **104,** 3623–3640 (2004).
65. Mittermaier, A. K. & Kay, L. E. Observing biological dynamics at atomic resolution using NMR. *Trends in Biochemical Sciences* **34,** 601–611 (2009).
66. Neudecker, P., Lundstrom, P. & Kay, L. E. Relaxation Dispersion NMR Spectroscopy as a Tool for Detailed Studies of Protein Folding. *Biophys J* **96,** 2045–2054 (2009).
67. Palmer, A. G. & Massi, F. Characterization of the dynamics of biomacromolecules using rotating-frame spin relaxation NMR spectroscopy. *Chem Rev* **106,** 1700–1719 (2006).
68. Kloiber, K. & Konrat, R. Differential multiple-quantum relaxation arising from cross-correlated time-modulation of isotropic chemical shifts. *J Biomol NMR* **18,** 33–42 (2000).
69. Salvi, N., Ulzega, S., Ferrage, F. & Bodenhausen, G. Time scales of slow motions in ubiquitin explored by heteronuclear double resonance. *J Am Chem Soc* **134,** 2481–2484 (2012).
70. Früh, D., Tolman, J. R., Bodenhausen, G. & Zwahlen, C. Cross-correlated chemical shift modulation: a signature of slow internal motions in proteins. *J Am Chem Soc* **123,** 4810–4816 (2001).
71. Andronesi, O. C. *et al*. Determination of membrane protein structure and dynamics by magic-angle-spinning solid-state NMR spectroscopy. *J Am Chem Soc* **127,** 12965–12974 (2005).
72. Byeon, I.-J. L. *et al*. Motions on the Millisecond Time Scale and Multiple Conformations of HIV-1 Capsid Protein: Implications for Structural Polymorphism of CA Assemblies. *J Am Chem Soc* **134,** 6455–6466 (2012).
73. Lorieau, J. L., Day, L. A. & McDermott, A. E. Conformational dynamics of an intact virus: order parameters for the coat protein of Pf1 bacteriophage. *P Natl Acad Sci Usa* **105,** 10366–10371 (2008).
74. Lange, A. *et al*. A combined solid-state NMR and MD characterization of the stability and dynamics of the HET-s(218-289) prion in its amyloid conformation. *ChemBioChem* **10,** 1657–1665 (2009).
75. Giraud, N. *et al*. Quantitative analysis of backbone dynamics in a crystalline protein from nitrogen-15 spin-lattice relaxation. *J Am Chem Soc* **127,** 18190–18201 (2005).
76. Torchia, D. A. Dynamics of biomolecules from picoseconds to seconds at atomic resolution. *J Magn Reson* **212,** 1–10 (2011).
77. Palmer, A. G., Williams, J. & McDermott, A. Nuclear magnetic resonance studies of biopolymer dynamics. *J. Phys. Chem* **100,** 13293–13310 (1996).
78. Krushelnitsky, A. *et al*. Direct Observation of Millisecond to Second Motions in Proteins by Dipolar CODEX NMR Spectroscopy. *J Am Chem Soc* **131,** 12097–12099 (2009).
79. Lewandowski, J. R. *et al*. Enhanced Resolution and Coherence Lifetimes in the Solid-state NMR Spectroscopy of Perdeuterated Proteins under Ultrafast Magic-angle Spinning. *J. Phys. Chem. Lett.* **2,** 2205–2211 (2011).
80. Frueh, D. Internal motions in proteins and interference effects in nuclear magnetic resonance. *Prog Nucl Mag Res Sp* **41,** 305–324 (2002).
81. Wist, J., Frueh, D., Tolman, J. R. & Bodenhausen, G. Triple quantum decoherence under multiple refocusing: slow correlated chemical shift modulations of C' and N nuclei in proteins. *J Biomol NMR* **28,** 263–272 (2004).
82. Dittmer, J. & Bodenhausen, G. Evidence for slow motion in proteins by multiple refocusing of heteronuclear nitrogen/proton multiple quantum coherences in NMR. *J Am Chem Soc* **126,** 1314–1315 (2004).
83. Wang, C. & Palmer, A. Differential multiple quantum relaxation caused by chemical exchange outside the fast exchange limit. *J Biomol NMR* **24,** 263–268 (2002).
84. Skrynnikov, N. Asymmetric doublets in MAS NMR: coherent and incoherent mechanisms. *Magn Reson Chem* **45,** S161–S173 (2007).
85. Verde, M., Ulzega, S., Ferrage, F. & Bodenhausen, G. Preservation of heteronuclear multiple-quantum coherences in NMR by double-resonance irradiation. *J Chem Phys* **130,** 074506 (2009).
86. Korzhnev, D. M., Kloiber, K. & Kay, L. E. Multiple-quantum relaxation dispersion NMR spectroscopy probing millisecond time-scale dynamics in proteins: theory and application. *J Am Chem Soc* **126,** 7320–7329 (2004).
87. Loria, J., Rance, M. & Palmer, A. A relaxation-compensated Carr-Purcell-Meiboom-Gill sequence for characterizing chemical exchange by NMR spectroscopy. *J Am Chem Soc* **121,** 2331–2332 (1999).
88. Hansen, D. F., Vallurupalli, P. & Kay, L. E. An improved N-15 relaxation dispersion experiment for the measurement of millisecond time-scale dynamics in proteins. *J Phys Chem B* **112,** 5898–5904 (2008).
89. Tollinger, M., Skrynnikov, N., Mulder, F., Forman-Kay, J. & Kay, L. Slow dynamics in folded and unfolded

states of an SH3 domain. *J Am Chem Soc* **123,** 11341–11352 (2001).
90. Millet, O., Loria, J., Kroenke, C., Pons, M. & Palmer, A. The static magnetic field dependence of chemical exchange linebroadening defines the NMR chemical shift time scale. *J Am Chem Soc* **122,** 2867–2877 (2000).
91. Tollinger, M., Sivertsen, A. C., Meier, B. H., Ernst, M. & Schanda, P. Site-Resolved Measurement of Microsecond-to-Millisecond Conformational-Exchange Processes in Proteins by Solid-State NMR Spectroscopy. *J Am Chem Soc* **134,** 14800–14807 (2012).
92. Lorieau, J. & McDermott, A. Conformational flexibility of a microcrystalline globular protein: Order parameters by solid-state NMR spectroscopy. *J Am Chem Soc* **128,** 11505–11512 (2006).
93. Majumdar, A. & Ghose, R. Probing slow backbone dynamics in proteins using TROSY-based experiments to detect cross-correlated time-modulation of isotropic chemical shifts. *J Biomol NMR* **28,** 213–227 (2004).
94. Hansen, D. F., Feng, H., Zhou, Z., Bai, Y. & Kay, L. E. Selective characterization of microsecond motions in proteins by NMR relaxation. *J Am Chem Soc* **131,** 16257–16265 (2009).
95. Massi, F., Grey, M. & Palmer, A. G. Microsecond timescale backbone conformational dynamics in ubiquitin studied with NMR R-1p relaxation experiments. *Protein Sci* **14,** 735–742 (2005).
96. Mills, J. L. & Szyperski, T. Protein dynamics in supercooled water: the search for slow motional modes. *J Biomol NMR* **23,** 63–67 (2002).
97. Sidhu, A., Surolia, A., Robertson, A. D. & Sundd, M. A hydrogen bond regulates slow motions in ubiquitin by modulating a β-turn flip. *J Mol Biol* **411,** 1037–1048 (2011).
98. Huang, K.-Y., Amodeo, G. A., Tong, L. & McDermott, A. The structure of human ubiquitin in 2-methyl-2,4-pentanediol: a new conformational switch. *Protein Sci* **20,** 630–639 (2011).
99. Cornilescu, G., Marquardt, J. L., Ottiger, M. & Bax, A. Validation of protein structure from anisotropic carbonyl chemical shifts in a dilute liquid crystalline phase. *J Am Chem Soc* **120,** 6836–6837 (1998).
100. Krushelnitsky, A., Zinkevich, T., Reichert, D., Chevelkov, V. & Reif, B. Microsecond Time Scale Mobility in a Solid Protein As Studied by the 15N R1ϱSite-Specific NMR Relaxation Rates. *J Am Chem Soc* **132,** 11850–11853 (2010).
101. Korzhnev, D. & Kay, L. Probing invisible, low-populated states of protein molecules by relaxation dispersion NMR spectroscopy: An application to protein folding. *Acc. Chem. Res.* **41,** 442–451 (2008).
102. Neudecker, P. *et al*. Structure of an intermediate state in protein folding and aggregation. *Science* **336,** 362–366 (2012).
103. Bouvignies, G. *et al*. Solution structure of a minor and transiently formed state of a T4 lysozyme mutant. *Nature* **477,** 111–114 (2011).
104. McConnell, H. M. REACTION RATES BY NUCLEAR MAGNETIC RESONANCE. *J Chem Phys* **28,** 430–431 (1958).
105. Quinn, C. & McDermott, A. Monitoring conformational dynamics with solid-state R (1 rho) experiments. *J Biomol NMR* **45,** 5–8 (2009).
106. Quinn, C. M. & McDermott, A. E. Quantifying conformational dynamics using solid-state $R_1\varrho$ experiments. *J Magn Reson* **222,** 1–7 (2012).
107. Gan, Z.-H. & Grant, D. M. Rotational resonance in a spin-lock field for solid state NMR. *Chem Phys Lett* **168,** 304–308 (1990).
108. Kurbanov, R., Zinkevich, T. & Krushelnitsky, A. The nuclear magnetic resonance relaxation data analysis in solids: General R(1)*/*R(1) (ϱ) equations and the model-free approach. *J Chem Phys* **135,** 184104 (2011).
109. Gan, Z., Grant, D. M. & Ernst, R. R. NMR chemical shift anisotropy measurements by RF driven rotary resonance. *Chem Phys Lett* **254,** 349–357 (1996).
110. Silver, L. L. Viable screening targets related to the bacterial cell wall. *Ann. N. Y. Acad. Sci.* **1277,** 29–53 (2013).
111. Matteï, P. J., Neves, D. & Dessen, A. Bridging cell wall biosynthesis and bacterial morphogenesis. *Curr Opin Struct Biol* (2010).
112. Mainardi, J.-L. *et al*. Unexpected inhibition of peptidoglycan LD-transpeptidase from Enterococcus faecium by the beta-lactam imipenem. *J Biol Chem* **282,** 30414–30422 (2007).
113. Lavollay, M. *et al*. The peptidoglycan of stationary-phase Mycobacterium tuberculosis predominantly contains cross-links generated by L,D-transpeptidation. *J Bacteriol* **190,** 4360–4366 (2008).
114. Magnet, S. *et al*. Specificity of L,D-transpeptidases from gram-positive bacteria producing different peptidoglycan chemotypes. *J Biol Chem* **282,** 13151–13159 (2007).
115. Lecoq, L. *et al*. Dynamics Induced by beta-Lactam Antibiotics in the Active Site of Bacillus subtilis L,D-Transpeptidase. *Structure/Folding and Design* **20,** 850–861 (2012).
116. Bielnicki, J. *et al*. B. subtilis ykuD protein at 2.0 A resolution: insights into the structure and function of a novel, ubiquitous family of bacterial enzymes. *Proteins-Structure Function and Bioinformatics* **62,** 144–151 (2006).
117. Biarrotte-Sorin, S. *et al*. Crystal Structure of a Novel β-Lactam-insensitive Peptidoglycan Transpeptidase. *J Mol Biol* **359,** 533–538 (2006).
118. Kim, H. S. *et al*. Structural basis for the inhibition of Mycobacterium tuberculosis L,D-transpeptidase by meropenem, a drug effective against extensively drug-resistant strains. *Acta Crystallographica Section D-Biological Crystallography* **69,** 420–431 (2013).
119. Correale, S., Ruggiero, A., Capparelli, R., Pedone, E. & Berisio, R. Structures of free and inhibited forms of

the L,D-transpeptidase LdtMt1 from Mycobacterium tuberculosis. *Acta Crystallographica Section D-Biological Crystallography* **69,** 1697–1706 (2013).
120. Böth, D. *et al*. Structure of LdtMt2, an L,D-transpeptidase from Mycobacterium tuberculosis. *Acta Crystallographica Section D-Biological Crystallography* **69,** 432–441 (2013).
121. Buist, G., Steen, A., Kok, J. & Kuipers, O. P. LysM, a widely distributed protein motif for binding to (peptido)glycans. *Molecular microbiology* **68,** 838–847 (2008).
122. Garvey, K. J., Saedi, M. S. & Ito, J. Nucleotide sequence of Bacillus phage phi 29 genes 14 and 15: homology of gene 15 with other phage lysozymes. *Nucleic Acids Research* **14,** 10001–10008 (1986).
123. Bateman, A. & Bycroft, M. The structure of a LysM domain from E. coli membrane-bound lytic murein transglycosylase D (MltD). *J Mol Biol* **299,** 1113–1119 (2000).
124. Siewering, K. *et al*. Peptidoglycan-binding protein TsaP functions in surface assembly of type IV pili. *P Natl Acad Sci Usa* **111,** E953–61 (2014).
125. Kern, T. *et al*. Dynamics Characterization of Fully Hydrated Bacterial Cell Walls by Solid-State NMR: Evidence for Cooperative Binding of Metal Ions. *J Am Chem Soc* **132,** 10911–10919 (2010).
126. Lehotzky, R. E. *et al*. Molecular basis for peptidoglycan recognition by a bactericidal lectin. *P Natl Acad Sci Usa* **107,** 7722–7727 (2010).
127. Kulminskaya, N. V. *et al*. In Situ Solid-State NMR Spectroscopy of Protein in Heterogeneous Membranes: The Baseplate Antenna Complex of Chlorobaculum tepidum. *Angew Chem Int Edit* **51,** 6891–6895 (2012).
128. Takahashi, H. *et al*. Solid-State NMR on Bacterial Cells: Selective Cell-Wall-Signal Enhancement and Resolution Improvement using Dynamic Nuclear Polarization. *J Am Chem Soc* 130130133309007 (2013). doi:10.1021/ja312501d
129. Kern, T. *et al*. Toward the Characterization of Peptidoglycan Structure and Protein–Peptidoglycan Interactions by Solid-State NMR Spectroscopy. *J Am Chem Soc* **130,** 5618–5619 (2008).
130. Gansmüller, A., Simorre, J.-P. & Hediger, S. Windowed R-PDLF recoupling: A flexible and reliable tool to characterize molecular dynamics. *J Magn Reson* **234,** 154–164 (2013).
131. Franks, W. *et al*. Magic-angle spinning solid-state NMR spectroscopy of the beta 1 immunoglobulin binding domain of protein G (GB1): N-15 and C-13 chemical shift assignments and conformational analysis. *J Am Chem Soc* **127,** 12291–12305 (2005).
132. Laguri, C. *et al*. 13C-labeled heparan sulfate analogue as a tool to study protein/heparan sulfate interaction by NMR spectroscopy. Application to the CXCL12 chemokine. *J Am Chem Soc* (2011).
133. Mesnage, S. *et al*. Molecular basis for bacterial peptidoglycan recognition by LysM domains. *Nature Communications* **5,** 4269 (2014).

Curriculum Vitae

Paul SCHANDA
Feb. 6, 1979 (35 years old)
Austrian citizen, married, two children

Education and Diploma

2007	**Ph. D. in Physics**, University J. Fourier Grenoble, France
2004	**M. Sc. in Chemistry**, with distinction, University of Vienna, Austria
1997-1999, 2000-2004	Studies of **Chemistry**, University of Vienna, Austria. (Civil service at Red Cross Vienna interrupted studies for one year 1999-2000.)

Research Experience

04/2013 – present	Research group leader at the **Institut de Biologie Structural Grenoble**, France. Funded by a 5-year "Starting Grant" by the European Research Council (ERC). Currently 5 group members. Permanent position at French National Research Institution "CEA".
12/2010 - present	Junior group leader solid-state NMR at the **Institut de Biologie Structurale Grenoble**, funded by grant from French National Research Agency (ANR – Retour-PostDoc).
02/2008-11/2010	Post-doctoral fellow, laboratory of Prof. B. H. Meier, **ETH Zürich**, Switzerland. **Methodological developments** and applications of **solid-state NMR** spectroscopy.
10/2005-12/2005	Visiting scientist in the group of Prof. L. Frydman, **Weizmann Institute of Science**, Israel. **Development of ultrafast NMR** for the study of kinetics in proteins.
10/2004-10/2007	Ph. D. studies under the supervision of Dr. B. Brutscher, **IBS Grenoble**, France. Development of **fast multidimensional solution-state NMR** and application to **protein kinetics and folding** studies.
02/2004-07/2004	Researcher on contract in the laboratory of Prof. R. Konrat, **University of Vienna**, Austria. NMR spectroscopic characterization of **protein interactions and dynamics.**
03/2003-03/2004	M. Sc. work in the laboratory of Prof. R. Konrat, University of Vienna, Austria. Protein dynamics in solution state by NMR.
02/2002-06/2002	Research internship in **bio-inorganic chemistry** in the group of Dr. J.M. Latour, CEA Grenoble, France. Physico-chemical characterization and synthesis of bio-mimetic iron complexes.

Professional Experience in Industry

7/2002-9/2002	Internship at Fluka (Sigma-Aldrich) in Buchs, Switzerland Analytical Chemistry (Trace Analysis with ICP-OES/ICP-MS. Quality control of research chemicals)
7/2001-9/2001	Internship at Sandoz - Biochemie Kundl, Austria Analytical Chemistry (Gas Chromatography. Quality control of antibiotics)

International collaborations

- Hartmut Oschkinat (FMP): Solid-state NMR methods, 1 publication.
- Lucio Frydman (Weizmann Institute, Israel): Development of fast NMR methods. 3 publications.
- Martin Tollinger (Univ.Vienna & Univ. Innsbruck, Austria): Protein dynamics: 2 publications + 1 subm.
- Alessandra Corazza (Univ. Udine, Italy): Protein folding, 1 publication.
- Michele Parrinello (ETH Zürich Lugano, Computational science): Protein dynamics simulations.
- Vincent Forge (CEA Grenoble, France): Protein folding & amyloid formation: 3 publications.
- Nikolai Skrynnikov (Purdue Universitiy): Protein dynamics and MD simulations.

Prizes, Grants and Awards:

- **ERC Starting Grant 2012**: 1.5M€ "Starting Grant" for 5 year (2013-2018).
- **Re-Integration grant** ANR Retour-PostDoc, (2010-2013)
  Total budget 495k€. Including 2-year salary for Post-doctoral fellow, NMR equipment and consumables.
- **Young Researcher Award** of the **French Biophysical Society** (2010) http://www.sfbiophys.org/
- **Post-doc fellowship „ETH Fellows"**, ETH Zurich (2008),
  http://www.vpf.ethz.ch/services/ETH_Fellows
- **Award for the promotion of outstanding young researchers**, Upper-Austrian regional government (2007)
- **Post-Graduate Grant from the Austrian ministry of Science and Education** (2004)
- **PhD Grant** from the **Boehringer Ingelheim foundation** for basic research (2004) http://bifonds.de/
  Prestigious and competitive PhD grant in life sciences

Languages

German (native), English (fluent), French (fluent)

Scientific publications

Publications summary

• 33 scientific publications: 31 original research articles, 1 review (number 18 below) and 1 book chapter (number 20 below). These publications have been cited >900 times.

• including top journals in chemistry, life sciences and NMR spectroscopy:
2 x *Angew. Chem. Int. Ed.* (Impact Factor 12.7)
1 x *Proc. Natl. Acad. Sci. USA* (IF 9.8)
9 x *J. Am. Chem. Soc.* (IF 9.0)
1 x *Prog. NMR Spectr.* (IF 6.1)
1 x *J. Biol. Chem.* (IF 5.3)
3 x *J. Mol. Biol* (IF 4.0)
and other journals in the field of physical chemistry, biochemistry and spectroscopy

• h-index: 18

Full list of publications

2005

1. Schanda, P., Brutscher, B.
Very fast two dimensional NMR spectroscopy for real-time investigation of dynamic events in proteins on the time scale of seconds. **J. Am. Chem. Soc.,** 127 (22): 8014-5 (2005).

2. Schanda, P ., Kupce, E., Brutscher, B.
SOFAST-HMQC experiments for recording of two-dimensional heteronuclear correlation spectra of proteins within a few seconds. **J. Biomol. NMR**, 33(4): 199-211 (2005).
Papers 1 and 2 describe an important new technique allowing the acquisition of atomic-resolution 2D NMR spectra in very short times. They have been cited over 200 times.

3. Schanda, P., Brutscher, B.
Hadamard frequency-encoded SOFAST HMQC for ultrafast two-dimensional protein NMR. **J. Magn. Reson**, 178(2): 334-9 (2005).

2006

4. Schanda, P., Forge, V., Brutscher, B.
HET-SOFAST NMR for fast detection of structural compactness and heterogeneity along polypeptide chains. **Magn. Reson. Chem**., 44: S177-84 (2006).

5. Schanda, P., Van Melckebeke, H., Brutscher, B.
Speeding up three-dimensional protein NMR experiments to a few minutes. **J. Am. Chem. Soc**., 128(28): 9042-3 (2006).

2007

6. Gal, M., Schanda, P., Brutscher, B., Frydman, L.
UltraSOFAST HMQC NMR and the Repetitive Acquisition of 2D Protein Spectra at Hertz Rates. **J. Am. Chem. Soc.**, 129(5): 1372-7 (2007).
This work combines the SOFAST method I developed with a method set up by Prof. Frydman. M. Gal and I contributed equally to this work during my 3-month visit at Weizmann Institute.

7. Schanda, P., Lescop, E., Falge, M., Sounier, R., Boisbouvier, J., Brutscher, B.
Sensitivity-optimized experiment for the measurement of residual dipolar couplings between amide protons. **J. Biomol. NMR**, 38(1): 47-55 (2007).

8. Lescop, E., Schanda, P., Rasia, R., Brutscher, B.
Automated spectral compression for fast multidimensional NMR and increased timeresolution in real-time NMR. **J. Am. Chem. Soc.**, 129(10): 2756-7 (2007).

9. Lescop, E., Schanda, P., Brutscher, B.
A set of BEST triple-resonance experiments for time-optimized protein resonance assignment. **J. Magn. Reson.**,187(1): 163-9 (2007)

10. Schanda, P., Forge, V., Brutscher, B.
Protein folding and unfolding studied at atomic resolution by fast two-dimensional NMR spectroscopy. **Proc. Natl. Acad. Sci. USA**, 104(27): 11257-62 (2007).
First application of SOFAST-NMR to protein folding. I produced protein, did all experiments and analysis.

2008

11. Kern, T., Schanda, P., Brutscher, B.
Sensitivity-enhanced IPAP-SOFAST-HMQC for fast-pulsing 2D NMR with reduced radiofrequency load. **J. Magn. Reson.**, 190: 333-8 (2008).

12. Bersch, B., Favier, A., Schanda, P., van Aelst, S., Vallaeys, T., Coves, J., Mergeay, J., Wattiez, R.
Molecular structure and metal-binding properties of the periplasmic CopK protein expressed in Cupriavidus metallidurans CH34 during copper challenge. **J. Mol. Biol.** 380(2): 386-403 (2008).

13. Schanda, P ., Brutscher, B., Konrat, R.,Tollinger, M.
Folding of the KIX domain. A detailed study of 15N/13C relaxation dispersion NMR and hydrogen/deuterium exchange. **J. Mol. Biol.** 380(4): 726-41 (2008).
I initiated this collaboration with Dr. Tollinger. Using a combination of my fast-NMR tools with relaxation dispersion we obtained detailed insight into a folding intermediate.

2009

14. Farjon, J., Boisbouvier, J., Schanda, P., Pardi, A., Simorre, J.P., Brutscher, B.
Longitudinal-relaxation-enhanced NMR experiments for the study of nucleic acids in solution. **J. Am. Chem. Soc.** 131(24): 8571-7 (2009).

15. Amero, C., Schanda, P., Dura, M.A., Ayala, I., Marion, D., Franzetti, B., Brutscher, B., Boisbouvier, B.
Fast two-dimensional NMR spectroscopy of high molecular weight protein assemblies. **J. Am. Chem. Soc.** 131(10): 3448-9 (2009).

16. Brüschweiler, S., Schanda, P., Kloiber, K., Brutscher, B., Kontaxis, G., Konrat, R., Tollinger, M.
Direct observation of the dynamic process underlying allosteric signal transmission. **J. Am. Chem. Soc.** 131(8): 3063-68 (2009).
I initiated this research project together with Dr. Tollinger and his PhD student S. Bruschweiler. When this paper was under review in the first journal (Nature), I was co-first author. (For reasons of editorial policy, the J. Am. Chem. Soc., where it got published, did not accept a statement about this equal authorship.)

17. Gal, M., Kern, T., Schanda, P., Frydman, L., Brutscher, B.
An improved ultrafast 2D NMR experiment: Toward atom-resolved real-time studies of protein kinetics at multi-Hz rates. **J. Biomol. NMR.** 43: 1-10 (2009).

18. Schanda, P.
Fast-pulsing longitudinal relaxation optimized techniques: Enriching the toolbox of fast biomolecular NMR spectroscopy. **Prog. NMR spectrosc.** 55: 238-265 (2009).

19. Schanda, P., Huber, M., Verel, R., Ernst, M., Meier, B.H.
Direct detection of $^{3h}J_{NC'}$ hydrogen bond scalar couplings in proteins by solid-state NMR spectroscopy. **Angew. Chem. Int. Ed. Engl.**, 49, 9322-9325 (2009).
This is the first-ever experimental demonstration of the measurement of hydrogen-bond-mediated scalar couplings by solid-state NMR. I produced protein samples, developed the methodology, recorded the data and did the full data analysis.

2010

20. Brutscher, B., Schanda, P.
Rapid Multidimensional NMR: Fast-Pulsing Techniques and their Applications to Proteins. **Encyclopedia of Magnetic Resonance.** 43: 1-10 (2009). Book chapter.

21. Corazza, A., Rennella, E., Schanda, P., Mimmi, M.C., et al.
Native-unlike long-lived intermediates along the folding pathway of the amyloidogenic β_2-microglobulin revealed by real-time 2D NMR. **J. Biol. Chem.**, 285, 5827-35 (2010).
I initiated this collaboration, collected the NMR data and contributed to data analysis and writing of the publication.

22. Schanda, P., Meier, B.H., Ernst, M.
Quantitative analysis of protein backbone dynamics in microcrystalline ubiquitin by solid-state NMR spectroscopy. **J. Am. Chem. Soc.**, 132, 15957-67 (2010).
Based on new methodology, I provided a comprehensive analysis of the dynamics in a model protein.

2011

23. Van Melckebeke, H., Schanda, P., Gath, J., Wasmer, C., Verel, R., Lange, A., Meier, BH., Böckmann, A.
Probing water accessibility in HET-s(218-289) amyloid fibrils by solid-state NMR. **J. Mol. Biol.**, 405, 765-72 (2011)

24. Huber, M., Hiller, S., Schanda, P., Ernst, M., Böckmann, A., Verel, R., Meier, BH.
A proton-detected 4D solid-state NMR experiment for protein structure determination. **ChemPhysChem**, 12, 915-8 (2011)
I initiated this project and supervised the PhD student who finalized this work.

25. Schanda, P., Meier, BH., Ernst, M.
Accurate measurement of one-bone H-X heteronuclear dipolar couplings in MAS solid-state NMR. **J. Magn. Reson.** 210, 246-59 (2011).

26. Schanda, P., Huber, M., Boisbouvier, J., Meier, BH., Ernst, M.
Solid-state NMR measurements of asymmetric dipolar couplings provide insight into protein side-chain motion. **Angew. Chem. Int. Ed. Engl.** 50, 1105-9 (2011)

27. Lalli, D., Schanda, P., Chowdhury, A., Retel, J., Hiller, M., Higman, VA., Agarwal, V., Reif, B., van Rossum, B., Akbey, U., Oschkinat, H.
Three-dimensional deuterium-carbon correlation experiments for high-resolution solid-state MAS NMR spectroscopy of large proteins. **J. Biomol. NMR,** 51, 477-85 (2011)

2012

28. Huber, M., With, O., Schanda, P., Verel, R., Ernst, M., Meier, B.
A supplementary coil for ^{2}H decoupling with commercial HCN MAS probes. **J. Magn. Reson.** 214, 76-80 (2012)

29. Rennella, E., Cutuil, T., Schanda, P., Ayala, I., Forge, V., Brutscher, B.
Real-Time NMR Characterization of Structure and Dynamics in a Transiently-Populated Protein Folding Intermediate. **J. Am. Chem. Soc.** 134: 8066-69 (2012)

30. Tollinger, M., Sivertsen, A. C., Meier, B. H., Ernst, M., Schanda, P.
Site-resolved measurement of microsecond to millisecond conformational-exchange processes in proteins by solid-state NMR spectroscopy. **J. Am. Chem. Soc.** 134: 14800-07 (2012)
In this publication, we demonstrate for the first time the detection of low-populated excited states in proteins.

31. Asami S, Szekely K, Schanda P, Meier BH, Reif B.
Optimal degree of protonation for H-1 detection of aliphatic sites in randomly deuterated proteins as a function of the MAS frequency. **J. Biomol. NMR** 54:155-68 (2012)

2013

32. Rennella, E., Cutuil, T., Schanda, P., Ayala, I., Gabel, F., Forge, V., Corazza, A., Esposito, E., Brutscher, B.
Oligomeric states along the folding pathways of b2-microglobulin: kinetics, thermodynamics, structure. **J. Mol. Biol** 425: 2722-36 (2013)

33. Haller, J. and Schanda, P. Amplitudes and time scales of picosecond-to-microsecond motion in proteins studied by solid-state NMR: a critical evaluation of experimental approaches and application to crystalline ubiquitin
J. Biomol. NMR (2013)

2014

34. Ma, P.; Haller, J. D.; Zajakala, J.; Macek, P.; Sivertsen, A. C.; Willbold, D.; Boisbouvier, J.; Schanda, P. Probing transient conformational states of proteins by solid-state R1ρ relaxation-dispersion NMR spectroscopy*Angewandte Chemie (International ed in English)* 2014, *53*, 4312.

35. Morin, S.; Linnet, T. E.; Lescanne, M.; Schanda, P.; Thompson, G. S.; Tollinger, M.;

Teilum, K.; Gagné, S.; Marion, D.; Griesinger, C.; Blackledge, M.; d'Auvergne, E. J. **relax: the analysis of biomolecular kinetics and thermodynamics using NMR relaxation dispersion data.** *Bioinformatics* **2014**, *30*, 2219.

Lectures:

Lectures at international conferences and workshops:

- Conference of the French NMR Association GERM, April 2005, Marseille (France)
- EUROMAR conference, July 2007, Tarragona (Spain)
- Intl. Workshop on High-Field Solid- and Solution-NMR, June 2009, Les Houches (France)
- Conference of the French Biophysical Society, Sept, 2010, La-Colle-sur-Loup (France)
- CCPNMR meeting, Oct. 2010, Hubertusstock/Berlin (Germany)
- 34th Annual Discussion Meeting DFG NMR, Sept 2012, Halle (Germany)
- Conference "Magnetic Moments in Central Europe", Feb 2013, Semmering (Austria)
- 8th Alpine Conference on solid-state NMR, Sept 2013, Chamonix (France)
- TSRC-LesHouches workshop on protein dynamics, may 2014, Les Houches (France)
- Carlsberg symposium on biomolecular NMR, May 2014, Copenhagen (Dk)
- EUROMAR conference, july 2014, Zurich (Switzerland)

Research seminars at universities:

- University of Vienna, Max F. Perutz Laboratories, Oct. 2007
- Computational Science group (Prof. Parrinello) at ETH, Lugano, Switzerland, Feb. 2010
- University of Strasbourg, Institute of Organic Chemistry, March 2011 (Job Interview for Professor position; I was offered the position but declined in favor of a position at IBS Grenoble.)

Teaching acitivities

Teaching is an integral part of research. Therefore, I was keen to teach throughout my career. I found teaching often very inspiring and several of my research ideas started out from a question that came up while teaching. Below is a list of the lectures and courses I have given in the last years, as well as a list of young scientists I supervised.

ETH Zürich

2008-2010 One lecture or course per semester on the following topics:

- Quantum mechanics
- Thermodynamics

I was giving one course per week with about 10-15 students (3rd and 4th semester), accompanying a plenary lecture. In these courses, example calculations were elaborated together to help understand the content of the lecture and prepare for the exams. I was responsible for designing exercises, performing them together with students, correcting them and preparing student for their exam.

- Introduction to NMR spectroscopy

I was responsible for organizing courses that accompanied a plenary lecture on NMR spectroscopy given by M. Ernst and B. Meier. Similar to the above case, these courses treated numerical and theoretical examples of NMR spectroscopy. I was responsible for designing exercises and managing the group of tutors, was well as holding the course with one of the groups of students.

- Advanced magnetic resonance (Relaxation theory in NMR)

I was assisting M. Ernst in setting up this 5-hour/week course on relaxation theory in NMR spectroscopy. Together with M. Ernst, we set up the content of the course, and wrote a manuscript, which we plan to publish as a book. In addition, I was assisting two students per week in preparing a talk on a selected topic in relaxation theory.

Université J. Fourier Grenoble

2011-2014	"NMR as a tool for structural biology", Master course, Université J. Fourier Grenoble. Co-lecturer together with 2 colleagues. Particular focus of my lectures: protein dynamics and protein folding.
2013	Basics of NMR spectroscopy: Course for PhD students in the European Network "IDPbyNMR".
2006	Thermodynamics for pharmaceutics students. I was responsible for guiding a group of students through example exercises (typically calculations) in thermodynamics, correcting and designing exercises.

Supervision of young researchers

04/2014-present	Supervision of post-doc Jia-Ying Guan
2013-present	Co-Supervision of PhD student Vilius Kurauskas
2013 (3 months)	Supervision of Master Student (J. Zajakala). 1 publication.
2012-2013 (10 months)	Supervision of Master Student (J. Haller). 2 publications + 1 in preparation.
2011- present	Supervision of two post-Doctoral fellows (A. C. Sivertsen, P. Ma) at the current host institute (IBS Grenoble). 2 publications.
2011	Supervision of two master students (M. Callon, R. Rapisarda) at IBS Grenoble.
2008-2010	Co-supervision of Ph. D. student (M. Huber) at ETH Zürich, resulting in 4 co-published papers (2x Angew. Chem., 1x ChemPhysChem, 1x J. Magn. Reson.), and one in preparation. I introduced Mr. Huber to proton-detected solid-state NMR experiments, a topic that I initiated in the group, and that turned into a major part of his Ph. D. work.
2009	Supervision of master student (K. Szekely) at ETH Zürich. Mrs. Szekely later joined the group as a Ph. D. student. 1 publication.
2009	Supervision of a Ph. D. student (J. Lopez, University of Madrid), who visited the group at ETH Zürich for 2 months during his Ph. D.
2006	Supervision of master student (M. Falge). Topic: Development of a sensitivity-optimized experiment for structural studies by NMR. 1 publication.